Assessment of Biomass Burning and Mineral Dust Impacts on Air Quality and Regional Climate

A Dissertation Presented for the
Doctor of Philosophy
Degree
The University of Tennessee, Knoxville

Xinyi Dong
December 2015

Copyright © 2015 by Xinyi Dong
All rights reserved.

DEDICATION

I dedicate this dissertation to my family for their endless love and support.

ACKNOWLEDGEMENTS

First of all, I would like to thank my committee members: Dr. Gregory Peterson, Dr. John Drake, Dr. Joshua Fu, and Dr. Wayne Davis. I am especially grateful to Dr. Fu for his help in my study since 2010. His outstanding teaching skills guided me to this interesting area and helped me develop the skill and ability to conduct scientific research with sufficient independence. While working with Dr. Fu, I also learned a lot from him on developing skills working with collaborators and funding agencies. I am grateful to Dr. Drake for this assistance and guidance in getting my research topic started from a solid base with an important yet applicable goal. I am also grateful to Dr. Davis for his support and encouragement. Dr. Davis has a very tight schedule as the Dean of the College of Engineering. Yet he spared time and provided me with many detailed comments and suggestions about my defense presentation and dissertation. Dr. Gregory Peterson's teaching helped me develop programming skills which are especially important for the intensive numerical modeling work in this study.

I wish to expend special thanks to all of the members of our research group for their friendship and great support. I would also like to thank the faculty and staff members in the Department of Civil and Environmental Engineering at The University of Tennessee, especially Dr. Chris Cox, Dr. Kan Huang, and Lisa Smith for their support and help during the past years.

Finally and most importantly, I would like to thank my wife and my parents, for their support, encouragement, quiet patience, and unwavering love.

ABSTRACT

East Asia is frequently influenced by dust storms and biomass burning. This study conducts a comprehensive investigation of its kind based on data analysis with surface measurements, satellite products, and model simulations. The objective of this study is to improve the understanding of the impacts of biomass burning and dust on air quality and regional climate. The study period covers March and April from 2006 to 2010. Biomass burning from Peninsular Southeast Asia (PSEA) has significant annual variations by up to 60% within the study period. The impact of biomass burning on air quality is mainly confined within the upper air due to the uplift motion driven by lee-side trough along eastern side of Tibet Plateau. The Weather Research and Forecasting and Community Multiscale Air Quality (WRF/CMAQ) system successfully reproduces the spatial distributions and temporal variations of air pollutants. Simulation bias falls in the range of 10%~50%, mainly due to the uncertainties within the emission inventory. This study reveals that the default WRF/CMAQ model has doubt counting of the soil moisture effect and subsequently underestimates dust emission by 55%. The microphysical parameterization and the speciation profile are revised to characterize the emission and mass contribution of dust better. Heterogeneous dust chemistry is also incorporated. These modifications substantially improve the model performance as indicated by the comparison between model simulations and observations. This study reveals that biomass burning has significant warming effect due to the presence of the underlying stratocumulus cloud. Biomass burning aerosol cools the near surface air by -0.2K, and significantly warms the upper air by up to +2K. Dust aerosol cools the near surface air by -0.9K and warms the upper air by +0.1K. This is the first investigation into the coexistence of biomass burning and dust over East Asia. This coexistence changes the aerosol direct radiative effect efficiencies of both biomass burning and dust by ±10%.

TABLE OF CONTENTS

1 DISSERTATION OVERVIEW 1

1.1 Introduction 1

1.2 Research goals 3

1.3 Applications of the study 3

2 METHODOLOGY 4

2.1 Overview of the methodology 4

2.2 Model description 4

2.3 Improvement of the wind-blown dust scheme 7

2.3.1 Improvement of CMAQ wind-blown dust emission scheme 9

2.3.2 Implementing source-dependent speciation profile 12

2.3.3 Implementing heterogeneous reactions 15

2.4 Emissions 16

2.5 Observations 19

2.5.1 Overview of the ground measurements and satellite products used in this study 19

2.5.2 AERONET 21

2.5.3 API 21

2.5.4 EANET 21

2.5.5 CERES products 26

2.5.6 Observations from Hong Kong and Taiwan 26

2.5.7 Observations from Thailand 27

2.5.8 MODIS products 27

2.5.9 OMI products 27

2.5.10 Surface observations from NCDC 28

2.5.11 TRMM and GPCP precipitation 28

2.6 Simulation design 28

3 BASELINE MODEL EVALUATION AND IMPACT ANALYSIS OF BIOMASS BURNING 30

3.1 Declaration 30

3.2 Abstract 30

3.3 Introduction 32

3.4 The WRF/CMAQ model evaluation 34

3.4.1 Evaluation of the offline WRF prediction 34

3.4.2 Evaluation of surface concentrations 34

3.4.3 Evaluation of column densities 53

3.5 Uplift motion and impact of biomass burning on air quality 68

3.5.1 Uplift motion and transport pathway of biomass burning 68

3.5.2 Annual variations of biomass burning 73

3.5.3 Impact of biomass burning on AOD 83

4 ASSESSMENT OF CMAQ MODEL PERFORMANCE AND INVESTIGATION OF DUST IMPACT ON AIR QUALITY 85

4.1 Declaration 85

4.2 Abstract *85*

4.3 Introduction *86*

4.4 Results and discussion *87*

4.4.1 Impact of applying revised friction velocity threshold 87

4.4.2 Impact of applying source-dependent speciation profile 89

4.4.3 Impact of heterogeneous chemistry 93

4.4.4 Case study of a severe dust storm 100

4.4.5 Remaining uncertainty within the modeling system 104

5 IMPACT OF BIOMASS BURNING AND DUST ON REGIONAL CLIMATE 112

5.1 Declaration *112*

5.2 Abstract *112*

5.3 Introduction *113*

5.4 Results and discussion *115*

5.4.1 Evaluation of the two-way mode WRF/CMAQ system 115

5.4.2 Impact of biomass burning aerosol on regional climate 131

5.4.3 Impact of dust on regional climate 140

5.4.4 Coexistence of biomass burning and dust 148

6 SUMMARY AND FUTURE STUDIES 157

6.1 Summary of the study *157*

6.2 Summary of Chapter 3 ..... *158*

6.3 Summary of Chapter 4 ..... *159*

6.4 Summary of Chapter 5 ..... *160*

6.5 Future studies *161*

REFERENCES 163

VITA 178

LIST OF TABLES

Table 2.1 Speciation profile of aerosol subspecies for the default CMAQ dust, Taklamakan (TK) dust, and Gobi dust 14
Table 2.2 Heterogeneous reactions and uptake coefficients 17
Table 2.3 Description of the observational dataset used in this study 24
Table 2.4 Simulation design and impact assessment method 29
Table 3.1 Evaluation Statistics for WRF simulation 38
Table 3.2 Evaluation statistics for surface concentrations of O_3, NO_2, SO_2, CO, PM_{10}, and $PM_{2.5}$ 43
Table 3.3 Evaluation statistics for VCD NO_2 58
Table 3.4 Evaluation statistics for AOD 67
Table 4.1 Evaluation statistics for tracer metals and $PM_{2.5}$ 92
Table 4.2 Evaluation statistics for the Dust_Profile, Dust_Chem, and Dust_ChemHigh simulation scenarios 101
Table 5.1 Evaluation Statistics for SWR flux 118
Table 5.2 Evaluation Statistics for T and RH 125
Table 5.3 Evaluation statistics for precipitation from the WRF (Offline) and WRF/CMAQ (Inline) simulations 129
Table 5.4 Dust aerosol impact on SW flux at TOA and SFC under clear sky condition 143

LIST OF FIGURES

Figure 2.1 Methodology flowchart 5
Figure 2.2 The WRF/CMAQ modeling system, and two-way communication diagram. Communicate diagram is modified based on Wong et al. [2012]..... 8
Figure 2.3 (a) Land cover categories; (b) Soil types; and (c) Comparison of initial friction velocity threshold constants in default and revised dust schemes 13
Figure 2.4 Comparison of five-year average biomass burning and anthropogenic CO emissions..... 22
Figure 2.5 Research domain and observation networks, different networks are represented by different markers: red cycles represent to API;, navy blue triangles represent PCD; green diamonds represent EANET; dark blue rectangles represent TAQMN; yellow rectangle represent HKEPD; and purple triangles represent AERONET..... 23
Surface measurements from different observational networks used in this study enable the evaluation of model performance at different sub-regions within the modeling Figure 3.1 Monthly average surface air temperature from NCDC observation (markers) and WRF simulation (color contours)..... 34
Figure 3.2 Overlay of simulated and observed surface concentrations of O_3 (1st column), NO_2 (2nd column), SO_2 (3rd column), CO (4th column), and PM_{10} (5th column) at surface level. Markers represent observations from different networks: cycles represent measurements from API, diamonds represent EANET, rectangular boxes represent TAQMN and HKEPD, and triangles represent PCD 40
Figure 3.3 Annual anthropogenic CO_2 emission for East Asia (EA) and PSEA..... 46
Figure 3.4 Daily variation of CO at (a) Lampang, (b) Ahuthaya, (c) Samut Sakorn, and (d) Chacherngsao. Green markers represent observations and solid black lines represent CMAQ simulations 49
Figure 3.5 (a) Spatial distribution of anthropogenic SO_2 emission from power plant sector, the locations of EANET and PCD observational station (triangles), and the locations of large power plants (cycles); (b) Population density over the Gulf of Thailand. .. 50
Figure 3.6 Daily variations of SO_2, NO_2, O_3, and PM_{10} at Samut Prakan and Bangkok. Markers represent observations and solid black lines represent CMAQ simulations 52
Figure 3.7 Daily variations of PM_{10}, SO_2, and NO_2 at Beijing, Guangzhou, and Banyu. Markers represent observations, solid black lines represent CMAQ simulations 54
Figure 3.8 Spatial distributions of VCD NO_2 from the OMI product and CMAQ simulation at 2:00 PM BT..... 55
Figure 3.9 Comparison of AOD from the MODIS product and CMAQ simulation at 11:00AM BT..... 60
Figure 3.10 Comparison of AOD between the AERONT observations and CMAQ simulations..... 63
Figure 3.11 Comparison of daily variations of AOD, AAOD, and SSA between CMAQ simulations and the AERONET observations..... 66
Figure 3.12 Biomass burning impact on O_3 at (a) 0~1km and (b) 1~3km height; Biomass burning O_3 flux at (c) 0~1km and (d) 1~3km height; (e) Topography in simulation

domain; (f) Cross sectional distributions of biomass burning impact on O_3; Geopotential height at (g) 850hPa and (h) 700hPa; (i) The LIST/OTD lightning product; and (j) The FLAMBE carbon emission 70
Figure 3.13 Biomass burning impact at near surface layer (0~1km) for O_3, $PM_{2.5}$, and CO for five-year average (1st column), 2008 (middle column), and 2010 (right column). Concentrations are plotted with filled color contours and percentage contributions are denoted by white dash lines with red labels..... 74
Figure 3.14 Comparison of daily variations of CO, O_3, and $PM_{2.5}$ between observation and the CMAQ simulation at Hong Kong and Taiwan-Sinjhuang. Observations are represented by markers. Black lines represent the Off_Base scenario simulation, and blue lines represent the Dust_Off scenario simulation 76
Figure 3.15 Biomass burning impact at upper air (1km~3km) for O_3, $PM_{2.5}$, and CO for five-year average (1st column), 2008 (middle column), and 2010 (right column). Concentrations are plotted with filled color contours and percentage contributions are denoted by white dash lines with red labels..... 78
Figure 3.16 Cross sectional distribution of biomass burning O_3 and wind fields on (a) Mar.7th, 2007; and (b)Mar.12th, 2008; O_3 vertical profiles from CWB sounding data and CMAQ simulations with and without biomass burning emission on (c) Mar.7th, 2007; and (d) Mar.12th, 2008 81
Figure 3.17 Biomass burning contribution to AOD for (a) five-year average; (b) 2008; and (c) 2010. 82
Figure 3.18 Comparison of daily average AOD between CMAQ simulations and the AERONET observations. Black lines represent the Dust_Off scenario, blue lines represent the Off_Base scenario, and red markers represent the AERONET observations 84
Figure 4.1 Dust concentration simulated under (a) Dust_Default scenario; and (b) Dust_Revised scenario; Simulation bias at the API observational stations for (c) Dust_Default; and (d) Dust_Revised scenario..... 88
Figure 4.2 CMAQ evaluation against PM_{10} observation from API and AOD observation from AERONET for Dust_Off, Dust_Default, and Dust_Revised scenarios..... 90
Figure 4.3 CMAQ evaluation for trace metals at Duolun and Yulin for (a) Dust_Revised, and (b) Dust_Profile scenario; and (c) Evaluation of CMAQ simulated (c) $PM_{2.5}$ at Duolun and Yulin..... 91
Figure 4.4 Impact of dust heterogeneous chemistry with lower (left panel) and upper (right panel) bound of uptake coefficient for surface concentration of O_3, SO_2, SO_4^{2-}, HNO_3, NO_x, and NO_3^-. Color contours represent the absolution concentrations change, and dash contour lines with numbers represent the percentages change..... 96
Figure 4.5 Spatial distribution of AOD from the MODIS product and the CMAQ simulation..... 102
Figure 4.6 Forward trajectories from (f) HYSPLIT; Comparison of daily average PM_{10} between observation and CMAQ simulations at (a) Beijing; (b) Lanzhou; (c) Nanjing; (d) Xiamen; (e) Lianyungang; (k) Shanghai; (g) Xinzhuang; (h) Oki; (i) Ogasawa; and (j) Hedo; Comparison of daily average AOD between simulations and the AERONET observations at (l) Beijing; (m) SACOL; (n) Osaka; and (o) NCU105

Figure 4.7 Temporal changes of the dust emission rate (solid orange rectangles), and the simulation bias of PM_{10} against observations from API (red cycles) and EANET (green diamonds). Dash lines represent the trends of the variables. 107
Figure 4.8 Spatial distribution of soil moisture fraction in the top 10cm soil depth from (a) FNL; and (b) GLDAS 111
Figure 5.1 Comparison of SWR between the CERES product (left panel) and the WRF/CMAQ simulation (right panel) for upwelling flux at TOA and downward flux at SFC 117
Figure 5.2 Comparision of air temperature at 1,000hPa, 950hPa, 920hPa, 850hPa, 780hPa, 700hPa, 620hPa, and 500hPa between the MODIS product (left panel) and the WRF/CMAQ simulation (right panel) 119
Figure 5.3 Comparision of relative humidity at 1,000hPa, 950hPa, 920hPa, 850hPa, 780hPa, 700hPa, 620hPa, and 500hPa between the MODIS product (left panel) and the WRF/CMAQ simulation (right panel) 122
Figure 5.4 Spatial distributions of precipitation from the TRMM product, the GPCP product, the offline mode WRF simulation, and the two-way mode WRF/CMAQ simulation. 127
Figure 5.5 Mass contributions of aerosol subspecies to biomass burning emission, data is derived from emission factors described in Akagi et al. [2011] 130
Figure 5.6 Impact of biomass burning aerosol on SWR flux at TOA and SFC under clear and all sky conditions. Color contours represent the absolute changes of SWR flux, and the white dash lines with red markers represent the percentage contribution.. 132
Figure 5.7 (a) Cloud fraction from WRF/CMAQ simulation; (b) Vertical profiles of cloud fraction from WRF/CMAQ simulation and the AIRS product at the selected grid (red rectangles in Figure 5.7(a)); (c) Cross Sectional distributions of cloud fraction (color contour), and biomass burning BC concentration (white dash lines with red markers with unit of $\mu g/m^3$). 134
Figure 5.8 Biomass burning aerosol induced temperature changes at (a) 20m; (b) 320m; (c) 530m; (d) 800m; (e) 1100m; and (f) 2500m above the surface ground. Upward triangles in (f) represent the locations of ground-based stations with sounding data. 136
Figure 5.9 (a) Comparison of air temperature profiles between the WRF/CMAQ simulations and sounding observations; (b) Biomass burning aerosol induced temperature change 137
Figure 5.10 Spatial distribution of biomass burning aerosol induced precipitation change 138
Figure 5.11 Impact of dust aerosoll on SWR flux at TOA and SFC under clear and all sky conditions. Color contours represent the absolute changes of SWR flux, and the white dash lines with red markers represent the percentage contribution 141
Figure 5.12 Snow cover from the NHSNOWM product. Green curve represents the location of Hengduan Mountains 142
Figure 5.13 Dust induced temperature changes at (a) 50m, (b) 250m, (c) 610m, (d) 5,500m, (e) 6,500m, and (f) 7,000m above the surface ground. Upward triangles in (f) represent the locations of ground-based stations with sounding data 144

Figure 5.14 (a) Comparison of temperature profiles between the WRF/CMAQ simulation and sounding observations; (b) Dust induced temperature change 146
Figure 5.15 CALIPSO aerosol subtype product on Mar.16th 2010 147
Figure 5.16 Coexistence of biomass burning and dust aerosol at the MPL EPA-NCU site in Taiwan on Mar.29th 2006. (a) MPL normalized back scatter observation; (b) HYSPLIT back trajectories from Mar.26th to Mar.29th; (c) Spatial (upper panel) and cross sectional (lower panel) distributions of biomass burning BC; (d) Spatial (upper panel) and cross section distributions of dust ASOIL; (e) MODIS AOD; (f) Vertical profiles of aerosol concentrations and temperature change 150
Figure 5.17 Same as Figure 5.16 but for the coexistence case on Mar.11th 2010 152
Figure 5.18 CALIPSO aerosol subtype on Mar.11th 2010..... 153
Figure 5.19 Aerosol radiative effect efficiency of dust and biomass burning under “No mixing”, “Mixing”, and “Overlay” conditions. 156

1 DISSERTATION OVERVIEW

1.1 Introduction

Wind-blown dust emitted from desert has important impacts on atmospheric environment. Dust reduces the atmospheric visibility and increases concentrations of suspended particles. It also alters climate forcing by absorbing and scattering solar radiation. Mineral dust has important far-reaching influence on the global biogeochemical cycle [*Zhuang et al.*, 1992]. The acidified dust particles may mobilize the dissolution ratio of iron and subsequently affect the rate of carbon fixation in high-nutrient and low-chlorophyll regions of the Pacific Ocean [*Meskhidze et al.*, 2003]. Northwest part of China and Mongolia are the main terrestrial sources of airborne dust over East Asia. Dust aerosol emitted from the Taklamakan and Gobi Desert can even travel across the Pacific Ocean toward United States. The East Asian dust storm has been well documented by previous studies with modeling and measuring methods. These published studies mainly focused on the transport pathway of dust storms, the chemical and physical characteristics of dust particles, and the impact of dust on air quality. However, the microphysical scheme of wind-blown dust emission and dust heterogeneous chemistry is not well understood. Many uncertainties still remain in our knowledge about natural wind-blown dust. For example, the dust heterogeneous chemistry involves natural dust particles and anthropogenic emission of sulfur dioxide (SO_2), nitrogen oxides (NOx), and volatile organic compound (VOC), but the reaction rate of the chemical process is not well quantified. In addition, the dust heterogeneous chemistry may produce secondary inorganic aerosol, and also change the radiative forcing budget. Recently, a few pilot studies have investigated the impact of mineral dust on air quality by using ground measurements. Huang et al. [2010] reported observed enhancement of sulfate (SO_4^{2-}) and reductions of nitrate (NO_3^-) and ammonium (NH_4^+) within the polluted dust samples over north China due to heterogeneous reactions between alkaline dust and anthropogenic SO_2; Wang et al. [2007b] found increased acidity of dust particles due to reaction with anthropogenic pollutants based on observation data from five nearby desert sites; Wang et al. [2013] reported observed

enhancement of organic carbon (OC) in urban Xi'an due to reaction between gaseous organics and dust. However, very limited modeling studies have been conducted to simulate the atmospheric chemistry process involving mineral dust and the subsequent impact on regional climate.

Compared with mineral dust, biomass burning aerosol has smaller particle size. It has large mass contribution from organic aerosol and small contributions from inorganic aerosol and crustal species. The characteristics of biomass burning and its impacts on air quality have been well documented by some recent studies [*Chuang et al.*, 2013; *Fu et al.*, 2012b; *Huang et al.*, 2013; *Lin et al.*, 2014; *Tang et al.*, 2004]. But modeling methods employed by previous studies contain a lot of uncertainties. The major uncertainties include the difficulties of quantifying the physical and optical properties [*Myhre et al.*, 2005; *Myhre et al.*, 2013], the estimation of emission [*Ito and Penner*, 2005], plume rise [*Jian and Fu*, 2014], and the emission factors [*Wang et al.*, 2007a] of biomass burning. Understanding about the impact of biomass burning on climate is not well developed yet. Biomass burning may exert a slightly negative radiative forcing effect under clear sky condition, but significant positive radiative forcing effect above cloud [*Haywood et al.*, 2003; *Hsu et al.*, 2003]. Consequently, The Intergovernmental Panel on Climate Change (IPCC) suggests that the impact of biomass burning on climate forcing is an open-ended question [*IPCC*, 2007]. In addition, biomass burning aerosol may serve as cloud condensation nuclei (CCN) and intensify cloud activity. Some recent published studies suggested that organic carbon aerosol from biomass burning may be coated with hygroscopic aerosol such as SO_4^{2-} during the transport. And this coating process may suppress the rate of water uptake during cloud activation [*Chuang and Penner*, 1995; *Xiong et al.*, 1998]. In contrast, Mochida and Kawamura [2004] reported that biomass burning can significantly enhance the hygroscopic property of suspended aerosol. Aging and coating processes of biomass burning are poorly represented by chemical transport models. The interactions between biomass burning and regional climate necessitate the research effort to address these uncertainties in the modeling system and improve our understanding in this area.

East Asia is encountering critical air pollution issues and extreme weather events caused by climate change [*Piao et al.,* 2010; *Sun et al.*, 2014]. Investigation into biomass burning and dust is helpful to estimate their impacts on air quality and regional climate. The findings from this study will help to address the uncertainties and questions mentioned above.

1.2 Research goals

Research goals of this study include: (1) evaluate the impact of biomass burning and wind-blown dust on air quality and regional climate of East China; and (2) enhance the capability of the Weather Research and Forecasting and Community Multiscale Air Quality (WRF/CMAQ) modeling system.

1.3 Applications of the study

1. The modified WRF/CMAQ modeling system can serve as a useful modeling tool to investigate the emission, transport, and atmospheric chemistry of mineral dust.

2. Investigation into biomass burning and dust will provide baseline estimation of their impacts on air quality and regional climate of East Asia. This estimation can also serve as a baseline to investigate the contribution from anthropogenic emission.

2 METHODOLOGY

2.1 Overview of the methodology

Figure 2.1 shows the flowchart of the methodology. This study requires model developments of wind-blown dust emission scheme and heterogeneous chemistry scheme within the WRF/CMAQ modeling system. Offline simulations are conducted to estimate the impacts of biomass burning and dust on air quality. And then the impacts of biomass burning and dust on regional climate are evaluated with the inline mode WRF/CMAQ modeling system. Observation from ground measurements and satellite products are also employed to help analyze the impacts. Studying period covers March and April from 2006 to 2010, to investigate the inter-annual variation of biomass burning and dust.

2.2 Model description

The WRF model version 3.4 [*Skamarock and Klemp,* 2008] is used in this study to provide the meteorology simulation. WRF is also used to quantify the direct radiative forcing effect of biomass burning and dust aerosol. WRF is a state-of-the-science mesoscale numerical weather prediction modeling system developed through a collaborative efforts principally include the National Center for Atmospheric Research (NCAR), the National Oceanic and Atmospheric Administration (represented by the National Centers for Environmental Prediction (NCEP) and the (then) Forecast Systems Laboratory (FSL)), the Air Force Weather Agency (AFWA), the Naval Research Laboratory, the University of Oklahoma, and the Federal Aviation Administration (FAA). Key modules within the WRF system include: microphysics, cumulus cloud and shallow convection, planetary boundary layer (PBL), surface layer, land-surface, longwave radiation, shortwave radiation (SWR), and ocean physics. WRF has been applied in many modeling studies for both research and operational forecasting needs. In this study, the model is configured with 34 vertical layers, ranging from the surface to 50mb with finer resolution in the free troposphere. The horizontal grid resolution of WRF is 36 km in this study.

CMAQ is developed by the United States Environmental Protection Agency

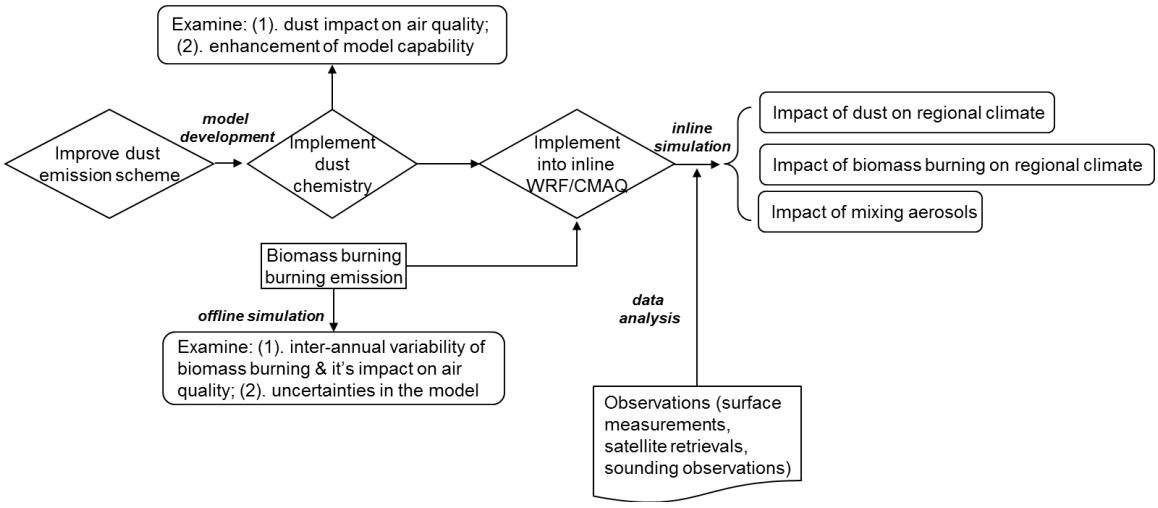

Figure 2.1 Methodology flowchart

(U.S. EPA) [*Byun and Ching*, 1999; *Byun and Schere*, 2006] as an air quality model for regulation purposes. CMAQ is a state-of-science model and has been applied world-wide for both research and regulation purposes. In this study, the latest version CMAQv5.0.1 is employed as the modeling platform to conduct simulations and implement model developments. Key physical and chemical modules within the CMAQ system include: subgrid turbulent vertical transport, horizontal advection and diffusion, vertical convection, aqueous chemistry, thermodynamic equilibrium between gas and aerosol, dry and wet depositions and gas-phase chemistry. The pre-processors that prepare inputs for the CMAQ system include: the emission processor SMOKE, the boundary condition processor BCON, initial condition processor ICON, and the photolysis reaction rate processor JPROC.

The offline mode CMAQ system takes inputs from meteorology models such as WRF and The PSU/NCAR mesoscale (MM5) model though the pre-processing program Meteorology-Chemistry Interface Processor (MCIP, [*Otte and Pleim,* 2010]). The offline mode simulation has been widely used by research community and even for the National Air Quality Forecasting purpose [*Otte et al.,* 2005]. However, as meteorology models and chemical transport models are developed independently, the offline mode simulation neglects the scientific inconsistency between the models. One of the most important uncertainties within the offline mode simulation is the omitting of aerosol feedback on radiation flux. CMAQ can simulate the new particles generation process, but it is unable to update the radiative forcing changes induced by new particles in meteorology model under offline mode simulation. Thus the impacts of aerosol on climate forcing can only be evaluated by radiative forcing models with prescribed aerosol inputs. The uncertainties within offline mode simulation drive the community to devote efforts for developing a two-way mode modeling system, which can enable the instantaneous communication between the chemical and meteorological simulations. The coupled WRF/CMAQ is the latest modeling system developed by U.S. EPA. It combines the meteorological and chemical models into one single executable file and bridges the communications between WRF and CMAQ. Figure 2.2 summarizes the key components within the modeling system. The communication diagram in two-way mode of WRF/CMAQ is also shown.

In the two-way mode of WRF/CMAQ system, a coupler is developed to facilitate the communication between WRF and CMAQ. The coupler includes a meteorology processor AQPREP and an aerosol feedback preprocessor Feedback. The AQPREP processor translates meteorological variables (e.g. pressure, temperature, wind, relative humidity) from WRF and prepares them compatible for CMAQ. And the Feedback processor translates aerosol concentration from CMAQ and prepares it for use in WRF. Figure 2.2 shows the calling frequency within the two-way mode WRF/CMAQ modeling system. The calling frequency ratio between WRF and CMAQ is setup as 4:1, and shortwave radiative forcing is updated every 6 time steps. The calling sequence within one full loop is described as below: WRF simulation is conducted for one time step (W_0), followed by the shortwave radiation (R_1) and AQPREP processor (A_0). After that, the WRF system continues to run for four time steps (W_1, W_2, W_3, and W_4), followed by the second calling of AQPREP processor (A_1). Then the CMAQ system is called for the first time (C_0-C_1), followed by the first calling of Feedback processor (F_1). The shortwave radiative forcing is called for the second time (R_2) after the 6th calling of WRF (W_6), and then the first loop ends. An important advantage of this two-way coupled system is that, it enables the investigation of the aerosol impact on meteorology field, and thus allows the evaluation of interactions between air quality and climate. It is important to notice that currently the coupler only considers direct radiative forcing effect of aerosol on shortwaver radiation. The impacts of aerosol on long waver radiation flux and the indirect effects of aerosol are not included in the WRF/CMAQ system yet.

2.3 Improvement of the wind-blown dust scheme

The wind-blown dust emission scheme is incorporated into CMAQ by U.S. EPA [*Appel et al.*, 2013]. Dust is usually treated as a unique aerosol species by other atmospheric models. But CMAQ divides dust emission into 19 aerosol subspecies, such as inorganic aerosol, organic aerosol, and trace metals. This method follows the original design of CMAQ as an air quality model, yet it also provides a potential modeling tool to identify the diversities of chemical and physical properties of dust particles. Dividing

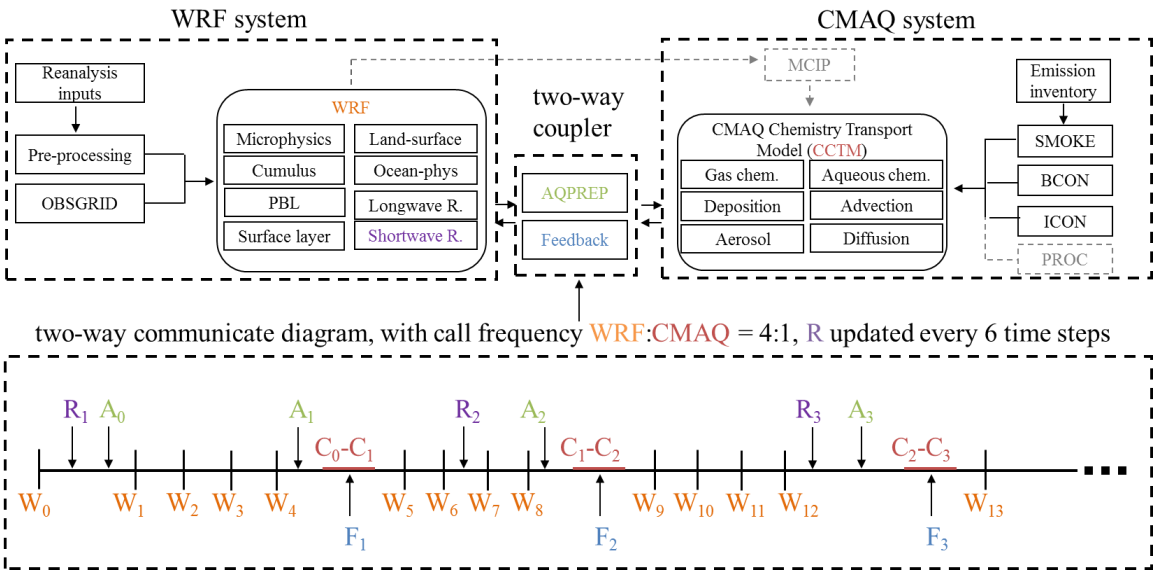

Figure 2.2 The WRF/CMAQ modeling system, and two-way communication diagram. Communicate diagram is modified based on Wong et al. [2012]

dust emission into subspecies also enables the model to investigate the mixing status between natural dust and other sources of aerosol, such as biomass burning and anthropogenic aerosol. The validation of CMAQ with wind-blown dust scheme is not well documented due to limited research efforts. Appel et al., [2013] conducted a full year simulation with CMAQ wind-blown dust over continental U.S. for 2006, and reported good agreement between simulation and observations. The mean bias was around ±0.5μg/m^3 and 0.5~1.5μg/m^3 (±30%) for soil concentrations over western and eastern U.S. respectively. However, CMAQ wind-blown dust significantly underestimates dust emissions over other regions. Fu et al. [2014] reported that the default dust scheme in CMAQ underestimated dust emission by 98% during a short dust storm episode in 2011. With modeling domain covering the entire Northern Hemisphere, Xing et al. [2015] also suggested that CMAQ underestimated AOD by 30%~60% in areas where mineral dust aerosol is dominant, while the bias was less than ±15% elsewhere. These studies suggested substantial uncertainty exist in the current CMAQ wind-blown dust scheme. So this study modifies the microphysical parameterization of CMAQ wind-blown dust scheme based on reanalysis of the field campaign data from Gillette et al. [1980]. This study also incorporates the dust heterogeneous chemistry into CMAQ, to estimate the impacts of dust on atmospheric chemistry. These modifications are also incorporated into the two-way mode WRF/CMAQ modeling system, to investigate the impact of dust on regional climate. The following sub-sections describe these modifications with more details.

2.3.1 **Improvement of CMAQ wind-blown dust emission scheme**

Wind-blown dust emission is determined by a number of environmental variables, including wind speed, soil texture, land use type, land cover, and soil moisture. The dust emission scheme employed in CMAQ was developed by Tong et al. [2015]. Dust emission (vertical flux) F (g/m^2s) is estimated based on the modified Owen's equation [*Owen et al.*, 1964; *Tong et al.*, 2015]:

$$F = \sum_{i=1}^{M}\sum_{j=1}^{N} K \times A \times \frac{\rho}{g} \times S_i \times SEP \times u_* \times (u_*^{\,2} - u_{*ti,j}^{\,2}) \qquad \text{for } u_* > u_{*ti,j} \quad \text{Equation 2.1}$$

where M is the erodible land use type, N is the soil texture type, K is the ratio of vertical to horizontal flux calculated based on the clay content (*clay%*) within the soil:

$$K = \begin{cases} 10^{[0.134\times(clay\%)]-6}, when: clay\% < 20\% \\ 0.0002, when: clay\% \geq 20\% \end{cases} \quad \text{Equation 2.2}$$

A is a scaling factor, ρ is air density, g is gravitational acceleration (9.8 m/s^2), and S_i is dust source area for land type i. *SEP* is the soil erodibility factor, which is calculated based on the amount of clay, silt, and sand of the soil as:

$$SEP = 0.08\times clay\% + 1.0\times silt\% + 0.12\times sand\% \quad \text{Equation 2.3}$$

And u_* is the friction velocity, $u_{*ti,j}$ is the threshold friction velocity for soil type j and land use type i. More details of the dust emission algorithm are summarized elsewhere [*Tong et al.*, 2015]. Equation 2.1 is applied only when model calculated friction velocity exceeds the designated threshold value. Therefore, the value of threshold friction velocity $u_{*ti,j}$ is critical to determine the onset and magnitude of dust emission in the CMAQ model.

In the CMAQ wind-blown dust scheme, the threshold friction velocity is dynamically calculated based on the presence of non-erodible elements and the change of soil moisture [*Tong et al.*, 2015]. The effect of non-erodible elements is represented by wind energy partitioning following Marticorna et al. [1997]. The effect of soil moisture is implemented following a two-step approach proposed by Fecan et al. [1999]. First, the maximum water holding capacity W_{max} (dimensionless) for each soil type is determined based on the clay content (*clay%*) of the soil:

$$W_{max} = (0.0014\times clay\% + 0.17)\times clay\% \quad \text{Equation 2.4}$$

In case that soil moisture exceeds W_{max}, the threshold friction velocity is then adjusted using a revised Fecan formulation [*Fecan et al.*, 1999]:

$$u_{*ti,j} = u_{*ci,j}\times Z_{i,j}\times f_{soilm\ i,j} \quad \text{Equation 2.5}$$

where $u_{*ci,j}$ is the initial threshold friction velocity constant, $Z_{i,j}$ is the surface roughness adjusting factor calculated with surface roughness length from meteorology field, and $f_{soilm\ i,j}$ is the moisture adjustment factor calculated as:

$$f_{soilm\ i,j} = \begin{cases} 999.9,\ for\ S_{oilm} > W_{max} \\ 1.0,\ for\ S_{oilm} \le W_{max} \\ \left(1.0 + 1.21 \times (S_{oilm} - W_{max})^{0.68}\right)^{0.5},\ for\ S_{oilm} \le S_{oill} \end{cases} \quad \text{Equation 2.6}$$

where S_{oilm} is soil moisture, and S_{oill} is the saturation soil moisture limit determined by soil textures.

In default CMAQ, the values of initial friction velocity constant are taken from observed data from wind tunnel experiments conducted by Gillette and co-workers [*Gillette et al.,* 1980, 1982]. Fu et al. [2014] found that the initial threshold friction velocity constant $u_{*ci,j}$ used in CMAQ has an average value of 0.7m/s among all soil types, which is too high to generate enough dust particles over East Asia. They used a fixed value for $u_{*ci,j}$ as 0.3m/s based on study of local measurements at northern desert in China [*Li et al.,* 2007]. This smaller threshold helped generate more dust emission during the simulation episode from May 1st to May 6th 2011 in their simulation. But Fu et al. [2014] arbitrarily assigned the thresholds for all land covers and soil categories, thus they prevented the model from reproducing spatial and temporal variations of dust emission under different weather and surface conditions. Recent reanalysis of the Gillette field data revealed that while some of these experiments were performed under rather dry conditions, for most samples the soil moisture effect is non-negligible. Therefore, these values reported from field experiments are not always suitable to be used directly as the initial threshold friction velocity constant, which is assumed to represent extremely dry condition. Meanwhile, in the CMAQ dust module, dynamic soil moisture data are used to adjust threshold friction velocity, thus applying the default values by Gillette would double count the impact of soil moistures under some conditions. In this study, the revised values of $u_{*ci,j}$ are developed based on the reanalysis of the Gillette field data. Land cover and soil types within the study domain are shown in Figure 2.3(a) and (b) respectively. Comparison of the default and revised friction velocity threshold constants are summarized in Figure 2.3(c). The revised friction velocity threshold constants are lower than the default ones, indicating that the revised wind-blown dust scheme is expected to produce more dust emission.

2.3.2 **Implementing source-dependent speciation profile**

The emission of natural wind-blown dust is distributed to 19 aerosol species in the CMAQ system following the speciation profile developed based on the EPA's SPECIATE database [*Simon et al.,* 2010]. This approach provides a more detailed description of the chemical characteristics of dust particles. However, mass contributions of different chemical components may differ significantly for dust emission from different deserts. So using a fixed profile for all the dust emission may introduce uncertainty and lose the capacity of modeling the varieties of dust particles. Mass contribution of Aluminum (Al) is around 6% to 8% for pure minerals. The ratios between other trace metals and Al could vary substantially for different dust particles. The elemental mass ratio between Calcium and Aluminum (Ca/Al) is usually used to identify the source region of sampled dust particles [*Huang et al.*, 2010; *Sun et al.*, 2005]. For example, the Ca/Al ratio is 0.9~2.0 for the Saharan dust [*Blanco et al.*, 2003; *Formenti et al.*, 2003; *Kandler et al.*, 2007; *Reid et al.*, 2003], 0.13~0.15 for the Arabian dust [*Krueger et al.*, 2004], 1.5~1.9 for the Taklamakan dust [*Huang et al.*, 2010], and 0.4~1.1 for the Gobi dust [*Arimoto et al.*, 2006; *Zhang et al.*, 2003]. To characterize the dust emission better, speciation profiles are developed in this study for the Gobi and Taklamakan deserts based on local measurement data collected by Huang et al. [2010]. These two profiles are compared with the default one used in the CMAQ as shown in Table 2.1. Some of the aerosol species were not measured by Huang et al. [2010], such as the primary organic carbons (APOC), non-carbon aerosol (APNCOM), elementary carbon (EC), silicon (ASI), and water (AH2O). The mass contributions of these species for the Taklamakan and Gobi deserts are kept the same as in the default profile. For unspeciated (AOTHR) and non-anion dust (ASOIL), their values in the two new profiles are calculated based on the contributions of all other species, to keep the total mass conservative. It is important to notice that the modeled species represent the anion or cation phase for sulfate (SO_4^{2-}), nitrate (NO_3^-), chloride (Cl^-), ammonium (NH_4^+), sodium (Na^+), Ca_2^+, magnesium (Mg_2^+), and potassium (K^+). The model species represent the element phase for iron (Fe), Al, silicon (Si), titanium (Ti), and manganese

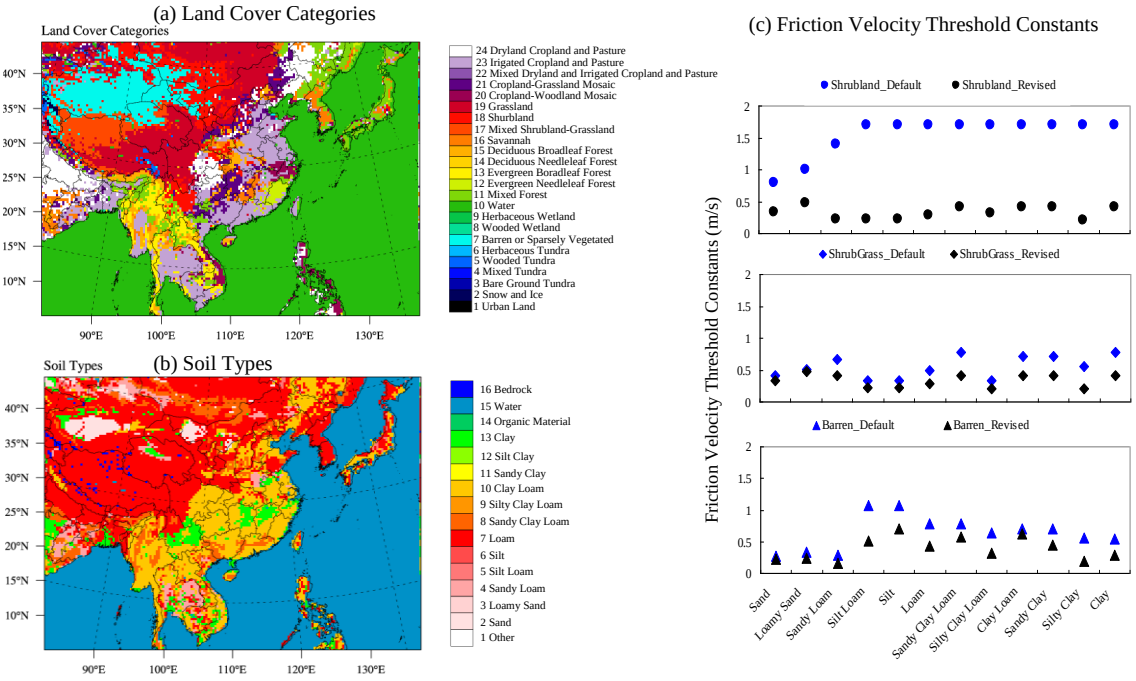

Figure 2.3 (a) Land cover categories; (b) Soil types; and (c) Comparison of initial friction velocity threshold constants in default and revised dust schemes

Table 2.1 Speciation profile of aerosol subspecies for the default CMAQ dust, Taklamakan (TK) dust, and Gobi dust

Model Variable	Description	Mass Conributions (%)					
		Fine Mode (I,J mode in CMAQ ≤2.5μm)			Coarse Mode (K mode in CMAQ ≤10 μm)		
		Default	TK	Gobi	Default	TK	Gobi
ASO4	Sulfate (SO_4^{2-})	2.5	3.554	0.953	2.655	2.825	0.471
ANO3	Nitrate (NO_3^-)	0.02	0.181	0.204	0.16	0.125	0.084
ACL	Chloride (Cl^-)	0.945	2.419	0.544	1.19	2.357	0.094
ANH4	Ammonium (NH_4^+)	0.005	0.098	0.346	0	0.066	0.185
ANA	Sodium (Na^+)	3.935	2.234	1.016	0	2.056	0.301
ACA	Calcium (Ca_2^+)	7.94	2.063	1.788	0	1.423	1.082
AMG	Magnesium (Mg_2^+)	0	0.165	0.799	0	0.121	0.819
AK	Potassium (K^+)	3.77	0.153	0.282	0	0.108	0.121
APOC	Primary Organic Carbon	1.075	1.075	1.075	0	0	0
APNCOM	Non-carbon organic matter	0.43	0.43	0.43	0	0	0
AEC	Elementary carbon	0	0	0	0	0	0
AFE	Iron (Fe)	3.355	4.689	2.425	0	3.75	3.055
AAL	Aluminum (Al)	5.695	5.926	4.265	0	4.987	4.641
ASI	Silicon (Si)	19.425	20.739	14.929	0	17.454	16.245
ATI	Titanium (Ti)	0.28	0.312	0.337	0	0.285	0.365
AMN	Manganese (Mn)	0.115	0.0758	0.063	0	0.062	0.072
AH2O	Water (H_2O)	0.541	0.541	0.541	0	0	0
AOTHR	Unspeciated	50.219	55.345	70.002	0	0	0
ASOIL	Non-anion dust	0	0	0	95.995	64.382	72.464

(Mn). Mass contributions of different species differ significantly among the default, Taklamakan, and Gobi profiles as shown in Table 2.1. For example, Ca_2^+ accounts for 7.94% of the total fine particle mass in the default profile. But it only accounts for 2.06% in the Taklamakan dust and 1.79% in the Gobi dust., The default profile assumes a zero percentage of mass contribution for Mg_2^+, yet the contribution in the Taklamakan and Gobi dust is 0.17% and 0.79% respectively. Contribution of K^+ in the default profile is 3.77%, while in the Taklamakan dust is 0.153%, and in the Gobi dust is 0.28%. Si is one of the most abundant metals in the Earth's crust, yet the default speciation profile had an inappropriate assumption for Si as zero in coarse mode dust particles. No measurements were found for Si over the Taklamakan or Gobi deserts. So this study uses the element ratio of Al/Si as 8%/28% to derive the mass contribution of Si in the coarse model dust particles, which is a conventional approach for trace metal analysis [*Huang et al.,* 2010]. Speciation profile has a dominant impact on the model simulated concentrations of aerosol species, which will be discussed with more details in Chapter 4.

2.3.3 **Implementing heterogeneous reactions**

Default heterogeneous chemistry scheme within CMAQ considers the conversions of N2O5 to HNO3, and NO2 to HONO and HNO3. These conversions play important role for nighttime production of nitrate [Dong et al., 2014; Pathak et al., 2011; Pun and Seigneur, 2001]. Heterogeneous reactions are treated as irreversible in the model [Davis et al., 2008; Sarwar et al., 2008; Vogel et al., 2003]. Dust aerosol is involved the reactions to deplete gas-phase species and produce secondary inorganic aerosol. The uptake of gases onto the surface of dust particle is defined by a pseudo-first-order reaction rate K [Dentener et al., 1996; Heikes and Thompson, 1983], which is calculated as:

$$K = \left(\frac{r_p}{D_g} + \frac{4}{v_g \gamma_g} \right)^{-1} A_p \qquad \text{Equation 2.7}$$

where r_p is the radius of the particle, D_p is the diffusion coefficient of gas molecules, v_p is the mean molecular velocity of gas, A_p is the surface area of particle, and γ_g is the uptake coefficient for the gas. Many research efforts have been devoted to quantify

the uptake coefficients of different gases on dust particle. The reported values of uptake coefficient may differ even more than 2 to 3 orders of magnitude, depending on the source of the dust samples and analytical methods [*Cwiertny et al.*, 2008; *Usher et al.*, 2003]. Modeling domain in this study is over East Asia, so the uptake coefficients used here are mainly collected from Zhu et al. [2010] which summarized the estimations with dust samples from deserts in China. The "best guess" of uptake coefficients were suggested by Zhu et al. [2010] based on analysis of different measurement studies. But in this study, the lower and upper limits of uptake coefficients are incorporated into the modeling system to evaluate the variations of heterogeneous chemistry. Table 2.2 shows the 13 dust heterogeneous reactions implemented into CMAQ in this study with the lower and upper boundaries of uptake coefficients.

2.4 Emissions

Due to the absence of official emission inventory of Asian countries, regional modeling studies usually have to rely on the inventories developed for research purpose. Transport Experiment-Phase B (INTEX-B) emission inventory which was also developed by NASA [*Zhang et al.*, 2009]; Ohara et al. [2007] also developed an emission inventory from fuel combustion and industrial sources for Asia for the period from 1980 to 2003. It is important to notice that these inventories are developed on an annual scale with coarse grid resolution and limited number of species. But regional modeling usually requires fine resolution for both temporal and spatial allocation and chemical speciation. Since Asian countries have experienced rapid economic changes during the past decade, their anthropogenic emissions are also expected to change accordingly. But the research efforts for updating Asian emission are limited and lag behind. The inventories mentioned above provide important basis for understanding the anthropogenic emissions over East Asia. But uncertainties within these inventories may introduce significant discrepancies for model simulations. This study uses the emission inventory from Zhao et al. [2013] over China because it is promptly updated and has been applied in some recent modeling studies [*Wang et al.*, 2011; *Zhao et al.*, 2013]. The INTEX-B inventory is used for other countries in the modeling domain.

Table 2.2 Heterogeneous reactions and uptake coefficients

No.	Reaction	Uptake coefficient (Reference)
Default heterogeneous reactions in CMAQv5.0.1		
C1	$N_2O_5 + H_2O \longrightarrow 2HNO_3$	$\gamma = \begin{cases} (x_1 + x_2) \times \gamma_d^* + x_3 \times \min(\gamma_d^*, \gamma_3), RH < CRH \\ \sum_{i=1}^{3} x_i \times \gamma_i^*, RH > IRH \\ 0.02, otherwise \end{cases}$ where x_1, x_2, x_3 and $\gamma_1, \gamma_2, \gamma_3$ are the normalized molar concentrations and N_2O_5 uptake coefficients on NH_4HSO_4, $(NH_4)_2SO_4$, and NH_4NO_3 respectively, $\gamma_d^* = \min(\gamma_d, 0.0124)$ where γ_d is the uptake coefficient on dry particles determined by relative humidity and temperature, RH is relative humidity, CRH is crystallization relative humidity, IRH is ice formation relative humidity determined by temperature [*Davis et al.*, 2008]
C2	$2NO_2 + H_2O \longrightarrow HONO + HNO_3$	$K = 5.0 \times 10^{-6} \times A_p$ [*Vogel et al.*, 2003]
Implemented dust heterogeneous reactions in this work		
R1	$O_3 + dust \longrightarrow products$	$5.0 \times 10^{-5} \sim 1.0 \times 10^{-4}$ [*Zhu et al.*, 2010]
R2	$OH + dust \longrightarrow products$	$0.1 \sim 1.0$ [*Zhu et al.*, 2010]
R3	$H_2O_2 + dust \longrightarrow products$	$1.0 \times 10^{-4} \sim 2.0 \times 10^{-3}$ [*Zhu et al.*, 2010]
R4	$CH_3COOH + dust \longrightarrow products$	1.0×10^{-3} [*Zhu et al.*, 2010]
R5	$CH_3OH + dust \longrightarrow products$	1.0×10^{-5} [*Zhu et al.*, 2010]
R6	$CH_2O + dust \longrightarrow products$	1.0×10^{-5} [*Zhu et al.*, 2010]
R7	$HNO_3 + dust \longrightarrow 0.5NO_3^- + 0.5NO_x$	$1.1 \times 10^{-3} \sim 0.2$ [*Dentener et al.*, 1996]
R8	$N_2O_5 + dust \longrightarrow 2NO_3^-$	$1 \times 10^{-3} \sim 0.1$ [*Zhu et al.*, 2010]
R9	$NO_2 + dust \longrightarrow NO_3^-$	$4.4 \times 10^{-5} \sim 2.0 \times 10^{-4}$ [*Underwood et al.*, 2001]
R10	$NO_3 + dust \longrightarrow NO_3^-$	$0.1 \sim 0.23$ [*Underwood et al.*, 2001]

Table 2.2 Continued

No.	Reaction	Uptake coefficient (Reference)
R11	$NO_3 + dust \longrightarrow HNO_3$	1.0×10^{-3} [*Martin et al.,* 2003]
R12	$HO_2 + dust \longrightarrow 0.5H_2O_2$	0.2 [*Underwood et al.,* 2001]
R13	$SO_2 + dust \longrightarrow SO_4^{2-}$	$1.0\times10^{-4} \sim 2.6\times10^{-4}$ [*Pandis and Carmichel,* 2000]

Biogenic emission is generated by the Model of Emissions of Gases and Aerosol from Nature (MEGANv2.10) (http://bai.acd.ucar.edu/Megan/index.shtml). MEGAN has been applied in many global and regional modeling studies. Biogenic emission from MEGAN is demonstrated to have good estimation of natural emission [*Guenther et al.*, 2006; *Muller et al.*, 2008].

This study uses the biomass burning emission developed from the Fire Locating and Modeling of Burning Emissions (FLAMBE) project [*Reid et al.*, 2009]. Fu et al. [2012b] compared the FLAMBE inventory and the Global Fire Emissions Database (GFED) inventory [*van der Werf et al.,* 2008, 2010]. It was reported that the GFED inventory underestimated emission over PSEA, and the FLAMBE inventory has better agreement with surface observations. The finding is also consistent with the conclusion from Nam et al. [2010], which reported that biomass burning emission is substantially underestimated due to lack of agricultural fires based on a global simulation with GFED. Time step of the FLAMBE inventory also fits better with the WRF/CMAQ system as compared with the GFED inventory.

To briefly introduce the intensities and distributions of emission inventories used in this study, Figure 2.4 shows the CO emission from biomass burning and anthropogenic inventories. CO emission is averaged for March and April respectively from 2006 to 2010. As shown in the figure, biomass burning emission is mainly distributed over Myanmar, north part of Laos, and northwest part of Thailand. Anthropogenic emission is much less intensive over PSEA, while China is the main contributor within the study domain.

2.5 Observations

2.5.1 Overview of the ground measurements and satellite products used in this study

Model evaluation is necessary to reveal the stability and sensitivity of model performance under different meteorological and emission conditions. So observations from both ground surface measurements and satellite products are used in this study to evaluate the performance of the WRF/CMAQ modeling system. Observations are also

used to facilitate the assessment of impact of biomass burning and dust. Public accessible surface measurements in Asian countries are limited in terms of both spatial coverage and monitored variables. This study collects observations from multiple networks, in order to cover most of the countries within the simulation domain. Figure 2.5 shows the locations of ground surface observational stations from some of the networks employed in this study. These databases include: the AErosol RObotic NETwork (AERONET; [*Holben et al.*, 2001]) operated by NASA; the Air Pollution Index (API; http://datacenter.mep.gov.cn) operated by the Chinese Ministry of Environmental Protection (MEP); the Acid Deposition Monitoring Network in East Asia [*EANET*, 2007]; the U.S. COOP network observations operated by National Climatic Data Center (NCDC); the Pollution Control Department of Ministry Natural Resources and Environment of Thailand (PCD; http://www.pcd.go.th/indexEng.cfm); the Hong Kong Environmental Protection Department (HKEPD, [*Kwok et al.*, 2010]); the Taiwan Air Quality Monitoring Network (TAQMN; http://taqm.epa.gov.tw/taqm/en/default.aspx) organized by Taiwan EPA. Local dust sampling data is also collected through personal contact with Dr. Guoshun Zhuang from Fudan University in China. Satellite products used in this study include: cloud fraction from the Atmospheric Infrared Sounder (AIRS); shortwave radiation flux from the NASA's Cloud and the Earth's Radiant Energy System (CERES); precipitation from the Global Precipitation Climatology Project (GPCP) and the Tropical Rainfall Measuring Mission (TRMM); aerosol optical depth and vertical distributions of temperature and relative humidity from the Moderate Resolution Imaging Spectroradiometer (MODIS); and column density of NO_2 from the Ozone Monitoring Instrument (OMI). The ground-based Micro-Pulse Lidar (MPL) observations and remote sensing product of The Cloud-Aerosol Lidar and Infrared Pathfinder Satellite (CALIPSO) operated by NASA, and air temperature sounding profiles collected by University of Wyoming are also employed to examine the characteristics of aerosol vertical distribution. Table 2.3 summarizes the data utilized in this study, with more details described in the following sub-sections.

2.5.2 **AERONET**

AERONET provides globally measured observations of spectral aerosol optical depth by using the ground-based Sun Photometer [*Holben et al.*, 1998]. Optical properties of aerosol such as refractive index and single scattering are also retrieved with the sky radiance almucantar and direct sun measurements. AERONET provides daily observations of these optical properties at multiple spectral wavelengths. In this study the measurements at 550nm wavelength is used to compare with model simulations. The accuracy of level 2.0 AERONET product is of the order of ±0.03. There are 70 AERONET sites within the modeling domain of this study, and data from these sites is collected for the simulation period.

2.5.3 **API**

API is collected by local agencies at 86 of the major cities in China and managed by the federal government. For most of the cities, daily observations of multiple air pollutants are collected to calculate one API value for one city each. Empirical functions have been developed to convert API back into PM_{10} concentrations. There are six cities including Beijing, Guangzhou, Guiyang, Shanghai, Wuhan, and Xi'an that also report daily API values for SO_2 and NO_2. API has been used for investigating air pollution and evaluating model performance in several studies despite some uncertainties [*Dong et al.*, 2014; *Zhao et al.*, 2013].

2.5.4 **EANET**

EANET is a regional cooperative program based on ground surface measurements operated by collaborations from national agencies, institutes, universities, and partners at multiple East Asia and Southeast Asia countries. Observations from EANET include wet and dry depositions, inland aquatic environment, soil acidity and vegetation, and also ambient concentrations of air pollutants. The monitoring period, frequency, and variables monitored differ greatly among different stations. In this study, observations of PM_{10}, SO_2, NO_2, O_3, HNO_3, SO_4^{2-}, and NO_3^- are collected at 23 sites within the modeling domain.

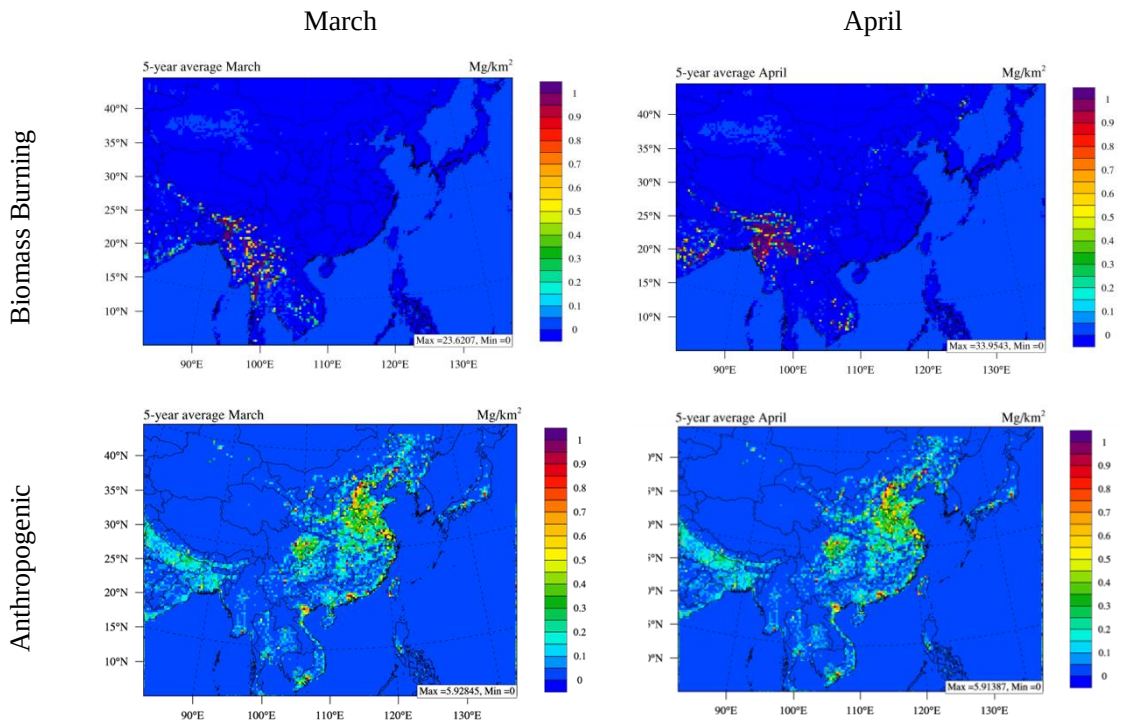

Figure 2.4 Comparison of five-year average biomass burning and anthropogenic CO emissions

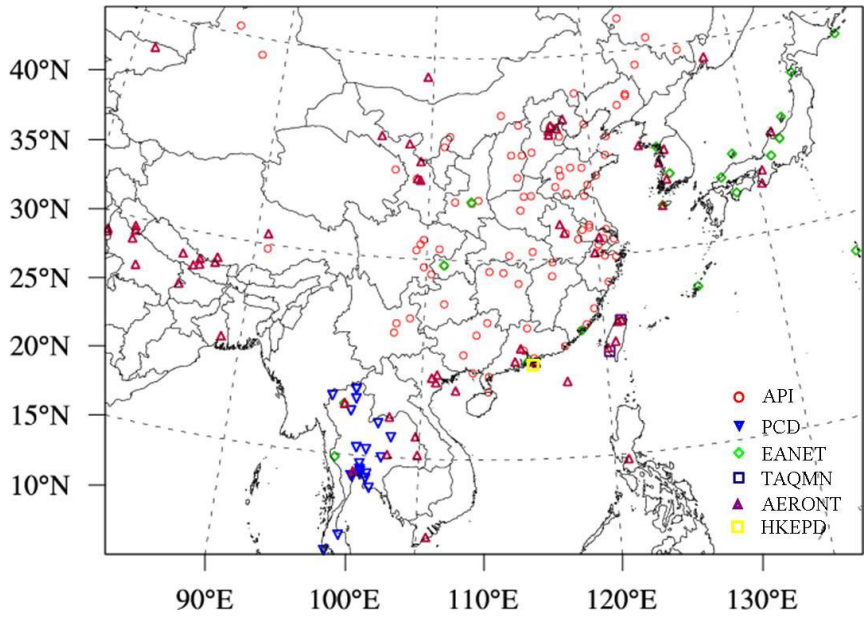

Figure 2.5 Research domain and observation networks, different networks are represented by different markers: red cycles represent to API;, navy blue triangles represent PCD; green diamonds represent EANET; dark blue rectangles represent TAQMN; yellow rectangle represent HKEPD; and purple triangles represent AERONET

Table 2.3 Description of the observational dataset used in this study

Ground-based measurements				
Dataset	Species measured	Observational frequency	Number of sites	Data source
AERONET	AOD	Daily	70 sites within our simulation domain	http://aeronet.gsfc.nasa.gov/cgi-bin/combined_data_access_new
API	PM_{10}, SO_2, NO_2	Daily	PM_{10}: 86 cities SO_2, NO_2: 6 cities	http://datacenter.mep.gov.cn
EANET	PM_{10}, SO_2, NO_2, O_3	Hourly/Daily/ Monthly	Hourly: 11 sites in Japan Daily: 4 sites in China, 4 sites in Thailand, 1 site in Russia Monthly: 3 sites in South Korea	http://www.eanet.asia/
Fudan Obs.	K^+, Ca^{2+}, Mg^{2+}, $PM^{2.5}$	Daily	3 sites (Duolun, Yunlin, Tazhong)	Personal contact with Dr. Guoshun Zhuang
HKEPD	SO_2, CO, O_3, $PM_{2.5}$	Daily	4 sites (Tap Mun, Yuen Long, Tung Chung, Tsuen Wan)	http://epic.epd.gov.hk/EPICDI/air/station/?lang=en
TAQMN	PM_{10}, SO_2, NO_2, CO, O_3, $PM_{2.5}$	Hourly	2 sites (Sinjhuang and Ciaotou)	http://taqm.epa.gov.tw/taqm/en/default.aspx
MPL	Back scattering coefficient	Hourly	1 site (Taiwan Central University)	http://mplnet.gsfc.nasa.gov/data.html
NCDC	Temperature, wind speed, wind direction, humidity	Daily	878 sites	http://rda.ucar.edu/
PCD	PM_{10}, SO_2, NO_2, CO, O_3	Daily	25 sites	http://www.pcd.go.th/indexEng.cfm

Table 2.3 Continued

Dataset	Species measured	Observational frequency	Number of sites	Data source
Wyoming Sounding	Air temperature vertical profile	Daily	10 sites	http://weather.uwyo.edu/upperair/sounding.html

Satellite retrievals

Dataset	Species measured	Observational frequency	Data source
AIRS	Cloud fraction	Daily	http://airs.jpl.nasa.gov/data/get_data
CALIPSO	Attenuated backscatter	Daily	http://www-calipso.larc.nasa.gov/tools/data_avail/
CERES	Shortwave radiation flux	Daily	https://eosweb.larc.nasa.gov/project/ceres/ceres_table
GPCP	Precipitation	Monthly	ftp://precip.gsfc.nasa.gov/pub/gpcp-v2.2/psg
MODIS	AOD	Daily	http://ladsweb.nascom.nasa.gov/data/search.html
OMI	Column NO_2	Daily	http://disc.sci.gsfc.nasa.gov/Aura/data-holdings/OMI/omno2_v003.shtml
TRMM	Precipitation	Monthly	http://mirador.gsfc.nasa.gov/cgi-bin/mirador/presentNavigation.pl?project=TRMM&tree=project

2.5.5 **CERES products**

CERES refers to a series of instruments developed for NASA's EOS experiment on board of the TRMM, Aqua, Terra, and Suomi National Polar-orbiting Partnership (S-NPP) satellites. Each of the instrument measures filtered radiances in three regions, including the shortwave (0.4~0.5 μm), total (0.3~200 μm), and window (8~12 μm) bands. CERES products include solar-reflected and Earth-emitted radiation from the top of the atmosphere (TOA) and the Earth's surface (SFC) [*Wielicki et al.,* 1998]. The CERES Energy Balanced Filled (EBAF) dataset provides monthly global retrievals of shortwave radiation flux at both TOA and at the ground surface [*Loeb et al.,* 2009, 2012], which has been employed in many studies [*Anantharaj et al.,* 2010; *Yu et al.,* 2006]. In this study, the CERES EBAF-TOA and EBAF-SFC products with 1 °×1 ° spatial resolution are used to compare with model simulations of shortwave radiation fluxes reaching the Earth and reflected back into the space.

2.5.6 **Observations from Hong Kong and Taiwan**

Observations from Hong Kong and Taiwan are frequently employed in regional studies to investigate the transported air pollutants from inland China and Southeast Asia [*Chuang et al.,* 2013; *Lin et al.,* 2009]. The HKEPD has established more than 10 ground surface observational sites for monitoring air pollutants and meteorological variables at Hong Kong. In this study, daily observations of O_3, SO_2, CO, and $PM_{2.5}$ from four representative HKEPD sites (Tap Mun, Yuen Long, Tung Chung, Tsuen Wan) are collected evaluate the model simulations. The Taiwan EPA has operated the local air quality monitoring network TAQMN at most of the counties in Taiwan. In this study, PM_{10} concentrations measured at two representative stations (Sinjhuang and Ciaotou) are collected to facilitate evaluating the model simulations at north and south part of Taiwan.

The ground-based MPL measurements of back scattering coefficient is initiated by NASA and operated through a collaborative program between NASA and the local Taiwan EPA and National Central University [*Wang et al.,* 2010]. In this study, the daily MPL level2 data is collected to investigate the vertical distributions of aerosol.

2.5.7 **Observations from Thailand**

The Thailand PCD has set up local air quality monitoring network with more than 20 sites across the country. In this study, the daily observations of CO, PM_{10}, SO_2, NO_2, and O_3 are collected to evaluate model simulations.

2.5.8 **MODIS products**

The standard MODIS products have been applied in tremendous studies in different research areas. The two MODIS sensors on board of Aqua and Terra satellites provide a wide spectral range (0.4μm~14μm) and high spatial resolution (0.25km~1km) measurements by following a sun-synchronous near-polar orbit with global coverage with one or two days. Standard MODIS products include various retrievals for atmosphere (e.g. aerosol, cloud, and air temperature), land (e.g. land cover, vegetation index, and wild fires), cryosphere (e.g. ice and snow cover), and ocean (ocean color and sea surface temperature) variables. In this study, the daily MOD08 product of AOD with $1°\times1°$ grid resolution and 5-minutes MAM07 product of air temperature and water vapor profile [*Borbas et al.,* 2011] are used to evaluate model simulations. The MAM07 product is integrated and averaged on daily scale at 8 pressure levels including 500hPa, 620hPa, 700hPa, 780hPa, 850hPa, 920hPa, 950hPa, and 1000hPa.

2.5.9 **OMI products**

The OMI sensor is on board of EOS-Aura satellite following a near-polar orbit with pixel size of 13×24km at nadir with daily global coverage. The OMI imaging spectrograph ranges from 270nm to 500nm with a spectral resolution about 0.5nm. The standard OMI products include column densities of O_3, NO_2, HCHO, BrO, cloud pressure and fraction, and also AOD. In this study, the daily OMNO2d product [*Boersma et al.*, 2007] of cloud-screened tropospheric column NO_2 with $0.25°\times0.25°$ grid resolution is collected to evaluate model simulations.

2.5.10 **Surface observations from NCDC**

In this study, the daily observations of surface air temperature, wind speed and wind direction, and humidity are collected at more than 800 sites from the NCDC dataset to evaluate the model simulations.

2.5.11 **TRMM and GPCP precipitation**

TRMM is a joint mission between NASA and Japan Aerospace Exploration Agency (JAXA) for rainfall observation [*Huffman et al.,* 2001, 2007]. GPCP is established by the World Climate Research Program (WCRP) with the objective to quantify the global distribution of precipitation [*Adler et al.,* 2003; *Huffman et al.*, 2009]. Both TRMM and GPCP have been applied in many research studies for model evaluation and analysis purposes. In this study, the monthly TRMM 3B-43 product with $0.25° \times 0.25°$ grid spatial resolution, and the monthly GPCPv2.2 product with $2.5° \times 2.5°$ grid spatial resolution are collected to facilitate the evaluation and analysis of the two-way mode WRF/CMAQ modeling system.

2.6 Simulation design

A total of 10 simulation scenarios are designed with different configurations to analyze the impacts from biomass burning and dust. The differences between simulations therefore represent the impacts induced by the difference within configurations. For example, the Off_Base scenario is offline WRF/CMAQ simulation with anthropogenic and biogenic emission only. The Dust_Off scenario is configured same as the Off_Base scenario, but it also includes biomass burning emission. Thus the difference between Off_BB and Dust_Off represents the impact of biomass burning on air quality. The Inline_Base and the Inline_DusOff scenarios are configured same as the Off_Base and the Dust_Off scenarios respectively, but these two scenarios are performed with the two-way mode WRF/CMAQ modeling system. Thus the difference between the Inline_DustOff scenario and the Inline_Base scenario represents the impact of biomass burning on regional climate. A full description of the simulation scenarios and their represented impacts are summarized in Table 2.4.

Table 2.4 Simulation design and impact assessment method

Simulation design	
Offline Mode Scenarios	Configuration of WRF/CMAQ
Off_Base	Baseline simulation with anthropogenic and biogenic emission only, without inline calculation of dust
Dust_Off	Same as Off_Base but add biomass burning emission over Southeast Asia
Dust_Default	Same as Dust_Off but with default dust plume rise scheme
Dust_Revised	Same as Dust_Off but with revised intial friction velocity threshold constant in dust plume rise scheme
Dust_Profile	Same as Dust_Revised but with implemented source dependent speciation profile
Dust_Chem	Same as Dust_Profile, but with implemented dust chemistry with lower limit of uptake coefficient
Dust_ChemHigh	Same as Dust_Chem, but with upper limit of uptake coefficients
Two-way Mode Scenarios	Configuration of two-way WRF/CMAQv5.0.1
Inline_Base	Same as Off_Base but performed with the two-way mode WRF/CMAQ system
Inline_DustOff	Same as Dust_Off but performed with the two-way mode WRF/CMAQ system
Inline_Profile	Same as Dust_Profile but performed with the two-way mode WRF/CMAQ system
Impact Assessment Method	
Scenarios Employed	Represented Impacts
Dust_Off – Off_Base	Impact of biomass burning on air quality (Chapter 3)
Dust_Default – Dust_Off	Impact of dust on air quality evaluated by default dust scheme in CMAQ (Chapter 4)
Dust_Revised – Dust_Off	Impact of dust on air quality evaluated by revised dust scheme with new parameterization of initial friction velocity threshold constant (Chapter 4)
Dust_Profile – Dust_Revised	Impact on aerosol prediction by applying source-dependent speciation profile (Chapter 4)
Dust_Chem – Dust_Profile	Impact of dust heterogeneous chemistry with lower limit of uptake coefficient (Chapter 4)
Dust_ChemHigh – Dust_Profile	Impact of dust heterogeneous chemistry with upper limit of uptake coefficient (Chapter 4)
Dust_ChemH – Dust_Profile	Impact of dust heterogeneous chemistry with lower limit of uptake coefficient (Chapter 4)
Inline_DustOff – Inline_Base	Impact of biomass burning aerosol on regional climate (Chapter 5)
Inline_Profile – Inline_DustOff	Impact of dust aerosol on regional climate (Chapter 5)
Inline_Profile – Inline_Base	Impact of mixed dust and biomass burning on regional climate (Chapter 5)

3 BASELINE MODEL EVALUATION AND IMPACT ANALYSIS OF BIOMASS BURNING

3.1 Declaration

This chapter summarizes the contents of the following two publications:

Dong, X., and J.S. Fu (2015a). Understanding the inter-annual variation of biomass burning from Peninsular Southeast Asia, part I: Model evaluation and analysis of systematic bias. *Atmospheric Environment*, 116, 293-307.

Dong, X., and J.S. Fu (2015b). Understanding the inter-annual variation of biomass burning from Peninsular Southeast Asia, part II: Variability and different impacts in lower and higher atmospheric layers. *Atmospheric Environment*, 115, 9-18.

3.2 Abstract

In this chapter the performance of the WRF/CMAQ modeling system is evaluated with the observation data described in Chapter 2. The impact of biomass burning on air quality is analyzed with model simulation and observation. The WRF/CMAQ modeling system is applied over Peninsular Southeast Asia (PSEA) and East Asia for five years from 2006 to 2010. As many of the published modeling studies over Asia were evaluated with limited regional measurements, this study uses ground surface measurements collected from multiple networks. These measurements provide a domain-wide coverage for model evaluation and impact analysis. Satellite products are also collected to comprehensively evaluate the performance of the WRF/CMAQ system. This study finds increasing simulation discrepancy for CO, NO_2, and SO_2 from 2006 to 2010 at south part of PSEA (≤17°N) due to outmoded anthropogenic emission. Local surface observation and CO_2 emission data reported by World Bank suggest substantial growth of anthropogenic emission over PSEA during the simulation period. The original spatial distribution of the INTEX-B anthropogenic emission is determined by population density. But this method results in overestimation at populated area and underestimation at industry area. Over north PSEA (>17 ℃N), the WRF/CMAQ model systematically overestimates CO, surface NO_2, and tropospheric column NO_2 by 6%~20%, 8~15%, and

40%~50% respectively. Analysis with the OMI satellite product suggests that the overestimated emission factor of deforestation fire should be responsible for the modeling bias. No distinct temporal trend of the modeling bias is found over East Asia, and the WRF/CMAQ modeling system overestimates AOD, NO_2, and SO_2 by 20%~50%. The model also underestimates PM_{10} at north and northeast East Asia by 50%~60% due to the impact of dust storm, because the default dust emission scheme within the model is unable to reproduce it. Evaluation result from this study suggests an urgent need to update the anthropogenic emission over PSEA. Findings from this study also suggest that the dust emission module within CMAQ system contains significant uncertainty and requires further development.

Data analysis is performed with simulation, surface observation, and satellite products to investigate the inter-annual variation of biomass burning in terms of its emission, transport and impact on air quality. Analysis of geopotential height indicates that PSEA biomass burning plume is frequently lifted by the lee side trough into free troposphere. The lightning observation data suggests that deep convection is weak over PSEA during the biomass burning season, thus it may only play a minor role for uplifting the fire plume. Biomass burning emission has large annual variation. For example, the emission in 2010 is 65% higher than that in 2008. But the impact of biomass burning on near surface air has less variability since most of the plume is lifted into free troposphere. At lower part of the free troposphere within 1km~3km height, impact of biomass burning has large variability. Sounding observation at Taiwan demonstrates that biomass burning has negligible impact on the near surface layer O_3. But it can contribute more than 30% of the total O_3 at free troposphere within 1~6km height during massive burning episode. Biomass burning also changes AOD over East Asia. The impact of biomass burning on AOD ranges from 0.1~0.3 (25%~45%) in 2008 to 0.2~0.6 (50%~70%) in 2010. This study suggests that PSEA biomass burning may introduce significant changes to atmospheric chemistry and radiative forcing budget within free troposphere over East Asia.

3.3 Introduction

Biomass burning over Southeast Asia (SEA) has important impact on atmospheric visibility, public health, aquatic system, and regional climate. Peninsular Southeast Asia (PSEA) includes Cambodia, Laos, Myanmar, Thailand, and Vietnam. The biomass burning at PSEA usually peaks in March and April with a sharp decrease in May due to the onset of summer monsoon. Biomass burning introduces about two-thirds of the total organic carbon and 50% of the element carbon over PSEA [*Gustafsson et al.*, 2009]. Biomass burning also leads to photochemical production of O_3 and formation of secondary inorganic aerosol, due to intensive emission of nitrogen oxides (NO_x) and SO_2. While many of the local countries are highly populated, biomass burning from PSEA also affects the downwind metropolitans, such as Hong Kong and Taiwan. PSEA biomass burning plume is brought into East Asia by subtropical the Westerlies and the Asian monsoon system. Some published studies have reported that it deteriorates the air quality in downwind areas [*Deng et al.*, 2008; *Fu et al.*, 2012b; *Huang et al.*, 2014; *Streets et al.*, 2003; *Wang et al.*, 2007a]. Evaluating the impact of biomass burning is helpful to better understand the changes of air quality and regional climate in sub-tropical areas.

In recent years, a few studies have been conducted with modeling or measuring methods to investigate the impact of biomass burning on air quality over PSEA and East Asia. These studies mainly focused on evaluating the contribution to air pollutants at local and downwind areas. Fu et al. [2012b] investigated the 2006 biomass burning with modeling method and reported that long-range transport introduced excessive $PM_{2.5}$ by 64μg/m^3 over eastern China; Huang et al. [2013] examined the same episode with models and ground measurements, and reported that the contribution from biomass burning to AOD was about 56% for local area, and 26%~62% for the downwind area; Tang et al., [2003] used the TRACE-P campaign measurements and regional model simulation to evaluate the 2001 biomass burning episode, and reported the averaged net influence in March was 50% for OH, 40% for HO_2, 60% for HCHO, and 10 ppbv for O_3; Hsu et al. [2003] used satellite products to evaluate the impact of biomass burning on radiative forcing in March 2000, and reported that the reflected solar radiation from cloud due to smoke aerosol can be reduced (enhanced) by up to 100 (20) W/m^2. Chuang et al. [2013]

analyzed the chemical characteristics of biomass burning aerosol, and reported that K^+ and water-soluble organic carbon from biomass burning were higher than previous estimations. During the past decade, some international collaborated field campaigns were conducted over PSEA to characterize the physical, chemical, and optical properties of biomass burning pollutants, such as the NASA TRACE-P [*Jacob et al.*, 2003], the UNEP ABC [*Nakajima et al.*, 2007], the NASA BASE-ASIA [*Tsai et al.*, 2013], and the 7-SEAS [*Lin et al.*, 2013; *Reid et al.*, 2013].

These research efforts have developed the fundamental knowledge of PSEA biomass burning in terms of the emission, transport pathway, and impacts on visibility and air quality. However, most of the published studies primarily focused on short episodes and very few of them have probed into the inter-annual variation of biomass burning. There remain two poorly understood issues: First, neither measuring nor modeling studies have described the annual changes or the upper and lower limits of PSEA biomass burning. It is essential to understand these upper and lower limits to estimate the overall impact of biomass burning for multiple years in order to assess its long term impacts on air quality and regional climate. Second, although we often rely on model simulation for impact analysis, the uncertainty within the modeling system and the stability of model predictions under different emission and meteorological conditions remain unknown. While the PSEA biomass burning has substantial annual changes [*Tsay et al.*, 2013], it is necessary to evaluate the inter-annual variation of the impacts. And it is also important to understand if the current modeling system can reproduce the variability. According to World Health Organization (WHO), many Asian countries are experiencing severe air pollution problems and rapid increases of anthropogenic emissions [*WHO*, 2011, 2014]. Understanding the inter-annual variation of PSEA biomass burning is also helpful to evaluate its relative importance and provide viable suggestions for mitigation and anthropogenic emission control.

In this study, the WRF/CMAQ modeling system [*Byun and Schere*, 2006] has been applied over PSEA and East Asia for five years from 2006 to 2010 in March and April. The WRF/CMAQ modeling system is thoroughly evaluated with observations from multiple networks over PSEA and East Asia for the first time in this study.

Evaluation of the modeling system is helpful to reveal the stability of model performance under different meteorology and emission conditions. And it is also helpful to identify the possible systematic errors and model sensitivities. This chapter summaries the analysis of model performance evaluation, and also discusses the impact of biomass burning on air quality.

3.4 The WRF/CMAQ model evaluation

3.4.1 Evaluation of the offline WRF prediction

WRF has been applied over Asia in many published studies, and has been demonstrated for its good agreement with observations [*Huang et al.*, 2013; *Zhao et al.*, 2013]. In this study, the offline WRF meteorology simulation is evaluated with observations from NCDC, which covers most of the countries within the research domain. The spatial distributions from WRF and NCDC are summarized in Figure 3.1. The evaluation statistics are summarized Table 3.1.

The meteorology field is reasonably well reproduced by the WRF model. Figure 3.1 shows the comparison between the observed and simulated surface air temperature from 2006 to 2010 in March and April. The WRF model successfully reproduces the spatial distributions of air temperature at 2m height as shown in Figure3.1. Some moderate discrepancies are identified for a few sites in Sichuan Basin area, southern China, and Tibet Plateau along Himalaya, which may be associated with the complex topography in these areas. Table 3.1 summarizes the statistics of the WRF model evaluation for key variables including air temperature, wind speed and relative humidity. The simulation bias for air temperature is about -0.5K. The WRF model systematically underestimates surface air temperature at 2m, owing to the excessive soil moisture of the National Centers for Environmental Prediction Final Analysis (NCEP FNL) data utilized in WRF simulation [Hu et al., 2010].

3.4.2 Evaluation of surface concentrations

Surface measurements from different observational networks used in this study enable the evaluation of model performance at different sub-regions within the modeling

Figure 3.1 Monthly average surface air temperature from NCDC observation (markers) and WRF simulation (color contours)

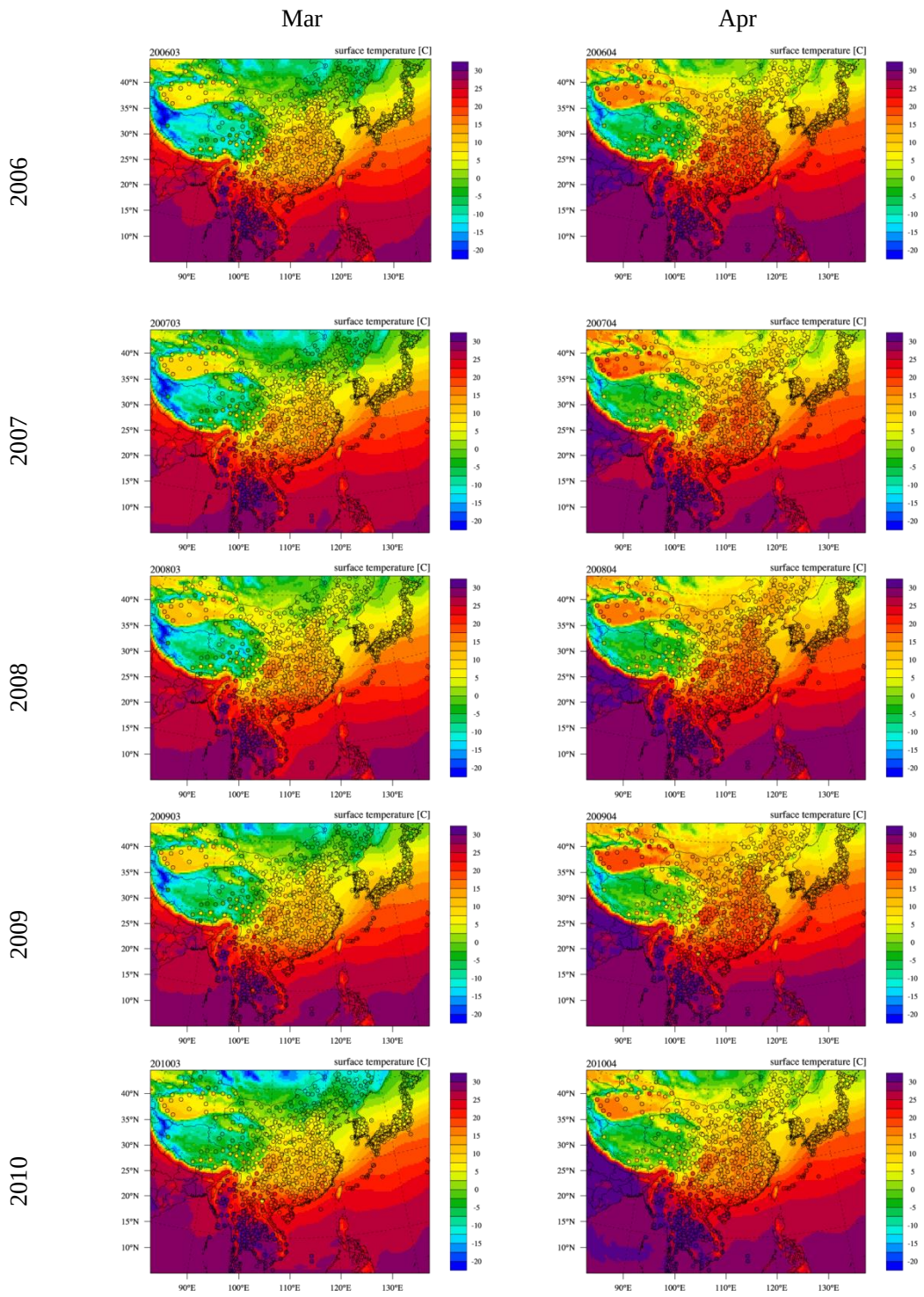

Figure 3.1 Continued

domain. Evaluation for all five years simulation helps to probe into the systematic errors and self-consistency of the modeling system. Comparisons between CMAQ simulations and observations are shown in Figure 3.2 for air pollutants including: O_3, NO_2, SO_2, CO, and PM_{10}. High concentrations of air pollutants are found over north part of PSEA and industrial areas over East Asia, indicating the dominant impacts from biomass burning and anthropogenic emission. Figure 3.2 also shows significant annual variations of air pollutants especially over PSEA and southwest China. As introduced in Chapter 2, biomass burning dominates the emission over north part of PSEA (>17 °N) and anthropogenic emission is dominant over south (≤17°N) part of PSEA. So evaluation statistics are calculated for north and south part of PSEA independently, to narrow down the uncertainties from biomass burning and anthropogenic emissions respectively, as summarized in Table 3.2.

Evaluation statistics summarized in Table 3.2 suggest that model performances at north and source part of PSEA are distinct from each other. Simulation bias has no significant changes for different years over north part of PSEA, but shows obvious annual trend over south part of PSEA. CO is overestimated by around 20% over north part of PEA from 2006 to 2010. Simulation bias over north part of PSEA for SO_2, NO_2, and O_3 is consistent with the overestimations of CO, and no significant temporal trend is found. Since biomass burning plays the dominant role at north part of PSEA, modeling discrepancy should be attributed to the systematic overestimation of biomass burning emission. Over south part of PSEA, simulation bias for CO ranges from 0.7% in 2006 to -19.3% in 2010. The gradually increased simulation bias suggests an increasing trend of model discrepancy 2006 to 2010. The simulation bias for other pollutants also shows similar trend as CO. SO_2 is slightly overestimated by 8% in 2006, but is significantly overestimated by 54.2% in 2010. NO_2 is slightly underestimated by -9.6% in 2006, but is significantly underestimated by -36.5% in 2010. Simulation bias for O_3 increases from 16.5% in 2006 to 39.9% in 2010. The ambient concentrations of CO, NO_2, and O_3 increase from 452.6ppbv, 11.5ppbv, and 26.1ppbv respectively in 2006 to 559.6ppbv, 13.4ppbv, and 32.7ppbv respectively in 2010. As the meteorology condition remains

Table 3.1 Evaluation Statistics for WRF simulation

		Temperature (K)						Wind Speed (m/s)						Humidity (g/kg)					
		Obs	Sim	MB[1]	GE[2]	RE[3]	R[4]	Obs	Sim	MB	GE	RE	R	Obs	Sim	MB	GE	RE	R
2006	Mar	285.67	284.90	-0.77	2.45	3.44	0.98	2.99	3.03	0.04	1.18	1.64	0.82	7.86	7.49	-0.37	1.19	1.80	0.98
	Apr	287.72	287.09	-0.63	2.19	3.08	0.97	3.51	3.66	0.15	1.40	1.89	0.82	7.89	8.06	0.17	1.08	1.53	0.98
2007	Mar	284.66	284.09	-0.57	2.21	3.10	0.98	3.45	3.66	0.21	1.37	1.84	0.81	6.50	6.64	0.14	1.07	1.61	0.97
	Apr	288.71	288.01	-0.71	2.16	2.96	0.97	3.22	3.20	-0.02	1.27	1.69	0.80	7.73	7.81	0.08	1.10	1.57	0.97
2008	Mar	285.63	285.17	-0.47	2.12	2.94	0.98	3.16	3.26	0.10	1.28	1.72	0.81	6.73	6.71	-0.02	1.16	1.78	0.96
	Apr	289.96	289.33	-0.63	2.12	2.90	0.97	3.21	3.28	0.07	1.29	1.75	0.80	8.66	8.68	0.02	1.21	1.77	0.97
2009	Mar	285.02	284.75	-0.27	2.15	2.99	0.98	3.40	3.65	0.25	1.38	1.86	0.82	6.72	6.84	0.12	1.14	1.71	0.97
	Apr	289.91	289.23	-0.68	2.10	2.89	0.97	3.23	3.27	0.03	1.30	1.73	0.81	8.35	8.49	0.14	1.21	1.71	0.97
2010	Mar	284.36	283.98	-0.38	2.08	2.88	0.98	3.49	3.92	0.42	1.48	1.96	0.81	6.97	6.93	-0.03	1.17	1.85	0.96
	Apr	288.18	287.65	-0.53	2.05	2.82	0.98	3.38	3.62	0.24	1.39	1.85	0.81	8.41	8.40	0.01	1.23	1.85	0.97

[1]MB $= \frac{1}{IJ}\sum_{j=1}^{J}\sum_{i=1}^{I}(Sim_j^i - Obs_j^i)$, Sim_j^i is the individual simulated value at site *j* and time *i*, and Obs_j^i is the individual observed value at site *j* and time *i*, and the summations are over all sites (*I*) and over time periods (*J*);

[2]GE $= \frac{1}{IJ}\sum_{j=1}^{J}\sum_{i=1}^{I}\left|Sim_j^i - Obs_j^i\right|$;

[3]RE $= \left[\frac{1}{IJ}\sum_{j=1}^{J}\sum_{i=1}^{I}(Sim_j^i - Obs_j^i)^2\right]^{1/2}$;

$^{4}\mathrm{R} = 1 - \left[\frac{IJ \cdot RMSE^{2}}{\sum_{j=1}^{J}\sum_{i=1}^{I}(\left|Sim_{j}^{i} - \overline{Obs}\right| + \left|Obs_{j}^{i} - \overline{Obs}\right|)} \right]$, where $\overline{Obs}$ is the average observed concentration and a value of 1 indicates perfect agreement between predicted and observed values.

Figure 3.2 Overlay of simulated and observed surface concentrations of O_3 (1st column), NO_2 (2nd column), SO_2 (3rd column), CO (4th column), and PM_{10} (5th column) at surface level. Markers represent observations from different networks: cycles represent measurements from API, diamonds represent EANET, rectangular boxes represent TAQMN and HKEPD, and triangles represent PCD

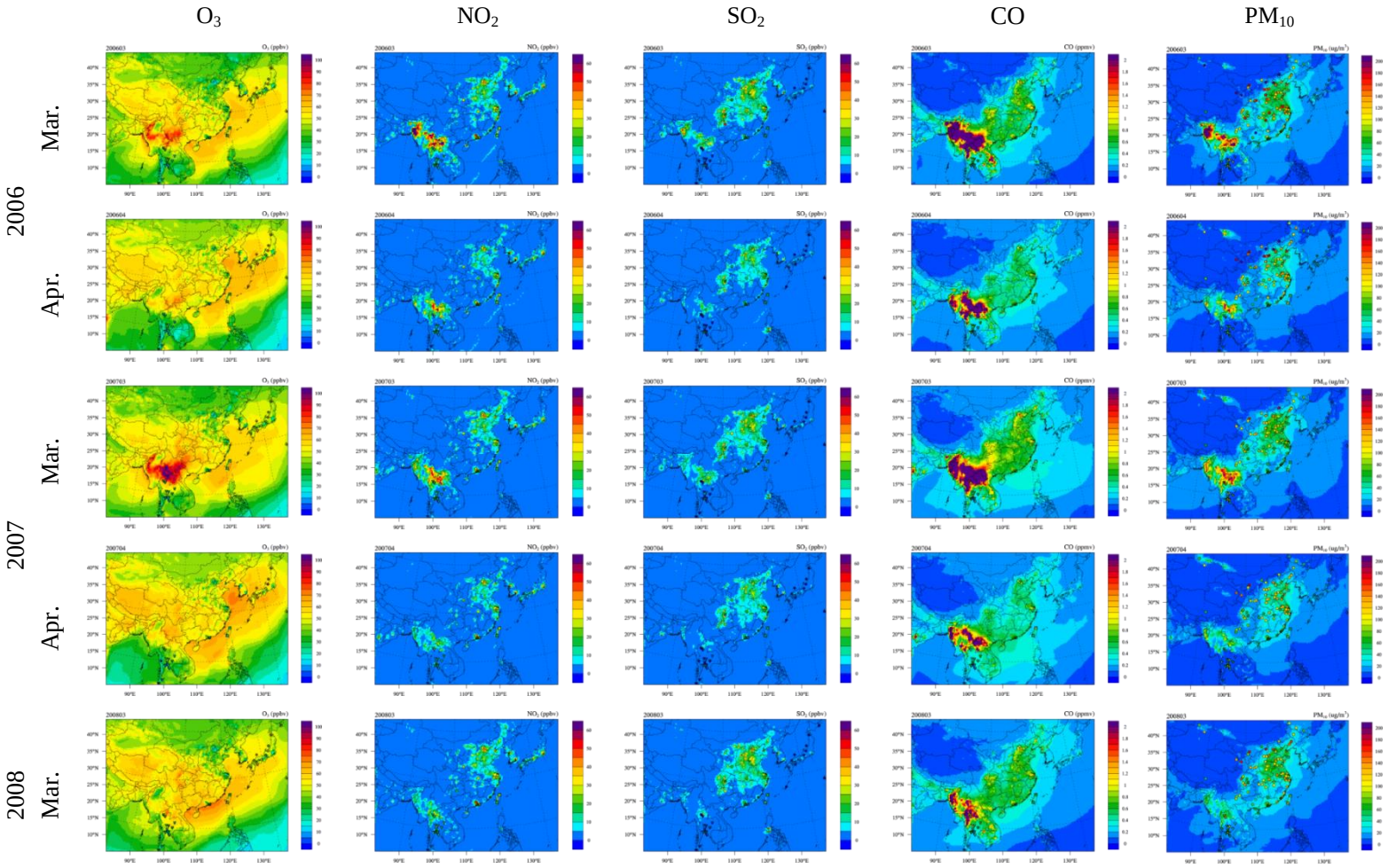

Figure 3.2 Continued

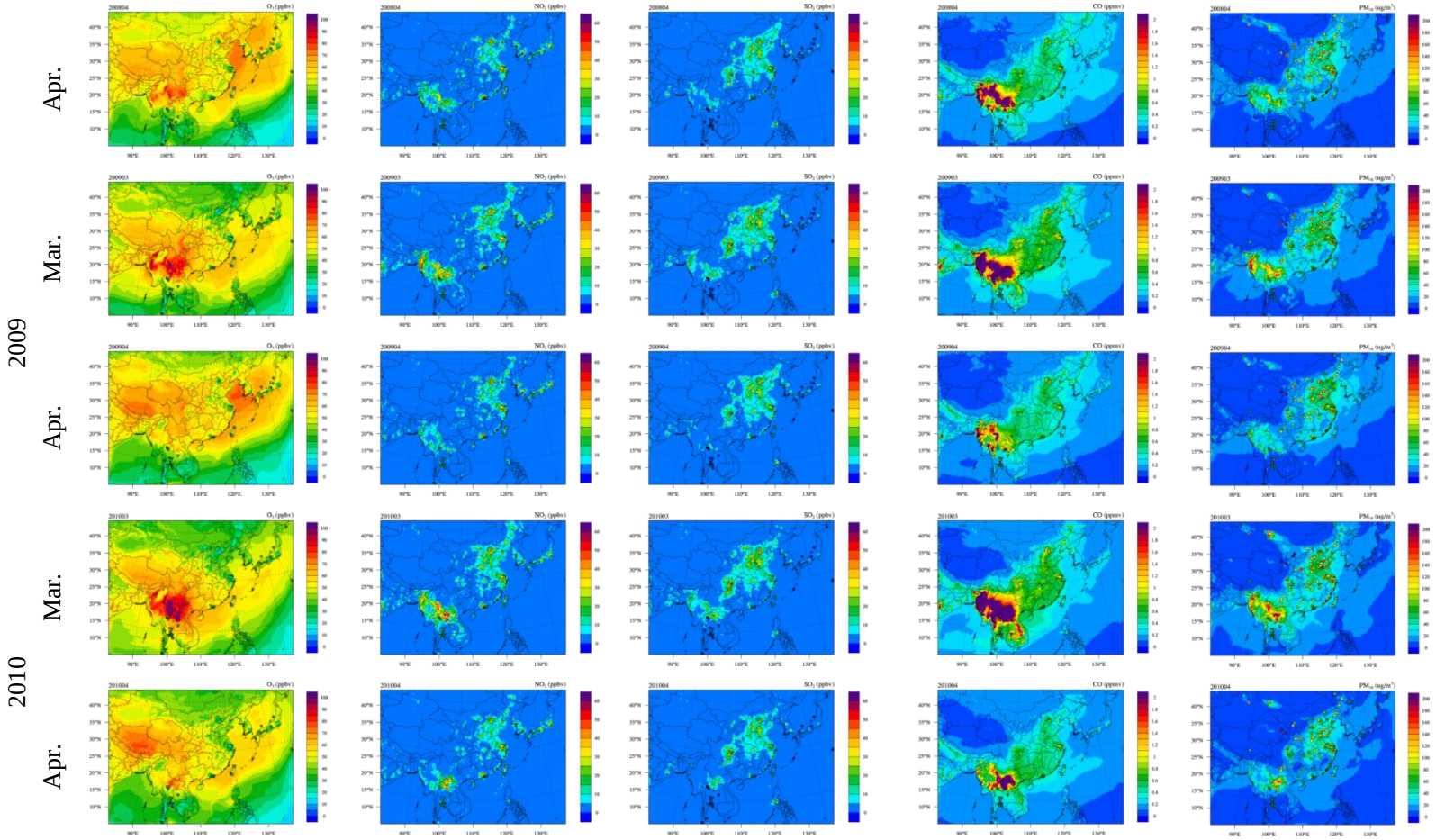

Figure 3.2 Continued

Table 3.2 Evaluation statistics for surface concentrations of O_3, NO_2, SO_2, CO, PM_{10}, and $PM_{2.5}$

	PSEA*										EA#				
	North					South									
	obs	sim	NMB (%)	R	# of data pairs	obs	sim	NMB (%)	R	# of data pairs	obs	sim	NMB (%)	R	# of data pairs
CO (ppbv)															
2006	690.01	803.98	16.52	0.71	139	452.58	455.91	0.73[$]	0.61	504	619.56	641.69	3.48	0.73	106
2007	861.72	910.81	5.69	0.72	123	511.79	425.32	-11.32	0.66	551	619.17	639.41	3.27	0.68	101
2008	678.43	809.89	19.37	0.63	129	471.11	397.43	-15.63	0.64	623	608.36	628.48	3.31	0.77	106
2009	654.26	820.51	21.45	0.67	262	449.27	382.37	-16.89	0.71	546	527.49	538.24	2.04	0.74	105
2010	926.95	1137.45	22.71	0.72	254	559.62	496.27	-19.34	0.66	624	554.43	566.34	2.15	0.79	105
SO_2 (ppbv)															
2006	1.51	2.18	44.05	0.64	123	4.77	5.12	7.29	0.52	399	6.57	8.09	23.25	0.96	257
2007	2.35	2.96	26.19	0.66	120	3.97	4.15	4.26	0.53	301	3.67	4.49	22.55	0.97	251
2008	2.81	3.57	27.54	0.71	131	3.85	5.05	31.15	0.51	462	4.42	5.38	21.82	0.96	242
2009	2.63	3.82	45.59	0.69	133	3.57	4.97	39.47	0.49	368	2.97	3.61	21.57	0.96	268
2010	2.37	3.27	37.98	0.69	155	3.38	5.22	54.19	0.51	480	4.73	6.12	29.29	0.98	203
NO_2 (ppbv)															
2006	13.39	14.41	7.58	0.63	122	12.61	11.5	-9.59	0.57	540	30.04	36.19	20.46	0.79	167
2007	15.64	17.67	12.96	0.62	102	12.39	8.7	-29.25	0.56	457	22.36	28.57	27.77	0.89	208
2008	13.08	14.83	13.33	0.66	126	12.52	8.71	-30.39	0.67	534	23.15	30.35	31.09	0.90	177
2009	13.32	15.14	13.65	0.59	165	12.41	7.64	-38.41	0.61	424	19.47	25.71	32.02	0.90	180
2010	15.69	17.81	13.59	0.61	165	13.39	8.5	-36.49	0.57	468	21.46	27.81	29.57	0.92	186

Table 3.2 Continued

	PSEA*										EA#				
	North					South									
	obs	sim	NMB (%)	R	# of data pairs	obs	sim	NMB (%)	R	# of data pairs	obs	sim	NMB (%)	R	# of data pairs
O_3 (ppbv)															
2006	30.69	38.31	24.82	0.69	409	26.1	30.39	16.45	0.67	192	47.97	45.84	-4.43	0.78	677
2007	37.13	43.75	17.82	0.63	383	29.98	38.29	27.68	0.76	186	50.07	45.94	-8.26	0.77	664
2008	37.18	46.81	25.89	0.63	423	28.47	39.2	37.67	0.82	193	49.36	46.81	-5.18	0.77	621
2009	34.23	44.61	30.03	0.86	405	27.83	37.07	33.17	0.8	216	47.59	46.72	-1.83	0.77	660
2010	41.68	54.17	29.96	0.66	447	32.72	45.75	39.95	0.86	155	43.76	42.19	-3.58	0.76	640
PM_{10} ($\mu g/m^3$)															
2006	47.07	37.19	-20.98	0.83	100	29.19	16.25	-44.32	0.84	183	111.84	45.31	-59.49	0.54	4789
2007	81.3	51.06	-37.04	0.92	181	36.53	20.08	-45.04	0.7	186	91.78	45.64	-50.27	0.48	4719
2008	69.95	50.12	-28.34	0.81	174	32.22	16.38	-49.16	0.88	207	95.95	47.09	-50.92	0.51	4663
2009	101.05	67.03	-33.67	0.89	158	34.14	15.76	-53.83	0.91	158	89.35	46.78	-47.64	0.54	4887
2010	117.95	78.46	-33.48	0.85	186	40.05	20.22	-49.52	0.82	213	89.92	41.95	-53.35	0.53	4682
$PM_{2.5}$ ($\mu g/m^3$)															
2006											42.12	34.51	-18.07	0.83	118
2007											34.99	33.62	-3.89	0.85	119
2008											43.95	37.09	-15.68	0.83	117
2009											30.29	29.64	-2.23	0.82	120
2010											31.86	27.9	-12.45	0.81	120

*. Observations used for PSEA evaluation include O_3, CO, SO_2, NO_2, and PM_{10} from PCD, and O_3, NO_2, SO_2, PM_{10} from EANET stations within PSEA.

[#.] Observations used for EA evaluation include PM_{10}, SO_2, NO_2derived from 6 cities of API in China, PM_{10} derived from 86 cities of China, O_3, CO, SO_2, NO_2, PM_{10}, $PM_{2.5}$ from TAQMN super sites, O_3, CO, SO_2, NO_2, $PM_{2.5}$,from HKEPD, and O_3, SO_2, NO_2, PM_{10} from EANET stations within EA.

[$.] Bold NMB values indicated increasing model discrepancy from 2006 to 2010.

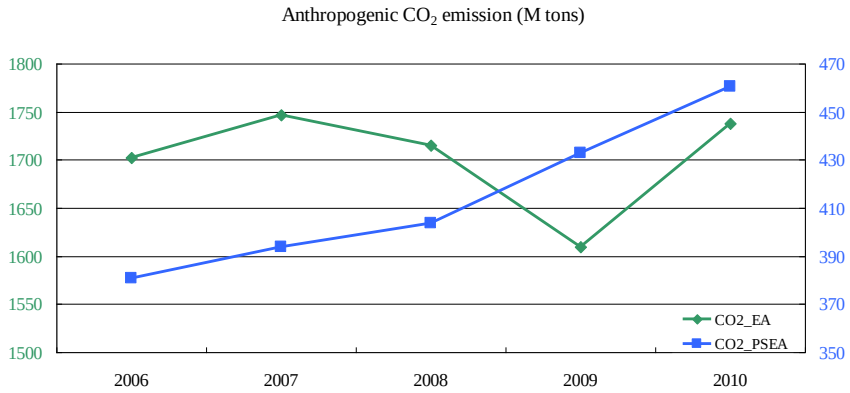

Figure 3.3 Annual anthropogenic CO_2 emission for East Asia (EA) and PSEA

stable as suggested by Table 3.1, the increasing trend of simulation bias over north part of PSEA suggests the substantial growth of anthropogenic emission from 2006 to 2010.
The CMAQ simulation shows relatively stable modeling bias over East Asia for different years during the study period. CMAQ overestimates CO, SO2, and NO2 by 2%~3.5%, 21.6%~29.3%, and 20.5%~32% respectively; and underestimates O3, PM2.5, and PM10 by -8.3%~-1.8%, -18%~-2.3%, and -47.6%~-59.5% respectively.

Anthropogenic emission over China is from Zhao et al. [2013], and anthropogenic emission over other countries in the modeling domain is from the INTEX-B inventory, as introduced in Chapter 2. The inventory from Zhao et al. [2013] is regularly updated based on annual reports, but no update has been made to the INTEX-B inventory. Thus the uncertainty within the INTEX-B inventory should affect modeling results over both East Asia and PSEA. But the increasing trend of simulation bias is found only over PSEA, indicating that the anthropogenic emission at East Asia contains less variability from 2006 to 2010. To verify the implication suggested by evaluation statistics, Figure 3.3 shows the CO2 emission trend as an indicator for PSEA and East Asia (Japan and South Korea only) to demonstrate their annual variations.

CO2 emission data shown in Figure 3.3 is collected from the World Bank (http://datacatalog.worldbank.org/). Note that EA in Figure 3.3 only includes Japan and South Korea, because anthropogenic emission over China is not from the INTEX-B inventory. On one hand, annual CO2 emission is relatively stable as 1,700~1,705 M tons (1e6 tons) from 2006 to 2010 over EA. The year 2009 has lower emission due to the economic recession started from the end of 2008. While for PSEA on the other hand, anthropogenic CO2 emission increases monotonically from 2006 to 2010 by 21%. The distinct annual trends of CO2 emission shown in Figure 3.3 suggest that, the real anthropogenic emission over PSEA should have substantial growth while the emissions over Japan and South Korea have no significant change. So CMAQ simulation bias over south part of PSEA increases from 2006 to 2010 because of the increasing discrepancy within the INTEX-B inventory.

Figure 3.4 shows the comparisons of daily CO concentrations between simulations and observations at selected sites in Thailand. Previous studies reported that

only north part of Thailand is affected by biomass burning [Huang et al., 2013], and the south part of Thailand is dominated by anthropogenic emission from industry and power facilities [Pham et al., 2007]. Four representative sites are selected in this section to evaluate the model performance and identify the simulation uncertainties. These sites include: Lampang at north Thailand, Ayuthaya at central Thailand, and Samut Sakorn and Chachoengsao at south Thailand. Simulations from CMAQ show good agreement with surface observations at these PCD sites. The CMAQ simulation bias for CO at north Thailand is mainly induced by uncertainty within the biomass burning emission since meteorology field is well reproduced the WRF model. Several published studies have suggested that the FLAMBE inventory may moderately overestimate biomass burning emission over PSEA. Fisher et al. [2010] reported that the FLAMBE inventory was overestimated by a factor of two. Alvarado et al. [2010] suggested that the FLAMBE inventory should be reduced by 45% over Southeast Asia to match with the local observation. In this study the simulation bias indicates that FLABME is overestimated by 20%~30% for the four selected sites shown in Figure 3.4.

Discrepancy in the spatial distribution of the anthropogenic emission may also induce simulation bias. Following the approach suggested by Streets et al. [2003], the INTEX-B inventory redistributes the top-down derived emission into model grids based on surrogate GIS distributions of population. While the spatial distributions between emission and population may not be consistent, this approach may allocate anthropogenic emission into incorrect model grids. In this section the emission and population density is investigated at south part of Thailand to probe into the possible uncertainty induced by spatial allocation of anthropogenic emission. Figure 3.5(a) shows the INTEX-B anthropogenic SO2 emission from power plant in model grids. Data from Carbon Monitoring for Action (CARMA, http://carma.org/) is collected to mark the locations of large power plants with annual capacity greater or equal to 1e6 MWh in this area, as shown by cycles in Figure 3.5(a). CARMA [Wheeler and Ummel, 2008; Ummel K., 2012] is a database containing information of the carbon emissions from worldwide power plants. Locations of power plants suggested by CARMA are also consistent with Thailand's local bottom-up inventory reported by Thao et al., [2014]. Figure 3.5(a) shows

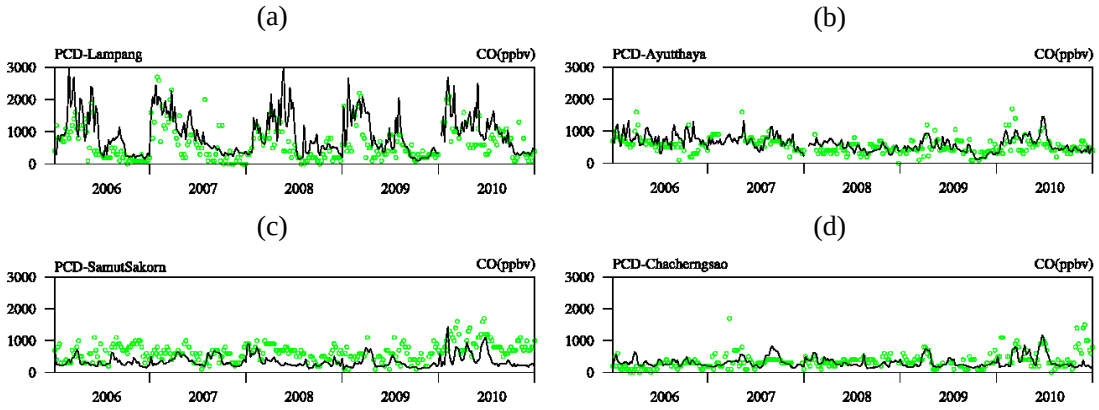

Figure 3.4 Daily variation of CO at (a) Lampang, (b) Ahuthaya, (c) Samut Sakorn, and (d) Chacherngsao. Green markers represent observations and solid black lines represent CMAQ simulations

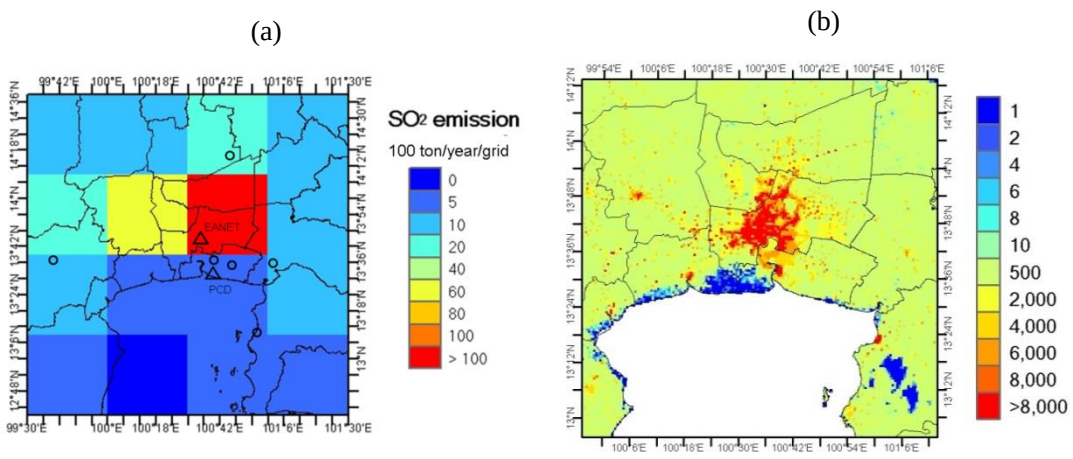

Figure 3.5 (a) Spatial distribution of anthropogenic SO_2 emission from power plant sector, the locations of EANET and PCD observational station (triangles), and the locations of large power plants (cycles); (b) Population density over the Gulf of Thailand.

that there is no large power plant located inside the urban area of Bangkok, but the INTEX-B inventory allocates most of the SO_2 emission into the model grid in Bangkok due to its high population density. Figure 3.5(b) shows the population distribution derived from the LandScan dataset over this area. Spatial distribution of the INTEX-B inventory is consistent with population, but inconsistent with the power plant locations. So Figure 3.5 demonstrates that the INTEX-B inventory is improperly distributed over Thailand, which should be responsible for the simulation bias over south part of PSEA.

Figure 3.6 shows daily variations of O_3, NO_2, SO_2 and PM_{10} at Samut Prakan and Bangkok. Observations are collected from PCD and EANET. The positions of the two stations are marked in Figure 3.5(a). The CMAQ simulation successfully reproduces the concentrations and temporal variations of air pollutants at Samut Prakan, but the model overestimates air polltuants significantly at Bangkok. Average SO_2 concentrations from observation and simulation are 4.5ppbv and 7.3ppbv respectively at Samut Prakan, and 4.5ppbv and 20.1 ppbv respectively at Bangkok. Simulation bias for NO_2, O_3, and PM_{10} at Bangkok is also greater than that at Samut Prakan. As south part of Thailand receives little impact from biomass burning, the simulation bias at Bangkok should be associated with uncertainty within the INTEX-B inventory. Population density in Bangkok is higher than that in Samut Prakan as shown in Figure 3.5(b). So the INTEX-B inventory allocates higher anthropogenic emission into the Bangkok model grid, and causes larger simulation bias as compared with Samut Prakan. The results shown by Figure 3.5 and Figure 3.6 suggest that systematic bias may exist in within the INTEX-B, as anthropogenic emission is overestimated at highly populated area but underestimated at industry area.

Evaluation statistics shown in Table 3.2 also suggest systematic simulation bias over East Asia. So in this section the modeling uncertainty over East Asia is investigated. Figure 3.7 shows the daily variations of NO_2, SO_2, and PM_{10} at Beijing, Guangzhou, and Banyu. These three sites are selected to represent the north, south, and northeast part of East Asia respectively. As shown in Figure 3.7(a) and (b), PM_{10} concentration in Guangzhou is much lower than that in Beijing, and the CMAQ simulation also agrees better with observation at Guangzhou. The average observed and simulated PM_{10} at Guangzhou are 77.2$\mu g/m^3$ and 62.9$\mu g/m^3$ respectively, while the concentrations at

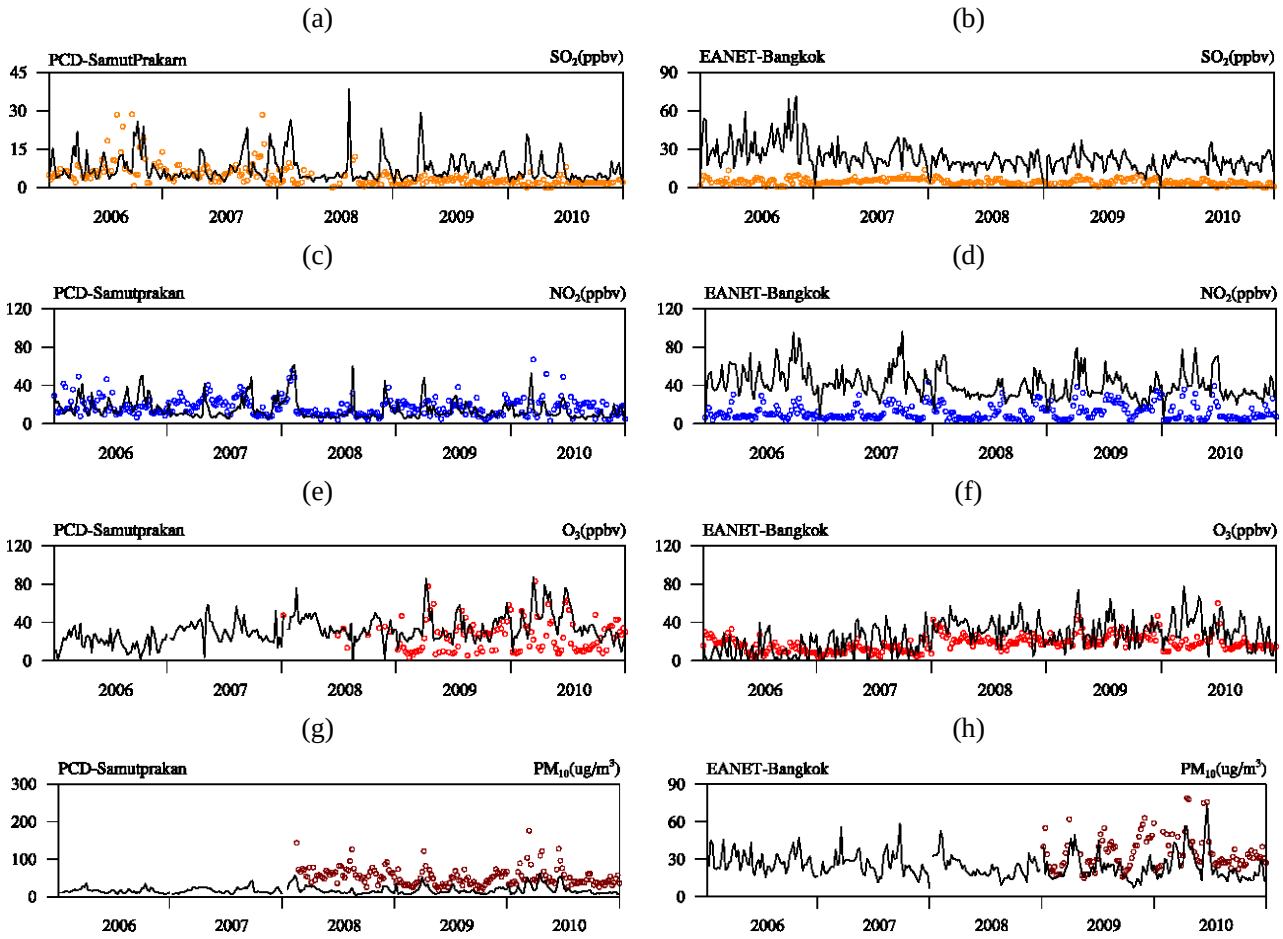

Figure 3.6 Daily variations of SO_2, NO_2, O_3, and PM_{10} at Samut Prakan and Bangkok. Markers represent observations and solid black lines represent CMAQ simulations

Beijing are 152.1μg/m^3 and 64.7μg/m^3 respectively. CMAQ also underestimates PM_{10} at Banyu. Guangzhou is located at south China where anthropogenic emission is the dominant contributor for PM_{10}. Figure 3.7(b) suggests a reasonable good estimation of the anthropogenic emission at south China. The relatively large PM_{10} simulation bias at Beijing and Banyu should be associated with the impact from dust storms. Spring dust storms generated from the Taklimakan and Gobi deserts have significant impact on the elevated PM_{10} concentration over north part of China, South Korea, and Japan [*Onishi et al.*, 2012; *Shimizu et al.*, 2014; *Watanabe et al.*, 2014; *Yang et al.*, 2013]. The large simulation bias of PM_{10} at Beijing and Banyu suggests that the wind-blown dust emission is not well reproduced by the CMAQ system. Fu et al. [2014] reported that the default friction velocity threshold should be reduced by half in order to drive the model to generate sufficient dust emission to meet with observation. Figure 3.7(d) and (e) show that CMAQ generally reproduces the daily variation of SO_2 with moderate overestimation at Beijing and minor underestimation at Guangzhou. The simulation bias slightly increases from 23.3% in 2006 to 29.3% in 2010. China initiates the anthropogenic emission control during the 11th five-year-plan from 2006 to 2010 [*Dong et al.*, 2015a]. The Zhao et al. [2013] inventory may omit some of the emission deductions since implementation of control technologies have large regional and temporal variations on national scale. Figure 3.7(g) and (h) show that NO_2 is overestimated by 40% at both Beijing and Guangzhou. Figure 3.7(f) and (i) show that the CMAQ model reproduces the daily variations of SO_2 and NO_2 well with some minor overestimations at Banyu.

3.4.3 **Evaluation of column densities**

Vertical column density (VCD) of NO_2 and AOD are also evaluated to investigate the model performance for predicting vertical distribution of air pollutants. Monthly average tropospheric VCD of NO_2 is compared with OMI products as shown in Figure 3.8. The evaluation statistics are summarized in Table 3.3. The CMAQ output at 2:00 PM Beijing Time (BT) is selected to make it comparable with the OMI products.

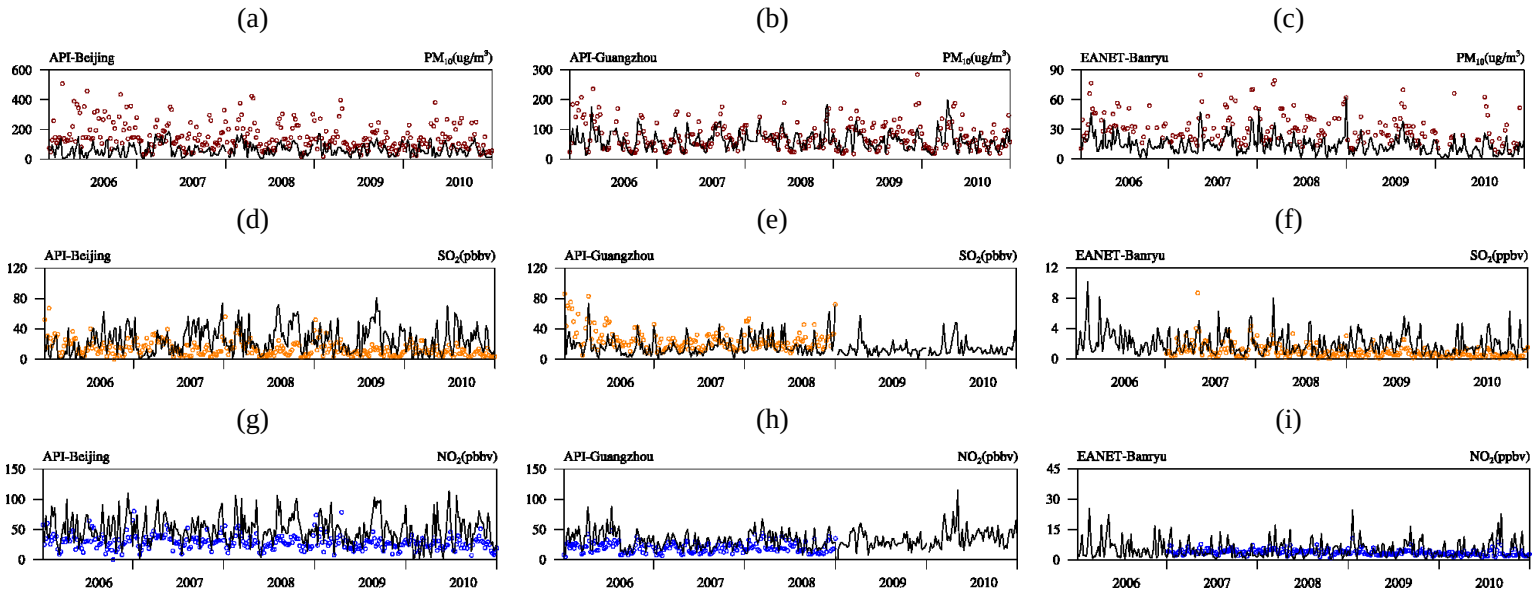

Figure 3.7 Daily variations of PM_{10}, SO_2, and NO_2 at Beijing, Guangzhou, and Banyu. Markers represent observations, solid black lines represent CMAQ simulations

Figure 3.8 Spatial distributions of VCD NO_2 from the OMI product and CMAQ simulation at 2:00 PM BT

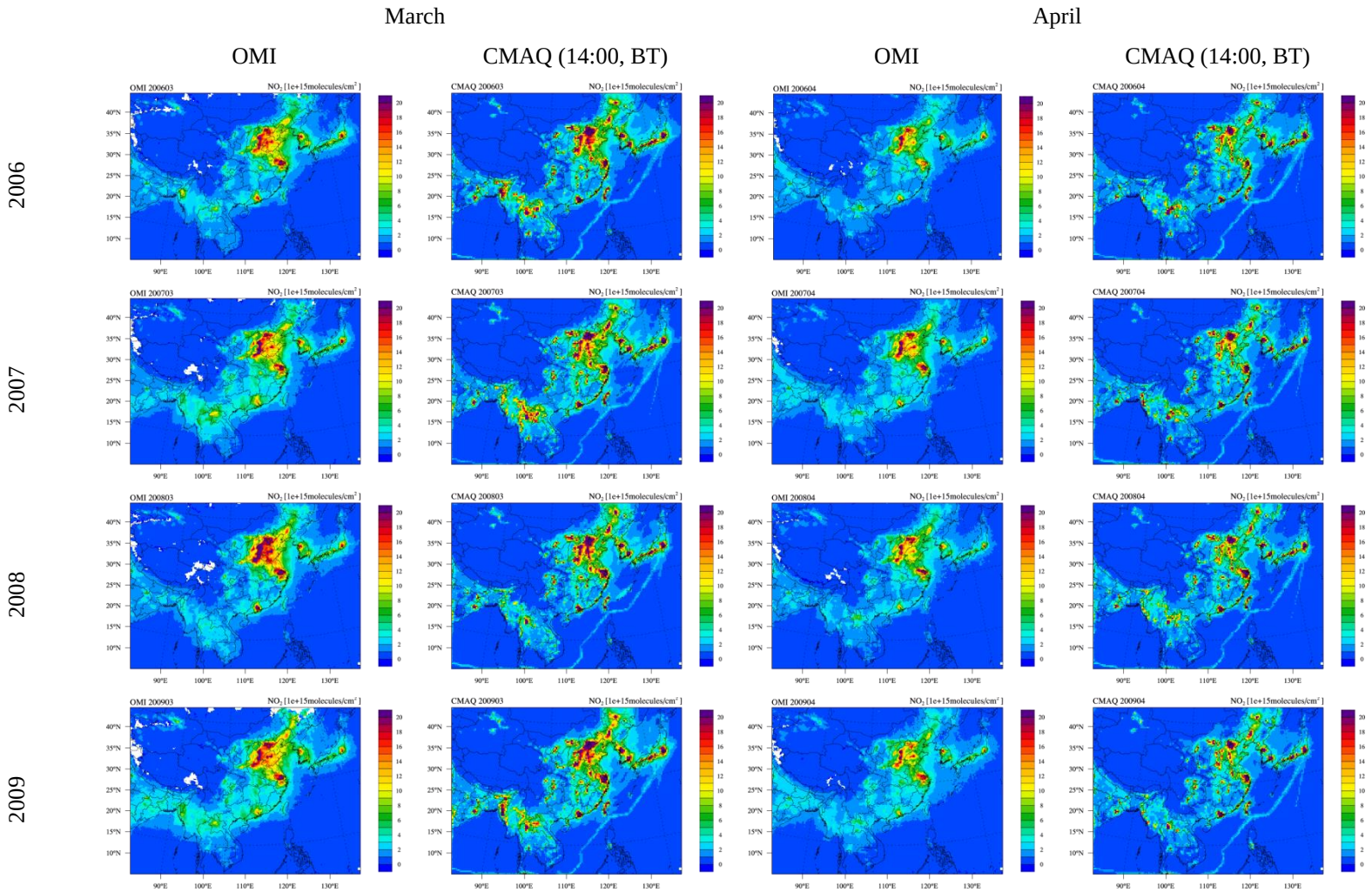

Figure 3.8 Continued

2010

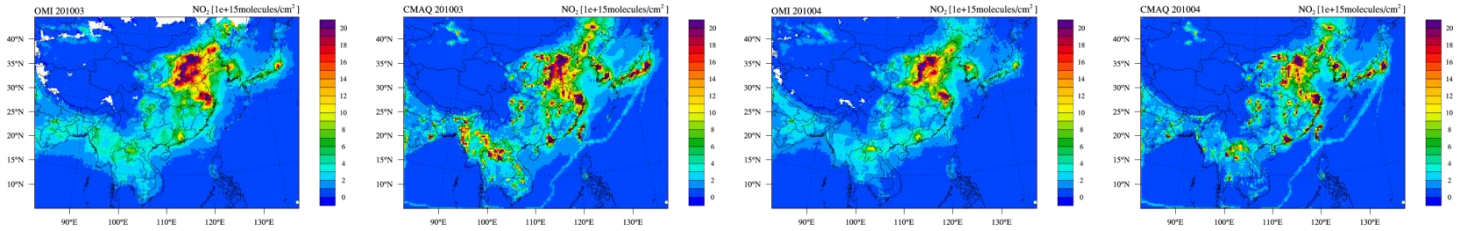

Figure 3.8 Continued

Table 3.3 Evaluation statistics for VCD NO_2

	PSEA								East Asia			
	North				South							
	obs*	sim*	NMB[#]	R	obs	sim	NMB	R	obs	sim	NMB	R
2006	1.08	1.51	39.63	0.61	0.61	0.54	-11.62	0.89	1.57	1.64	4.44	0.85
2007	1.26	1.73	37.11	0.64	0.61	0.45	-24.59	0.87	1.69	1.71	0.79	0.83
2008	1.09	1.53	40.44	0.61	0.61	0.48	-20.18	0.88	1.65	1.72	4.19	0.84
2009	1.25	1.83	46.32	0.62	0.59	0.44	-25.58	0.87	1.73	1.81	4.27	0.84
2010	1.29	1.92	49.02	0.64	0.59	0.41	-32.77	0.87	1.91	1.93	1.61	0.87

*Unit is 1e15 molecules/cm^2

[#] Unit is %

Simulation shows an overall good agreement with satellite product, but large overestimation is identified over north part of PSEA. Figure 3.8 shows the spatial distributions of tropospheric VCD NO_2 from CMAQ and OMI. Simulation bias of VCD NO_2 is -32%~-11% and 37%~49% over the south and north part of PSEA respectively, which is quite consistent with the surface NO_2 evaluation discussed in last section. Biomass burning NO_x emission is derived based on emission factor from Akagi et al. [2011]. In a recent study, Castellanos et al. [2014] used OMI products and reported that NO_x emission factor had substantial spatiotemporal variability. Emission factor for deforestation fire in dry season reported by Castellanos et al. [2014] is about 46% less than the value reported by Akagi et al. [2011]. Since deforestation is one of the major types of biomass burning over PSEA [*Reid et al.*, 2009], the overestimated NO_x emission factor should be responsible for the positive simulation bias of VCD NO_2.

Simulation of AOD is evaluated with both the MODIS product and the AERONET ground measurements. The CMAQ simulation is extracted for 11:00AM local time to make it compatible with the Terra-MODIS descending node. The daily averages from CMAQ simulation are compared with AERONET measurements. Figure 3.9 shows the comparison of AOD between the MODIS product and CMAQ simulation. Figure 3.10 shows the comparison of AOD between the AERONET measurements and CMAQ simulation. The model successfully reproduces the spatial distributions of AOD as compared to both MODIS and AERONET. AOD is high over East Asia at the North China Plain, Pearl River Delta, and Yangtze River Delta, due to the intensive anthropogenic emission from these industrial areas. High AOD is also found over southwest part of China and north part of PSEA due to the impact from biomass burning. The evaluation of AOD with both MODIS product and AERONET measurements suggest the CMAQ model generally reproduces the column density of aerosol, as shown by the evaluation statistics summarized in Table 3.4. Simulation bias is -16%~-21% over north part of PSEA, and -48%~-25% over East Asia. Since NO_2 is one of the most important precursors for production of secondary inorganic aerosol, the negative simulation bias of AOD may be associated with the underestimation of NO_2, as identified in previous sections.

Figure 3.9 Comparison of AOD from the MODIS product and CMAQ simulation at 11:00AM BT

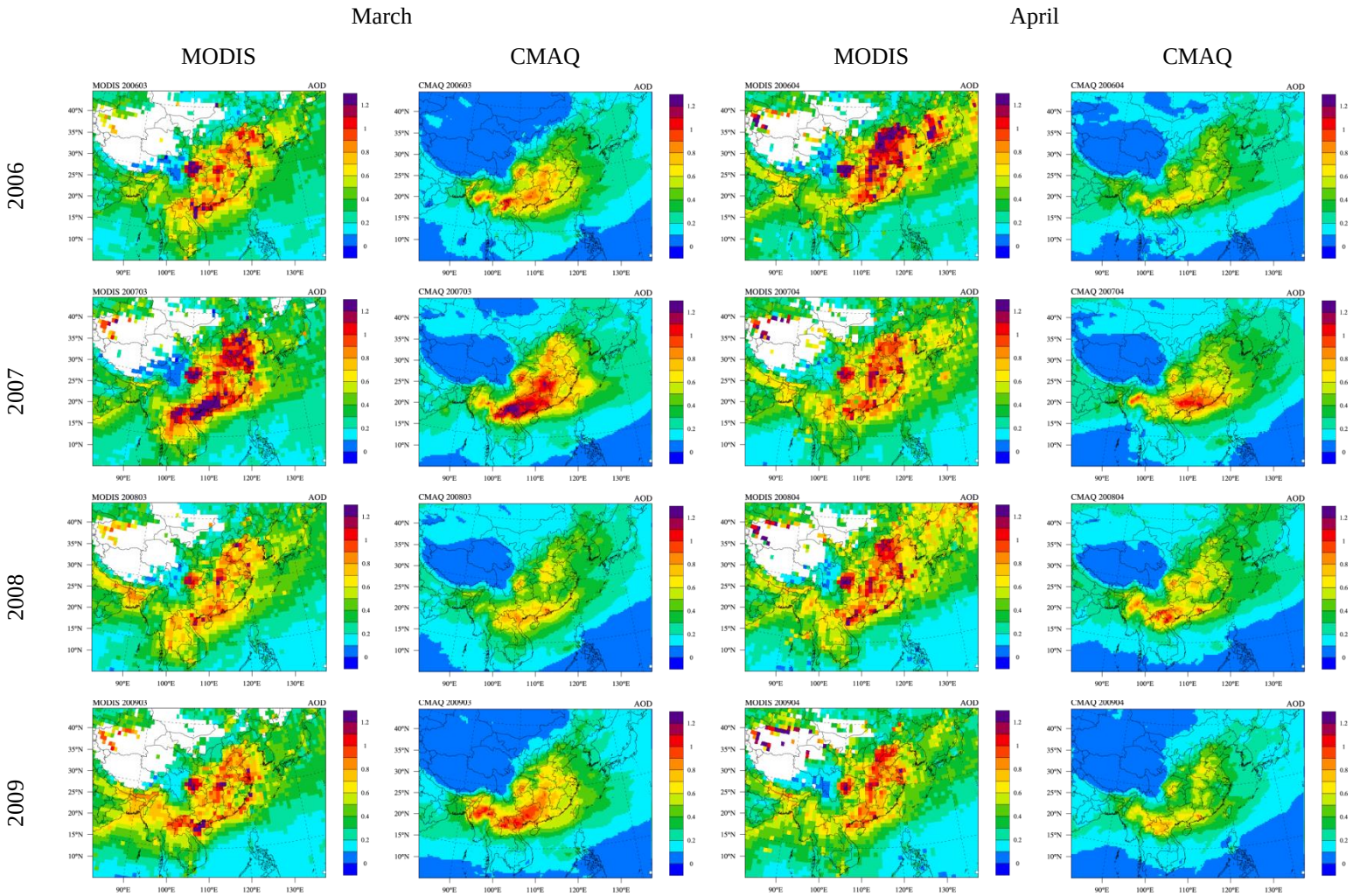

Figure 3.9 Continued

2010

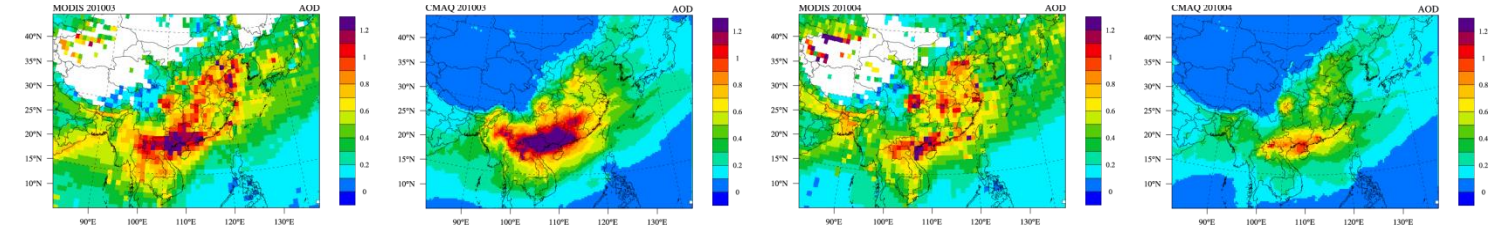

Figure 3.9 Continued

Figure 3.10 Comparison of AOD between the AERONT observations and CMAQ simulations

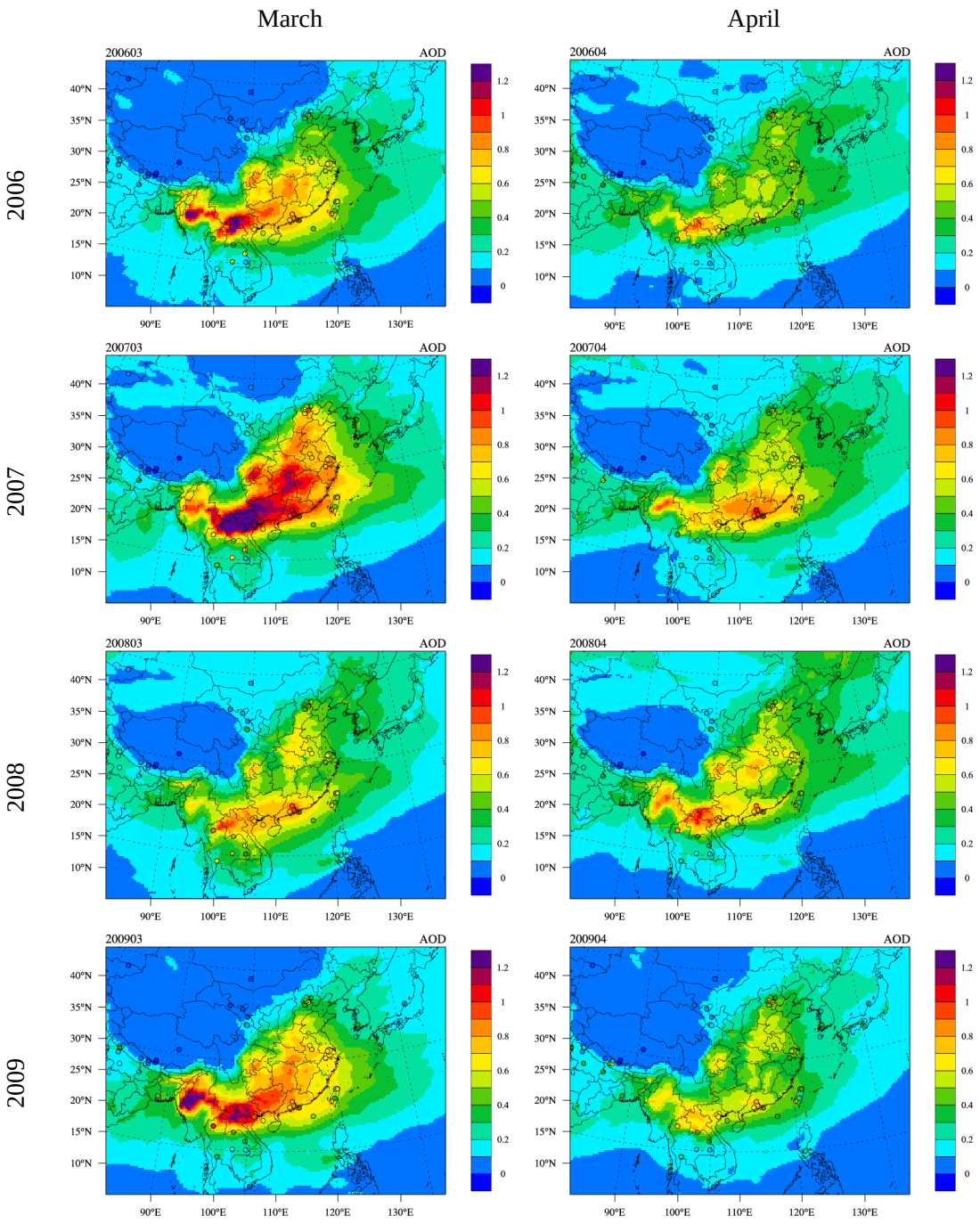

Figure 3.10 Continued

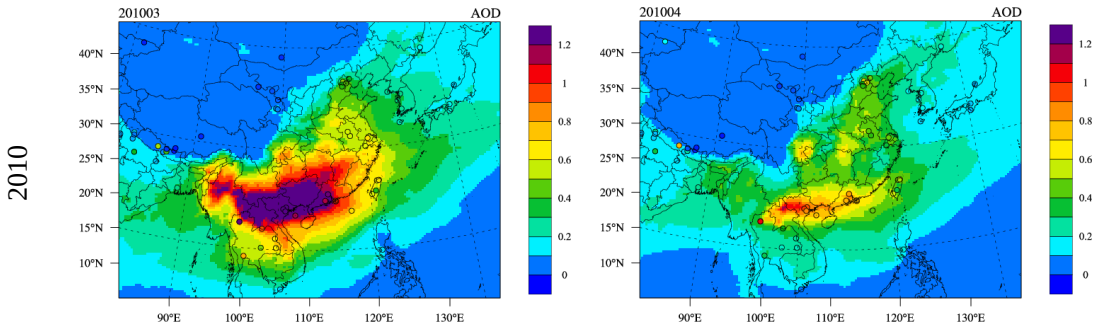

Figure 3.10 Continued

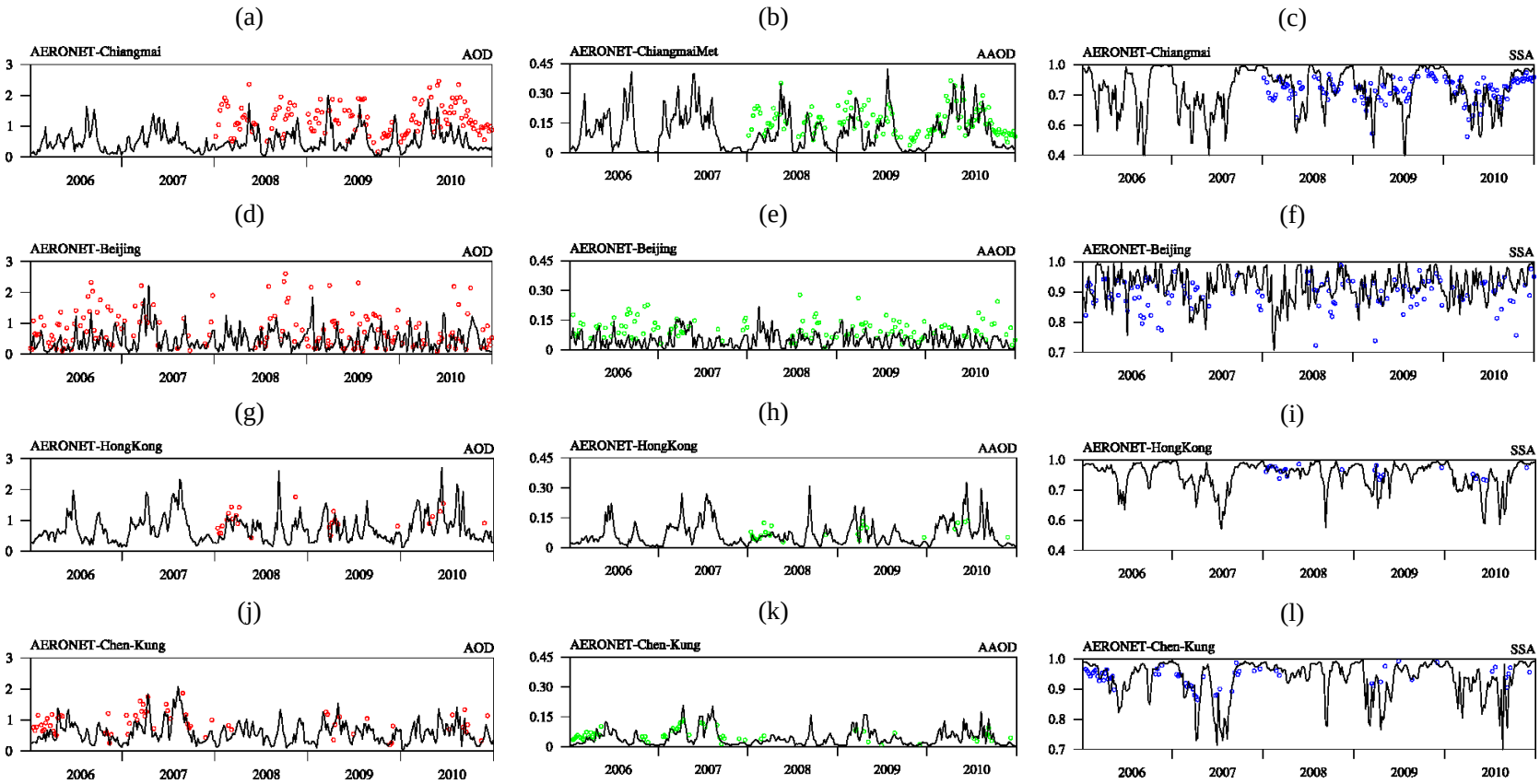

Figure 3.11 Comparison of daily variations of AOD, AAOD, and SSA between CMAQ simulations and the AERONET observations

Table 3.4 Evaluation statistics for AOD

	PSEA								East Asia			
	North				South							
	obs	sim	NMB (%)	R	obs	sim	NMB (%)	R	obs	sim	NMB (%)	R
AOD (observation from MODIS)												
2006	0.52	0.42	-19.84	0.84	0.37	0.21	-46.19	0.92	0.41	0.21	-48.22	0.87
2007	0.62	0.49	-21.36	0.82	0.32	0.13	-58.82	0.87	0.41	0.26	-38.32	0.89
2008	0.57	0.45	-20.33	0.85	0.36	0.15	-57.49	0.89	0.41	0.23	-43.45	0.91
2009	0.62	0.49	-20.83	0.75	0.29	0.12	-59.87	0.87	0.39	0.21	-47.99	0.83
2010	0.71	0.59	-15.75	0.89	0.31	0.12	-62.13	0.81	0.39	0.21	-47.53	0.85
AOD (observation from AERONET)												
2006	0.65	0.46	-24.42	0.79	0.59	0.34	-42.69	0.87	0.61	0.34	-44.96	0.74
2007	0.78	0.56	-28.35	0.82	0.57	0.22	-62.21	0.71	0.61	0.44	-27.87	0.86
2008	0.91	0.78	-14.16	0.76	0.57	0.29	-49.92	0.84	0.53	0.38	-26.83	0.83
2009	0.81	0.67	-16.67	0.81	0.41	0.19	-53.43	0.81	0.55	0.31	-44.08	0.77
2010	1.21	0.93	-23.13	0.91	0.53	0.18	-65.97	0.35	0.42	0.29	-30.69	0.78

Figure 3.11 shows the comparisons of daily variations of AOD, absorption aerosol optical depth (AAOD), and single scattering albedo (SSA) between CMAQ simulation and the AERONET measurements. Four sites are selected to represent the different sub-regions within the study domain. Chiangmai represents the biomass burning source area in PSEA; Hong Kong represents the downwind area of biomass burning at south China; Chen Kung represents the remove downwind area of biomass burning at Taiwan; and Beijing represent the north part of China which gets little impact from PSEA biomass burning. The CMAQ simulation underestimates AOD with moderate discrepancy at Chiangmai, but generally captures the daily variations and the massive burning events. The CMAQ simulation agrees fairly well with the AERONET measurements at both Hong Kong and Cheng Kun. At Beijing, CMAQ also successfully reproduces the daily variation of AOD with moderate underestimates due to the uncertainty from wind-blown dust scheme. Some modeling studies [*Fu et al.*, 2012; *Wang et al.*, 2011; *Zhao et al.*, 2013] also suggested that the CMAQ model usually underestimates AOD over Asia. In summary, it is essential to devote more research efforts to quantify the uncertainty within emission inventories and address the uncertainty within the modeling system.

3.5 Uplift motion and impact of biomass burning on air quality

3.5.1 **Uplift motion and transport pathway of biomass burning**

Figure 3.12 shows the spatial distributions of biomass burning impact on O_3 at near surface layer (0~1km) and upper layer (1km~3km). The impact of biomass burning is analyzed at these two selected levels because the PBL height is around 1km at subtropical and mid-latitude regions. It has been demonstrated [Huang et al. 2013] that biomass burning is transported by the Westerlies from PSEA to south China and the West Pacific. As shown in Figure 3.12(a), biomass burning contributes more than 60% (~50ppbv) of total surface O_3 in Myanmar, Laos, and northern Thailand over PSEA. The impact of biomass burning gradually declines from 20% (~15ppbv) at Vietnam to about 5%~10% (~5ppbv) at south China and Taiwan along the transport pathway. At near surface layer, the contribution of biomass burning to local O_3 concentration decreases rapidly from 40% to 20% over Yungui Plateau between 100°E to 105°E longitude. At

upper air as shown in Figure 3.12(b), contribution of biomass burning to local O_3 reaches up to 25% (30ppbv) in south China. To investigate the transport pathway and uplift motion of biomass burning plume, Figure 3.12(c) and (d) shows the biomass burning O_3 flux at 0~1km and 1~3km respectively. The biomass burning O_3 flux is defined as the contribution of biomass burning to O_3 multiplies the wind speed and wind direction. Thus the O_3 flux describes the O_3 outflow due to the impact of biomass burning. At near surface layer, O_3 flux starts from the south lee side of Tibet Plateau and moves northward shortly before it gets blocked by the higher terrain height over Yungui Plateau and Hengduan Mountains. At upper air, O_3 flux is carried by the Westerlies at the southeast flank of Tibet Plateau, and transported towards south China and the West Pacific without any barriers. The distinct O_3 fluxes at 0~1km and 1km~3km height indicate that biomass burning has a more significant impact on the upper air.

Knowledge of the biomass burning uplift mechanism is not well developed due to limited research efforts. Liu et al. [2003] claimed that deep convection is the dominate factor for PSEA biomass burning uplift motion based on GEOS-Chem simulation. But Lin et al. [2009] used tracer module in WRF/Chem and reported that the lee side trough at eastern flank of Tibet Plateau may push the biomass burning plume up to 3km height above the surface ground. The global model GEOS-Chem simulation conducted by Liu et al. [2003] may be too coarse to reproduce the regional uplift motion of biomass burning. The simulation conducted by Lin et al. [2009] also contains critical uncertainties. Lin et al. [2009] artificially allocated O_3 emission into the first model layer only (~20m), and O_3 was treated as a non-reactive tracer. However, plume rise of biomass burning emission is determined by the burning activity and meteorology condition [*Fu et al.*, 2012; *Jian and Fu*, 2014]. And primary O_3 emission from biomass burning is very limited, while the majority of O_3 is produced from primary emission of precursors. In this study the plume rise of biomass burning is calculated by following the algorithm from SMOKE [*Huang et al.*, 2013]. And the FLAMBE inventory also provides a detailed biomass burning emission input for the WRF/CMAQ modeling system. The modeling method in this study allows a more solid investigation of the uplift motion of biomass burning as compared to previous studies. Figure 3.12(f) shows the cross sectional distribution of biomass burning

Figure 3.12 Biomass burning impact on O_3 at (a) 0~1km and (b) 1~3km height; Biomass burning O_3 flux at (c) 0~1km and (d) 1~3km height; (e) Topography in simulation domain; (f) Cross sectional distributions of biomass burning impact on O_3; Geopotential height at (g) 850hPa and (h) 700hPa; (i) The LIST/OTD lightning product; and (j) The FLAMBE carbon emission

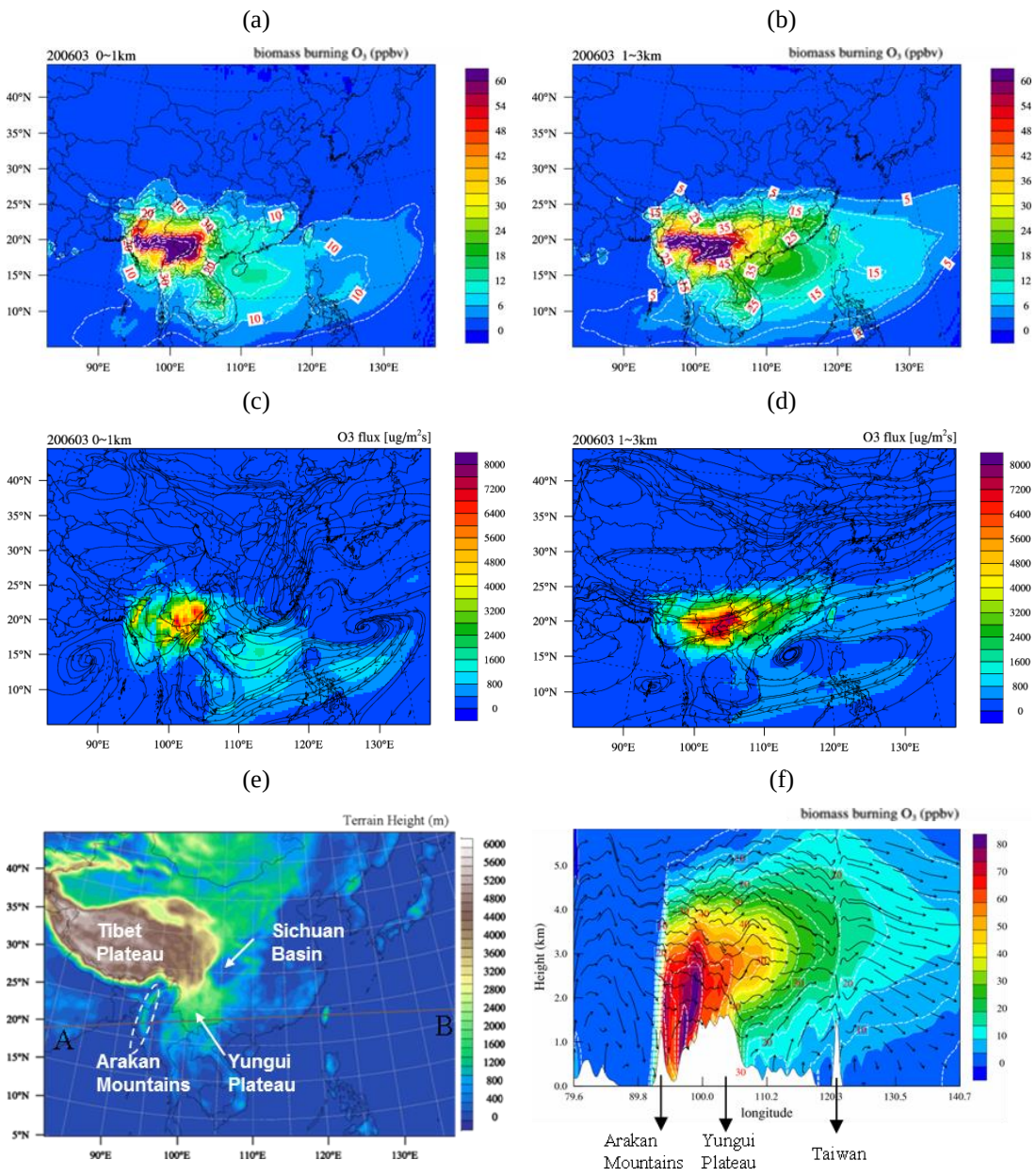

Figure 3.12 Continued

(g)

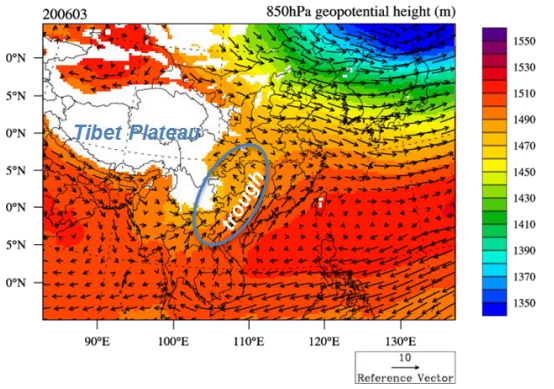

(h)

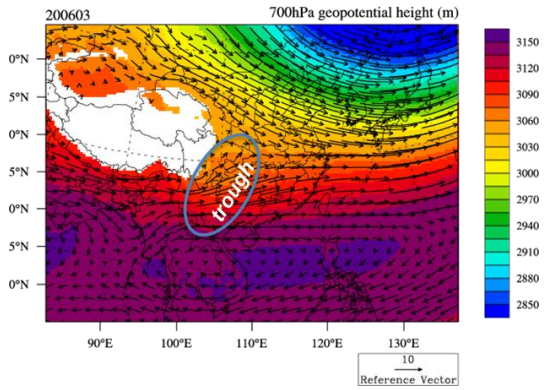

(i)

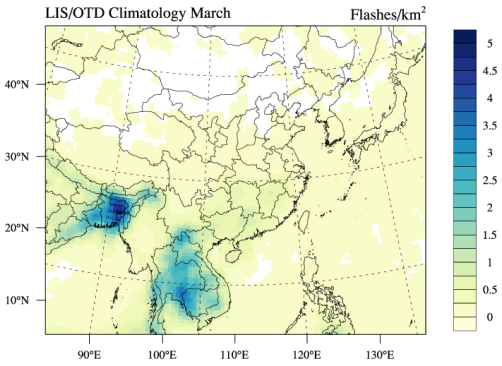

(j)

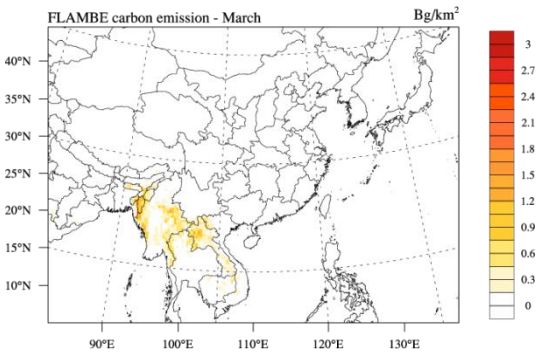

Figure 3.12 Continued

impact on O_3 following the brown line AB shown in Figure 3.12(e). Biomass burning emission is mainly allocated between 90°E ~105°E longitude over Myanmar, north Thailand, Laos, and Vietnam. The uplift motion of biomass burning brings excessive O_3 up to 6km in the free troposphere, and then the Westerlies carries the O_3 plume towards the West Pacific at 140°E longitude. The geopotential height (GPH) at 850hPa and 700hPa demonstrates the existence of lee side trough at east side of the Tibet Plateau, as shown in Figure 3.12(g) and (h). The center of the lee side trough lies between the Bay of Bengal and the South China Sea (SCS), with relatively lower air pressure than the neighboring area. Due to the impact of the lee side trough, wind direction is changed from northwest to southeast along the edge of the trough at Myanmar, northern Thailand, and Laos at 850hPa. Consequently, biomass burning plume is lifted into free troposphere over Yungui Plateau. The NASA Lightning Image Sensor and Optical Transient Detector (LIS/OTD) data suggests that deep convection is weak in March as shown in Figure 3.12(i). In addition, deep convection is identified at west side of the Arakan Mountains and south part of Thailand. But biomass burning emission is located at east side of the Arakan Mountains and north boundary of Thailand as shown in Figure 3.12(j). The inconsistent spatial distributions between LIS/OTD and FLAMBE carbon emission suggest that deep convection cannot be the major driving force for uplifting biomass burning plume. This study is the first investigation of the biomass burning uplift scheme with the WRF/CMAQ modeling system and multiple observations.

3.5.2 **Annual variations of biomass burning**

Figure 3.13 shows the impact of biomass burning at near surface layer within 0~1km height. The impact in 2008 and 2010 is selected to represent the lower and upper boundary respectively due to the changes of biomass burning emission. The five-year average impact is calculated to represent the mean contribution from biomass burning. The five-year average biomass burning contribution to O_3 is 20ppbv~60ppbv (10%~50%) at PSEA, 8ppbv~26ppbv (12%~24%) at South China, and 5ppbv~10ppbv (4%~12%) at the West Pacific. The contribution to O_3 changes from 45 ppbv in 2008 to more than 60 ppbv in 2010 at PSEA, but no significant variation is found over the downwind areas.

Figure 3.13 Biomass burning impact at near surface layer (0~1km) for O_3, $PM_{2.5}$, and CO for five-year average (1st column), 2008 (middle column), and 2010 (right column). Concentrations are plotted with filled color contours and percentage contributions are denoted by white dash lines with red labels

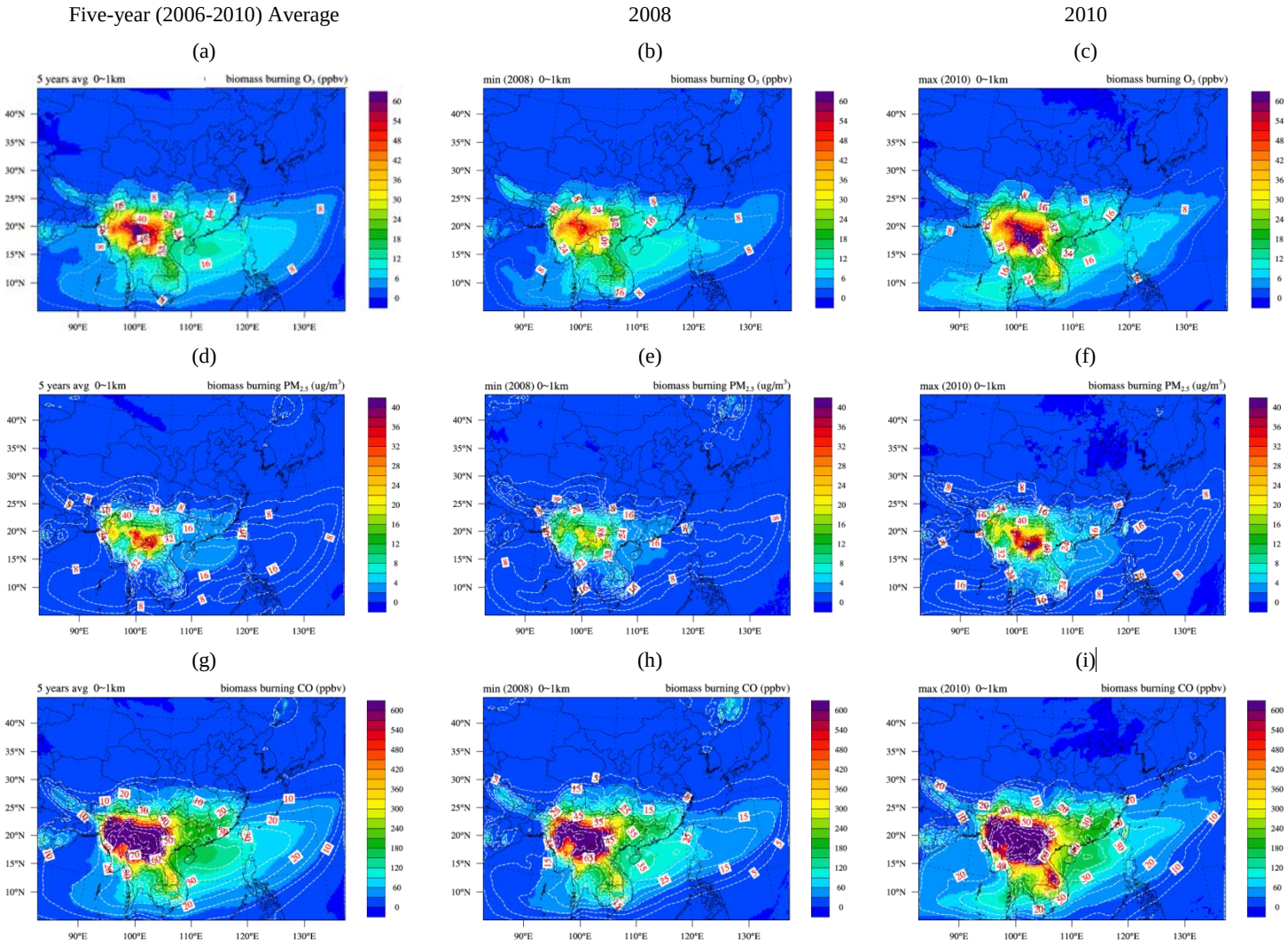

Figure 3.13 Continued

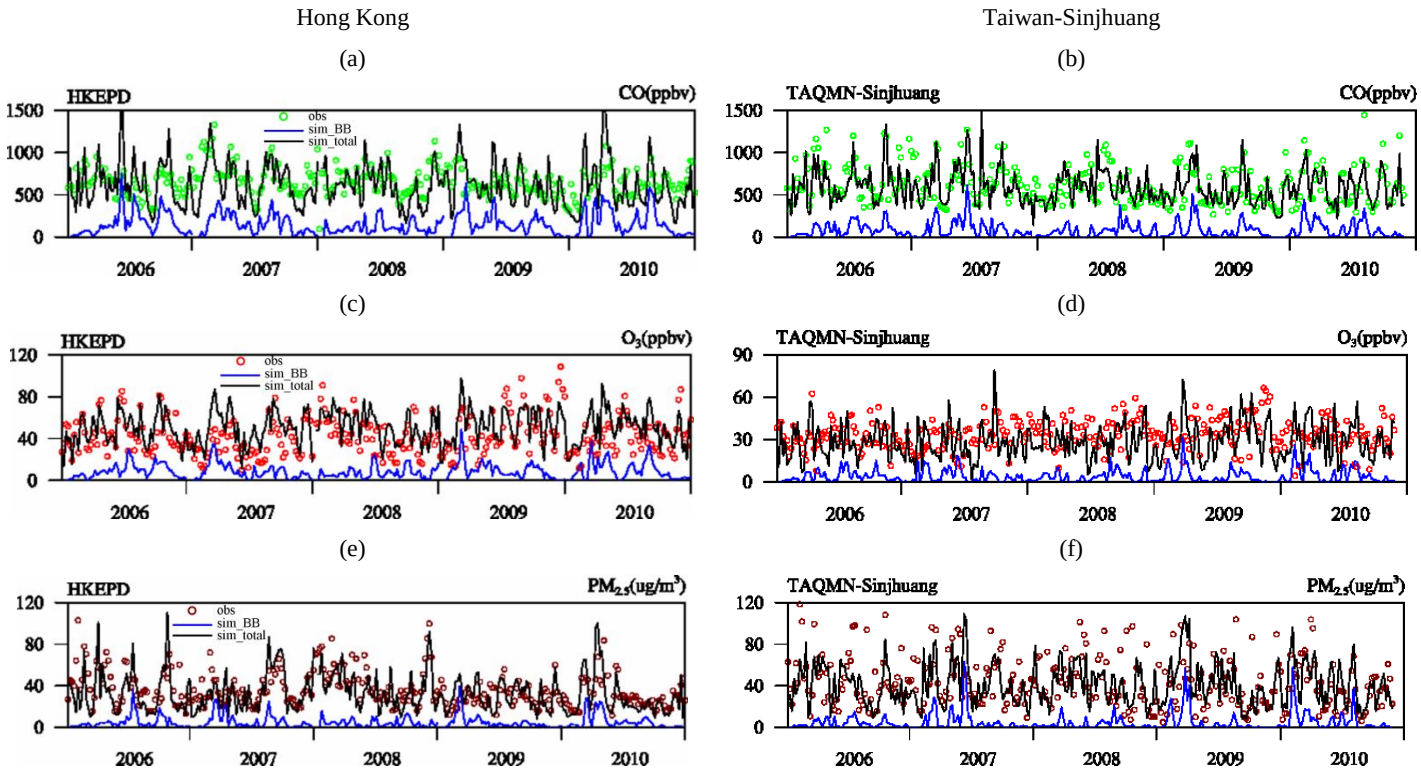

Figure 3.14 Comparison of daily variations of CO, O_3, and $PM_{2.5}$ between observation and the CMAQ simulation at Hong Kong and Taiwan-Sinjhuang. Observations are represented by markers. Black lines represent the Off_Base scenario simulation, and blue lines represent the Dust_Off scenario simulation

The biomass burning contributions to $PM_{2.5}$ and CO show consistent spatial distributions and annual variations. On five-year average, biomass burning contributes 15μg/m^3~35μg/m^3 (25%~50%), 5μg/m^3~8μg/m^3 (16%~20%), and 0~5μg/m^3 (0~16%) to $PM_{2.5}$ at PSEA, south China, and the West Pacific respectively. The contribution to CO is 400ppbv~600ppbv (35%~60%), 200ppbv~300ppbv (20%~35%), and 50ppbv~150ppbv (5%-30%) at PSEA, south China, and the West Pacific respectively. Considering the biomass burning emission in 2010 is 65% higher than that in 2008, its impact at near surface layer over downwind area has slight annual variations.

Figure 3.14 shows the comparison between the CMAQ simulations and observations at Hong Kong and Taiwan. Daily variations of CO, O_3 and PM2.5 are extracted from simulations with and without biomass burning emission to investigate the impacts. The simulation with biomass burning emission under Dust_Off scenaior shows significantly better agreement with observations than the simulation without biomass burning emission under Off_Base scenario. At Hong Kong, contributions from biomass burning for CO, O_3, and $PM_{2.5}$ range from 117ppbv(19.5%), 7.2ppbv(13.8%), and 4.3μg/m^3 (11.7%) respectively in 2008 to 164ppbv(27.1%), 9.1ppbv(18.3%), and 5.1μg/m^3 (17.2%) respectively in 2010. Contributions of PSEA biomass burning to air pollutants at Hong Kong change slightly from year to year. The inter-annual variation of biomass burning impact at Taiwan is even smaller. The contributions to CO, O_3, and $PM_{2.5}$ range from 61ppbv(10.5%), 3.2ppbv(11.3%), and 3.7μg/m^3(9.7%) respectively in 2008 to 90ppbv(15.1%), 4.1ppbv(16.1%), and 5.9μg/m^3(14.1%) respectively in 2010. The uplift motion carries majority of the biomass burning plume into upper air, and subsequently leads to the slight inter-annual variations of its impact on air quality at downwind areas.

Figure 3.15 shows the impact of biomass burning at upper air within 1km~3km height. On five-year average, biomass burning contributes 30ppbv~55pbv (25%~50%), 15ppbv~40pbv (20%~40%), and 0~15ppbv (0~20%) to O_3 at PSEA, south China, and the West Pacific respectively. The contribution to O_3 in 2008 is 25ppbv~45ppbv (20%~40%), 10ppbv~30ppbv (15%~30%), 0-10ppbv (0~15%) at PSEA, south China, and the West Pacific respectively. And in 2010 the contribution is 35ppbv~60ppbv (30%~55%),

Figure 3.15 Biomass burning impact at upper air (1km~3km) for $O_{3,}$ $PM_{2.5}$, and CO for five-year average (1st column), 2008 (middle column), and 2010 (right column). Concentrations are plotted with filled color contours and percentage contributions are denoted by white dash lines with red labels.

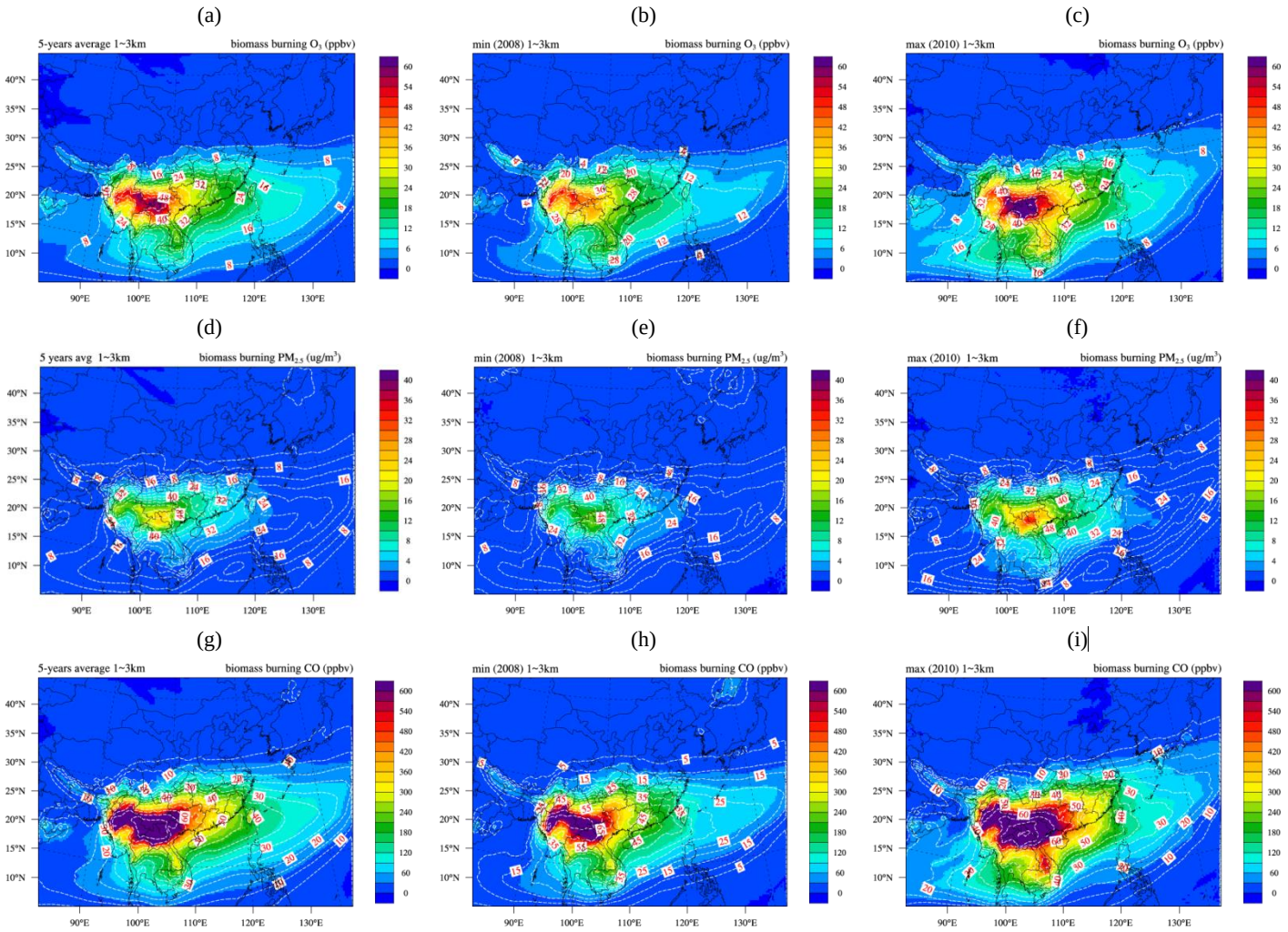

Figure 3.15 Continued

25ppbv~45ppbv (20%~45%), and 0~20ppbv (0~20%) at PSEA, south China, and the West Pacific respectively. Impact of biomass burning shows wide annual variations in the upper air. In 2010, the biomass burning contribution to O_3 is 60%~100% higher than that in 2008. Contributions to $PM_{2.5}$ and CO in upper air also show similar variations. Figure 3.14 suggest that impact of biomass burning is subject to variation only at upper air due to changes of the emission from year to year.

To better understand the uplift motion and the impact of biomass burning at near surface and upper layers, sounding data from CWB at Taiwan is compared with model simulations to investigation the vertical distribution of O_3. Figure 3.16 shows the cross sectional distribution of biomass burning O_3. The contribution of biomass burning to O_3 ranges from 30ppbv to 80ppbv in upper air during an intensive burning episode on Mar.7th 2007 as shown in Figure 3.16(a). And the contribution ranges from 10ppbv to 40ppbv in upper air during a weak burning episode on Mar.12th 2008 as shown in Figure 3.16(b). The CMA simulations are compared with sounding observations as shown in Figure 3.16(c) and (d). The simulation with biomass burning emission successfully reproduces the vertical profile of O_3. The impact of biomass burning shows slight variation at the near surface air during both episodes. At the upper air within 2km~6km height however, impact of biomass burning accounts for 30% of the total O_3. Excessive O_3 in upper air induced by biomass burning is also identified on Mar.12th 2008. About 15% of total O_3 is contributed by biomass burning. Both episodes demonstrate that major influence of PSEA biomass burning is confined within the upper air at 2~6km height, and massive burning events may cause greater influence in the upper air only.

Fu et al. [2012b] reported that the impact of PSEA biomass burning over East Asia in surface layer is 8ppbv~18ppbv, 160ppbv~360ppbv, and 8μg/m^3~64μg/m^3 for O_3, CO, and $PM_{2.5}$ respectively; Tang et al. [2003] reported that biomass burning net influence on O_3 is about 10 ppbv for the layers below 1km over East Asia. Findings from this study are consistent with the conclusions from previous studies. But this study is the first investigation of the biomass burning impact during multiple years. The distinct contribution at near surface and upper air is also systematically illustrated with simulations and observations for the first time.

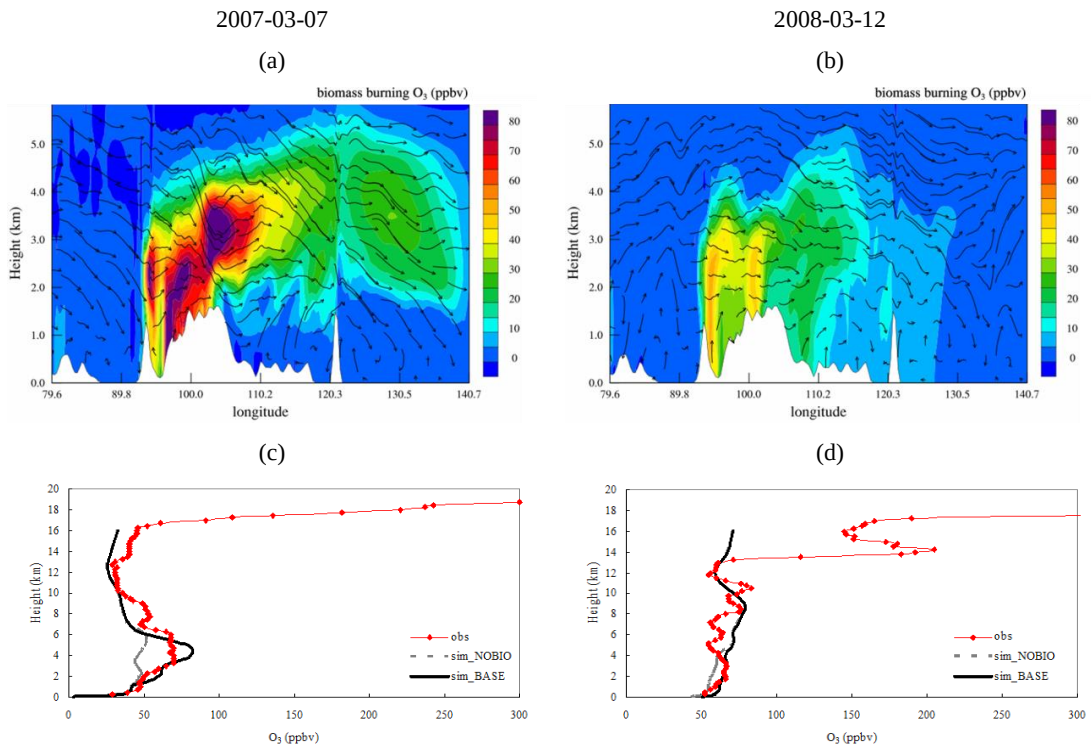

Figure 3.16 Cross sectional distribution of biomass burning O_3 and wind fields on (a) Mar.7th, 2007; and (b)Mar.12th, 2008; O_3 vertical profiles from CWB sounding data and CMAQ simulations with and without biomass burning emission on (c) Mar.7th, 2007; and (d) Mar.12th, 2008

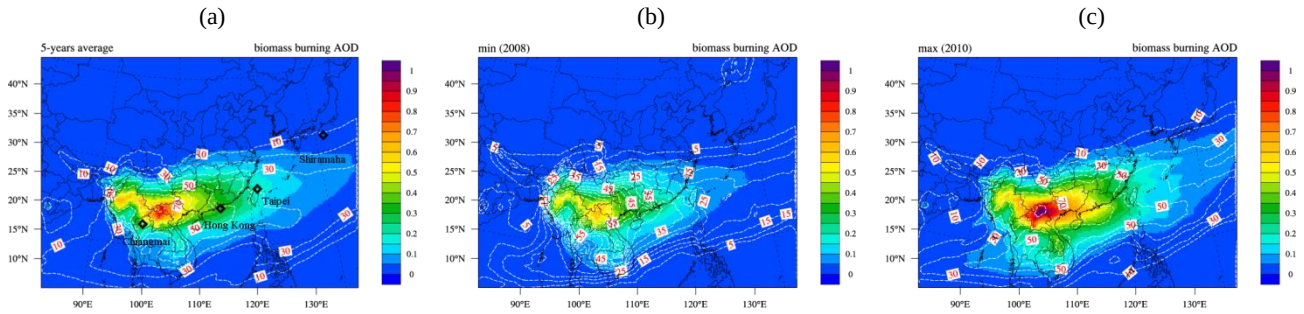

Figure 3.17 Biomass burning contribution to AOD for (a) five-year average; (b) 2008; and (c) 2010.

3.5.3 **Impact of biomass burning on AOD**

Figure 3.17 shows the impact of biomass burning on AOD. Contribution from biomass burning to AOD declines gradually along the transport pathway. The impact ranges from 40%~70% at PSEA to 30%~50% at south China, and drops to 10%~30% at the West Pacific on five-year average scale. Contribution of biomass burning to AOD is also subject to wide annual variation. It changes from 25%~55% in 2008 to 50%~70% in 2010.

Figure 3.18 compares the daily variations of AOD between The AERONET observation and CMAQ simulations at four selected sites along the transport pathway. These sites include Chiangmai, Hong Kong, Taipei, and Shirahama. Chinagmai is in the north part of Thailand, thus the AOD variation at Chiangmai represents the variability of biomass burning emission. Contribution from biomass burning to the total AOD increases from 36% in 2008 to 71% in 2010, which is fairly consistent with the emission change. At Hong Kong and Taipei, contributions from biomass burning range from 37% and 23% in 2008 to 57% and 39% in 2010 respectively. The impact of PSEA biomass burning also plays an important role for elevated AOD at these downwind areas. At Shirahama, contribution from biomass burning to total AOD increases from 2% in 2008 to 15% in 2010, indicating the limited impact of biomass burning at remote downwind area. But some high values of daily AOD are also found at Shirahama in 2007 and 2010. Biomass burning contributes more than 50% to the total AOD, suggesting that long-range transport may also have significant impact over the West Pacific during massive burning episodes

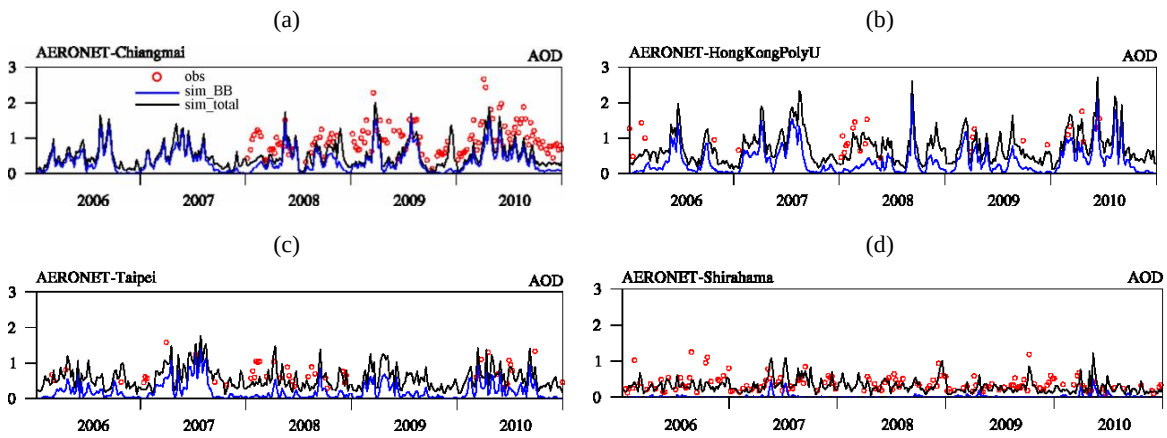

Figure 3.18 Comparison of daily average AOD between CMAQ simulations and the AERONET observations. Black lines represent the Dust_Off scenario, blue lines represent the Off_Base scenario, and red markers represent the AERONET observations

4 ASSESSMENT OF CMAQ MODEL PERFORMANCE AND INVESTIGATION OF DUST IMPACT ON AIR QUALITY

4.1 Declaration

This chapter is a slightly revised version based on the manuscript submitted to *Atmospheric Chemistry and Physics*.

4.2 Abstract

The wind-blow dust emission scheme within the CMAQ model is improved in this study. The default parameterization of threshold friction velocity constants are revised to avoid double counting of the impact of soil moisture based on reanalysis of field experiment data. The source dependent speciation profiles for dust emission are derived based on local measurements for the Gobi and Taklamakan deserts in East Asia. Dust heterogeneous chemistry is incorporated into the CMAQ model. The modified dust module in the CMAQ is applied in this study to evaluate the improvement of model performance. Simulation bias of PM_{10} and AOD is reduced from -55.42% and -31.97% in the original CMAQ to -16.05% and -22.1% in the modified CMAQ, respectively. Simulation with the source dependent speciation profile shows better agreement with observations for trace metals. Simulation with the dust heterogeneous chemistry also shows better agreement with observations for SO_2, SO_4^{2-}, HNO_3, NO_x, and NO_3^-. Based on the investigation of a severe dust storm episode from Mar.19th to Mar.21st 2010, the modified CMAQ is capable of reproducing the spatial distribution and temporal variation of dust storm. Evaluation of the CMAQ model performance suggests potential uncertainty within the excessive soil moisture used by meteorological simulation. The mass contribution of fine mode particles in dust emission may be underestimated by 50%. This study demonstrates the improvement of the CMAQ model capability based on these modifications. The revised CMAQ model provides a useful tool for future studies to investigate the emission, transport, and impact of wind-blown dust over East Asia and elsewhere.

4.3 Introduction

Natural dust has a wide impact on many different aspects of the Earth's system. It reduces atmospheric visibility [*Engelstaedter et al.*, 2003; *Kurosaki and Mikami*, 2005; *Washington et al.*, 2003], deteriorates air quality [*De Longueville et al.*, 2010; *Prospero*, 1999], alters the radiative forcing budget [*Liao et al.*, 2004; *Miller et al.*, 2006; *Reddy et al.*, 2005], and also affects the cloud properties and precipitation [*Rosenfeld et al.*, 2001; *Forster et al.*, 2007]. Over East Asia, dust storms often lead to severe air pollution problems due to the intensive aerosol loading over China [*Qian et al.*, 2002], South Korea [*Chun et al.*, 2001; *Park and In*, 2003], and Japan [*Ma et al.*, 2001; *Uno et al.*, 2001]. The estimated global source of mineral dust with diameters below 10 μm is between 1,000 and 4,000 Tg/year on global scale as reported by IPCC. Zhang et al. [2003] reported Asian dust emission is about 800 Tg/year. East Asian wind-blown dust is mainly generated from two source regions, including the Taklamakan Desert in northwest China and the Gobi Desert in Mongolia and northern China [*Huang et al.*, 2010]. In spring, the Mongolian Cyclone associated with the East Asian trough often leads to strong northwesterly near surface winds [*Shao and Dong*, 2006] that lift and transport dust particles. East Asian dust can even transport across the Pacific Ocean, reaching as far as the west coast of North America [*Fairlie et al.*, 2010; *Wang et al.*, 2012; *Zhao et al.*, 2010]. Dust particles serve as reaction platforms by depleting O_3, NO_x, SO_2, HNO_3, hydroxyl radicals (OH), and VOC, leading to changes of photochemistry, acid deposition, and production of secondary inorganic aerosol in the atmosphere. East Asian dust is also believed to contribute geochemically significant amounts of minerals that are deposited into the West Pacific Ocean and alter the oceanic primary productivity [*Zhang et al.*, 2003; *Zhuang et al.*, 1992]. Since natural wind-blown dust links the biogeochemical cycle of land, atmosphere, and ocean, understanding the characteristics of dust is essential for further investigating its impact in the Earth's system. Numerical modeling is one of the most important approaches to systematically investigate mineral dust. Global models represent the emission, transport, and deposition of dust in a coherent manner. Huneeus et al. [2011] conducted inter-comparison of 15 global models and reported their simulated AOD and Angström Exponent (AE) within a factor of two and the total

deposition and surface concentration within a factor of 10 with respect to observations. Regional models usually represent dust by following the similar approach as global models. For example, the WRF-Chem [*Grell et al.*, 2005] has been coupled with the GOCART dust scheme [*Ginoux et al.*, 2001]; and the STEM [*Carmichael et al.*, 2003] uses the COAMPS dust scheme [*Liu and Westphal*, 2001]. As compared with global models, regional models usually have finer spatiotemporal resolution and multiple physical parameterizations at the cost of intensive computation. So regional models shall provide more realistic representations of the surface roughness, soil moisture and contents, and also allow comparable validation against surface observations [*Darmenova and Sokolik*, 2008]. The wind-blown dust scheme has been incorporated into the CMAQ model by U.S. EPA [*Appel et al.*, 2013]. Chapter 2 describes the modifications incorporated into the CMAQ model in this study. The objective of this chapter is to evaluate and improve the model's capability of reproducing dust emission, and also enable the model to treat the dust heterogeneous chemistry. This chapter summarizes the improved model performance based on evaluation against observations, and also discusses the remaining uncertainties in the modeling system.

4.4 Results and discussion

4.4.1 **Impact of applying revised friction velocity threshold**

To examine model improvement by implementing new friction velocity threshold constants, simulation from the default dust scheme (Dust_Default scenario) and simulation from the revised dust scheme (Dust_Revised scenario) are compared with the API observations as shown in Figures 4.1. Simulation with the default dust scheme fails to reproduce the dust emission. Dust is generated only over the Gobi Desert for less than $70\,\mu g/m^3$, which can hardly represent the spring dust storm over East Asia. Simulation with the revised dust scheme produces sufficient PM_{10} concentrations by more than $400\,\mu g/m^3$ at the Gobi Desert. Dust plumes are generated by the revised model from the Gobi and Taklamakan Desert, and also from sparse grassland over the northwest region of the Tibetan Plateau. Dust contributes $50\,\mu g/m^3$~$100\,\mu g/m^3$ to PM_{10} over north and east

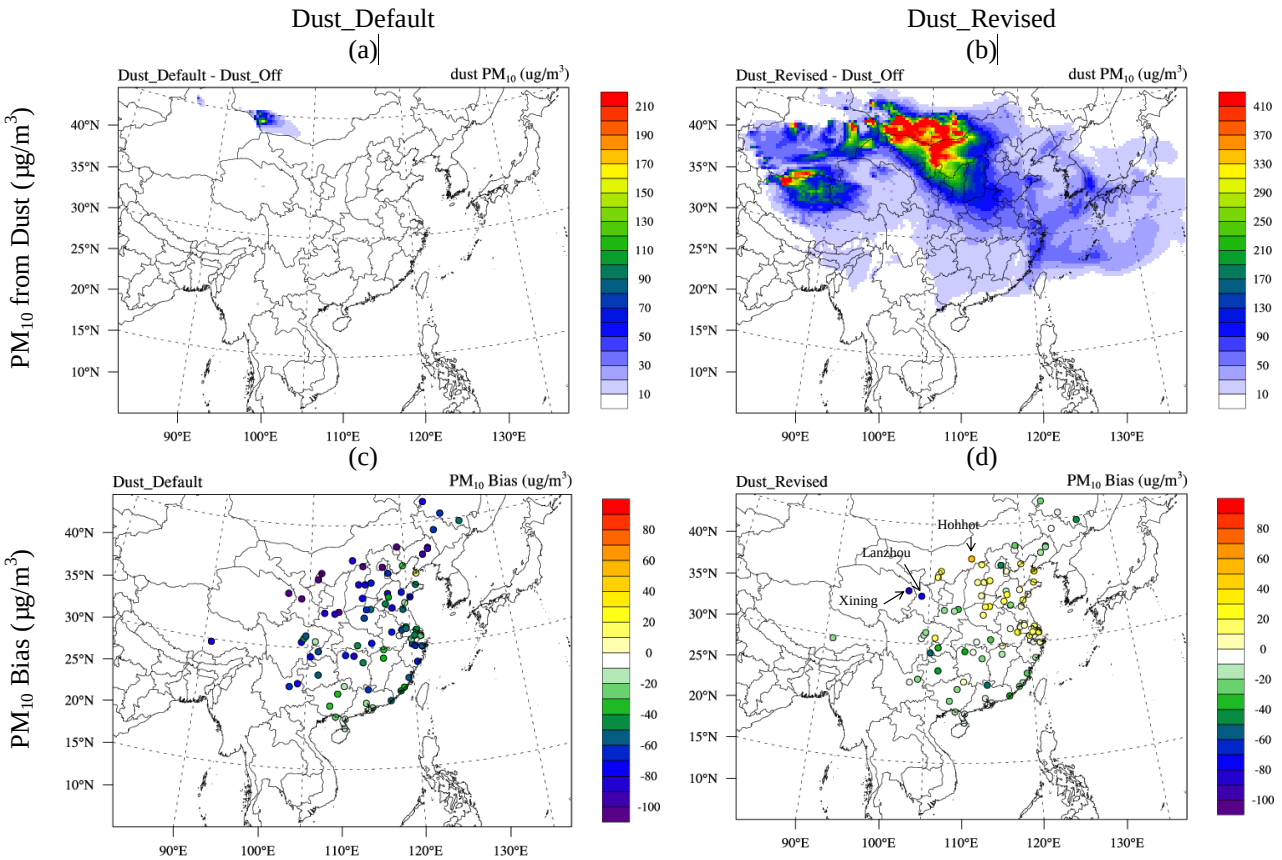

Figure 4.1 Dust concentration simulated under (a) Dust_Default scenario; and (b) Dust_Revised scenario; Simulation bias at the API observational stations for (c) Dust_Default; and (d) Dust_Revised scenario

part of China, and less than 50 $\mu g/m^3$ over south part of China, South Korea, and Japan. Huang et al. [2010] demonstrated that there are two transport pathways for East Asian dust. Dust emission from the Gobi and Taklamakan Desert is either carried by prevailing winds towards South Korea and Japan or towards south part of China and Taiwan. The CMAQ model with revised dust scheme generally reproduces the spatial distribution of Asian dust in spring. Simulation bias of total PM_{10} is reduced from $\pm 80\,\mu g/m^3$ with the default dust scheme to $\pm 30\,\mu g/m^3$ with the revised dust scheme at most of the API stations.

Figures 4.2 shows the evaluation statistics of simulated PM_{10} and AOD as compared with the API and AERONET observations. Simulation bias of PM_{10} without dust emission is -57.52%. With the default dust scheme, domain-wide PM_{10} concentration is underestimated by -55.42%. The default dust scheme is unable to generate sufficient wind-blown dust particles to meet with the observed PM_{10} concentrations. However, the simulation bias of PM_{10} with the revised dust scheme is reduced to -16.06%, suggesting significantly improve model performance for estimating coarse particles. Evaluation for AOD also shows consistent improvement of model performance. As compared to the AERONET measurements, the simulation bias is reduced from -31.19% for CMAQ with default dust scheme to 22.1% for CMAQ with the revised dust scheme. Evaluation of AOD suggests that the revised dust scheme also enables the CMAQ model to better estimate fine mode dust particles.

4.4.2 **Impact of applying source-dependent speciation profile**

Speciation of dust particles determines the mass contributions of trace metal. As described in Chapter 2, the default speciation profile assigns fixed mass contributions of aerosol subspecies for dust emission generated from different areas. This study developed the source-dependent speciation profile for the Gobi and Taklamakan Desert. This section evaluates the improvement of CMAQ model performance for predicting trace metals. Simulations are compared with ground-based observations collected at Duolun and Yulin for K^+, Mg_2^+, and Ca_2^+ as shown in Figure 4.3. It is important to notice that simulations and observations of K^+ and Mg_2^+ are upscaled by 5 and 10 times respectively, to make them comparable with Ca_2^+. Evaluation statistics are summarized in Table 4.1. Duolun

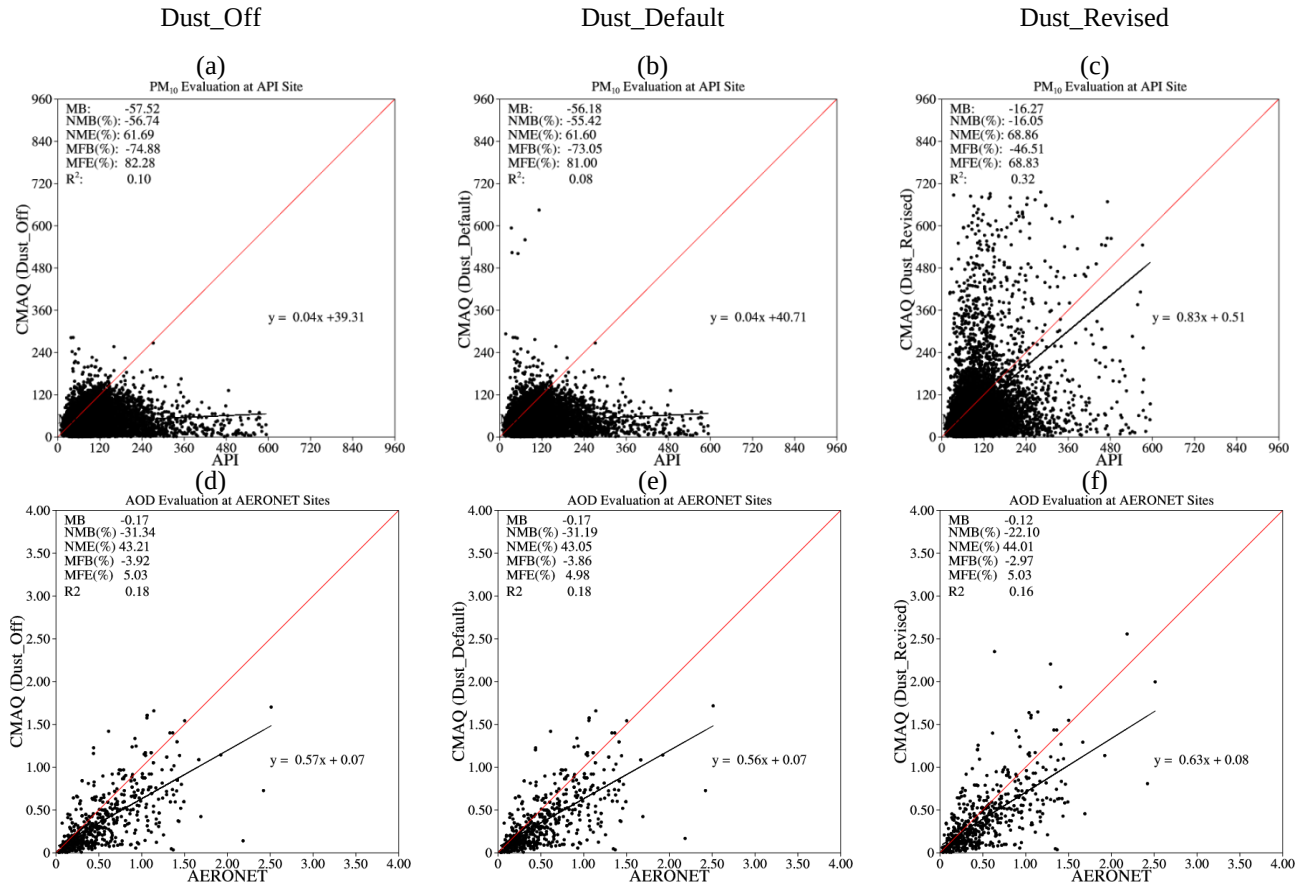

Figure 4.2 CMAQ evaluation against PM_{10} observation from API and AOD observation from AERONET for Dust_Off, Dust_Default, and Dust_Revised scenarios.

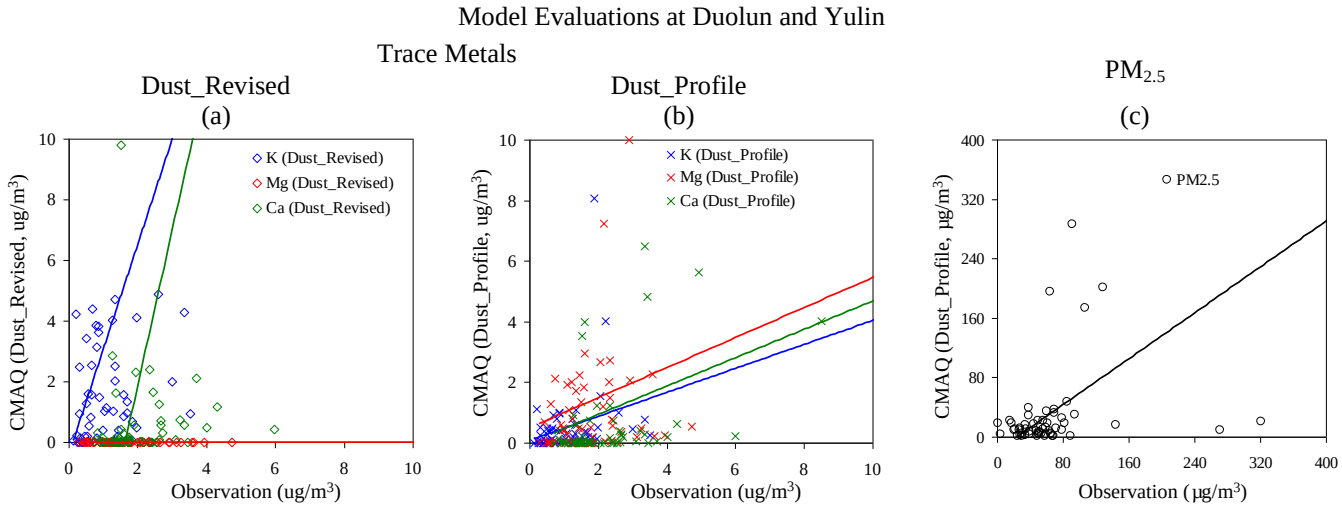

Figure 4.3 CMAQ evaluation for trace metals at Duolun and Yulin for (a) Dust_Revised, and (b) Dust_Profile scenario; and (c) Evaluation of CMAQ simulated (c) $PM_{2.5}$ at Duolun and Yulin.

Table 4.1 Evaluation statistics for tracer metals and $PM_{2.5}$

Variable	$PM_{2.5}$	K^+		Mg_2^+		Ca_2^+	
		Revised*	Profile#	Revised	Profile	Revised	Profile
Mean Obs (μg/m^3)	81.52	0.23	0.23	0.19	0.19	2.24	2.24
Mean Sim (μg/m^3)	44.36	0.69	0.12	0.02	0.12	3.06	1.05
MB (μg/m^3)	-37.17	0.46	-0.11	-0.17	-0.07	0.82	-1.19
NMB (%)	-45.59	208.9	-47.83	-99.8	-36.84	36.69	-53.12
R	0.67	0.42	0.44	0.22	0.51	0.22	0.44

*Revised represents the Dust_Revised scenario

#Profile represents the Dust_Profile scenario

and Yulin are close to the Gobi Desert and the observations at these two stations get littlie contamination by anthropogenic emission. Simulation bias for K^+, Ca_2^+, and Mg_2^+ is changed from 208.9%, 36.69%, and -99.8% respectively with the default speciation profile to -47.83%, -53.12%, and -36.84% respectively with the source-dependent speciation profile. Consistent negative bias for trace metals may be associated with the underestimation of total fine particles with the dust emission. The model evaluation for trace metals suggests that the source-dependent speciation profile provides better description of the mass contribution of each aerosol subspecies in the model. Figure 4.3(c) also shows the comparison between observed and simulated $PM_{2.5}$ concentrations at Duolun and Yulin. On one hand, concentration of $PM_{2.5}$ is underestimated by -45.59%, which is pretty consistent with the underestimations for trace metals. On the other hand, mass contribution of $PM_{2.5}$ to the total suspend particles (TSP) is 40% based on the observations at Duolun and Yulin. Unfortunately there is no PM_{10} observation available at the nearby desert stations. But mass contribution of $PM_{2.5}$ to PM_{10} should be even higher than that to TSP. So it is highly possible that fine particle mass contribution configured within the CMAQ model may be underestimated.

4.4.3 **Impact of heterogeneous chemistry**

Dust heterogeneous chemistry involves the uptake of gas-phase species on to the surface of particles and production of secondary inorganic aerosol. This section investigates the impact of dust heterogeneous chemistry on air pollutants. Figure 4.4 shows the contribution of dust heterogeneous chemistry to O_3 (1st row), SO_2 (2nd row), SO_4^{2-} (3rd row), HNO_3 (4th row), NO_x (5th row), and NO_3^- (6th row). Simulations with the lower (Dust_Chem scenario) and upper (Dust_ChemHigh scenario) bounds of uptake coefficients are investigated to evaluate the impact of heterogeneous chemistry with different reaction rate. Spatial distributions of air pollutants shown in Figure 4.4 suggest that the impact of dust chemistry is more pronounced over east China, while the impact over desert areas is very limited. This is because the east part of China has substantial anthropogenic emission that helps to accelerate the heterogeneous chemistry. But the desert areas in the north and west parts of China have much lower background

concentrations of the air pollutants. Dong and Fu [2015a] report that in spring, O_3 concentration is around 30ppbv and NO_2 and SO_2 concentrations are less than 5ppbv over the Gobi Desert. The concentrations over eastern China are 50~60ppbv for O_3 and 10~40ppbv for NO_2 and SO_2. Substantial amount of reactive gases participate in the heterogeneous reactions on the surface of dust particles transported from deserts. So the impact of dust heterogeneous chemistry is more significant over eastern China. Li et al. [2012] also reported that the impact of dust chemistry for O_3, SO_2, and NO_2 is less than 5% over the Gobi but up to 30~40% in eastern China and even higher over the West Pacific. O_3 concentration is reduced by 3~6 ppbv (2%~10%) and 5~11ppbv (4%~20%) with the lower and upper limits of uptake coefficients, respectively. The impact of heterogeneous chemistry on O_3 evaluated in this study agrees well with the findings from other studies. Tang et al. [2004] reported the impact of heterogeneous chemistry on O_3 is 20%, and Li et al. [2012] reported the impact is 5%~20%. Wang et al. [2012] reported surface O_3 is reduced by 3.8ppbv and 7.3ppbv due to the impact of heterogeneous chemistry with lower and upper uptake coefficients, respectively. The SO_2 concentration is reduced by 2ppbv (10%) and 6ppbv (30%) with lower and upper limits of uptake coefficients, respectively. Depletion of SO_2 also leads to the increase of SO_4^{2-} concentration by $3\,\mu g/m^3$ (8%) and more than $5\,\mu g/m^3$ (15%) with lower and upper limits of uptake coefficients, respectively. Estimations of the heterogeneous chemistry impact on SO_2 vary among different studies. Tang et al. [2004] suggested the impact as 55%; Li et al. [2012] suggested the impact as 10%~20%; and Wang et al. [2012] suggested the impact as 5%~8%. Different evaluations should mainly be attributed to the different simulation episodes. Tang et al. [2004] focused on dust storm episode in 2001 with lower baseline pollutants from anthropogenic emission; Li et al. [2012] simulated for dust storm episode in 2010; and Wang et al. [2012] simulated the entirety month of April in 2001. The net effect of dust heterogeneous chemistry decreases HNO_3 concentration by 0.2ppbv~0.8ppbv (8%~30%). Li et al. [2012] reported the impact of heterogeneous chemistry on HNO_3 is 5%~40%, and Tang et al. [2004] the impact is 30%~70%. The NO_x concentration is increased by 0.2ppbv~1ppbv over eastern China and the West Pacific due to impact of heterogeneous chemistry. The elevation of NO_x concentration

should be attributed to the conversion of gas-phase HNO_3 back to NO_x [*Yarwood et al*., 2005]. As a result of excessive SO_4^{2-} produced from dust chemistry, the concentration of NO_3^- is decreased under the Dust_Chem scenario. The thermal-dynamic equilibrium of the $SO_4^{2-} - NH_4^+ - NO_3^-$ system favors the transformation from NH_4NO_3 to $(NH_4)_2SO_4$ over eastern China due to the intensive anthropogenic emission of SO_2 and NO_x. The depleted NO_3^- evaporates back to HNO_3 and favors the production of NO_x, and subsequently leads to the increase of NO_x but decrease of HNO_3 and NO_3^-. Over South Korea and Japan, the concentration of NO_3^- is increased slightly due to the depletion of NO_x through heterogeneous chemical reactions R8 and R10. This result is also consistent with the findings from other studies. Wang et al. [2012] reported the increase of NO_x and decrease of HNO_3 and NO_3^- due to dust chemistry over East Asia; Li et al. [2012] reported that NO_3^- concentration with lower bound of uptake coefficient is $5\,\mu g/m^3$ (30%) lower than the base case simulation, but the NO_3^- concentration with high uptake coefficient is $12\,\mu g/m^3$ (100%) higher than the base case simulation over China. The impact of dust chemistry shown in Figure 4.4 suggests comparable results as other modeling assessments. But the previous studies mentioned above performed evaluation with model simulations only, and few of them have compared the simulation results with observations to verify the impact of dust heterogeneous chemistry. In this section the EANET measurements are used to compare with simulations from the Dust_Profile, Dust_Chem, and Dust_ChemHigh scenarios. Evaluation statistics are summarized in Table 4.2. O_3 is overestimated by 1.26% without dust chemistry, and is underestimated by -1.97% and -4.43% with lower and upper uptake coefficients, respectively. SO_2 is overestimated by all scenarios, but the simulation bias is reduced from 90.7% without dust chemistry to 69.8% and 63.7% with lower and upper uptake coefficients, respectively. Overestimation of HNO_3 is reduced from 109.03% without dust chemistry to 85.17% and 81.24% with lower and upper limits of uptake coefficients, respectively. The positive simulation bias for SO_2 and HNO_3 should be attributed to the overestimated anthropogenic emissions from China [*Dong and Fu*, 2015; *Wang et al.*, 2011]. Simulation bias of NO_x is slightly increased from 35.61% without dust chemistry 37.79% and 38.21% with lower and upper limits of uptake coefficients, respectively.

Figure 4.4 Impact of dust heterogeneous chemistry with lower (left panel) and upper (right panel) bound of uptake coefficient for surface concentration of O_3, SO_2, SO_4^{2-}, HNO_3, NO_x, and NO_3^-. Color contours represent the absolution concentrations change, and dash contour lines with numbers represent the percentages change

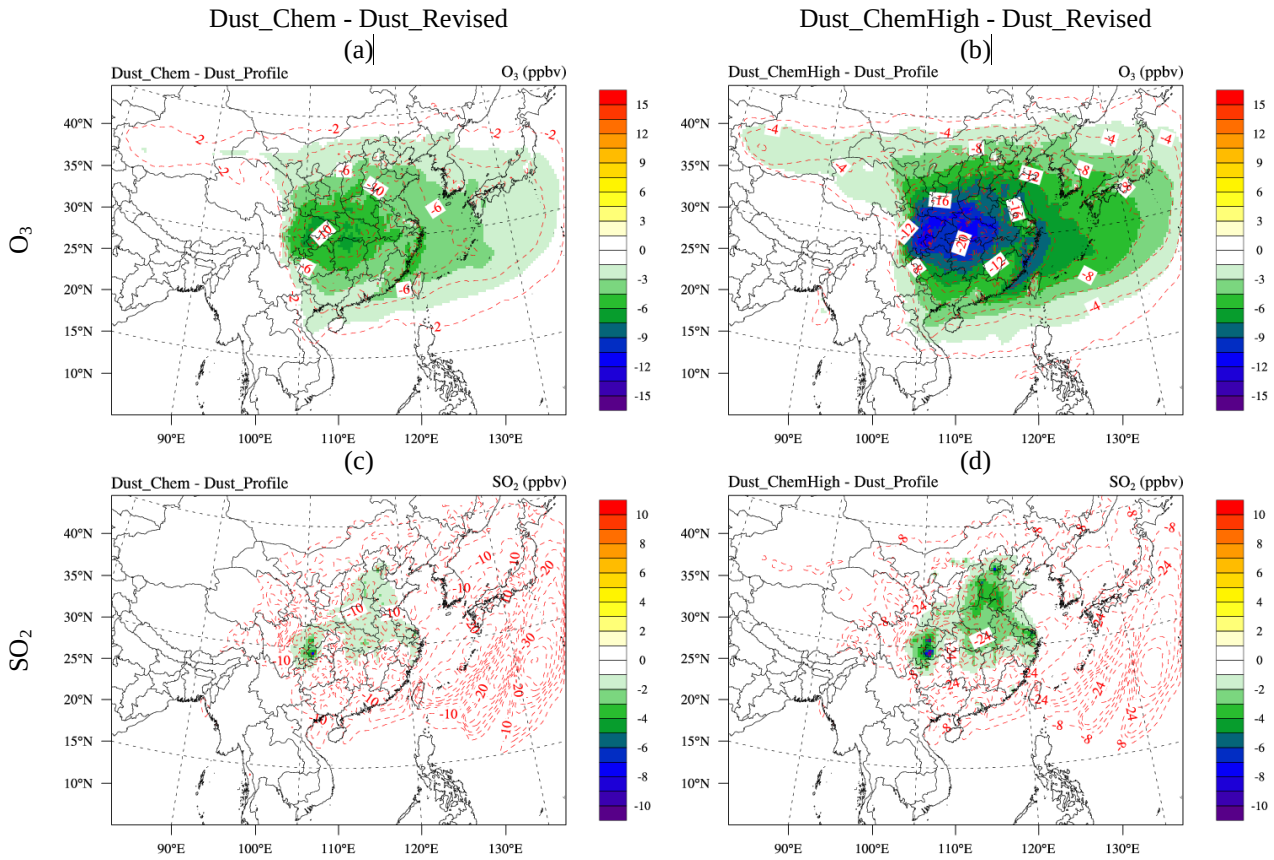

Figure 4.4 Continued

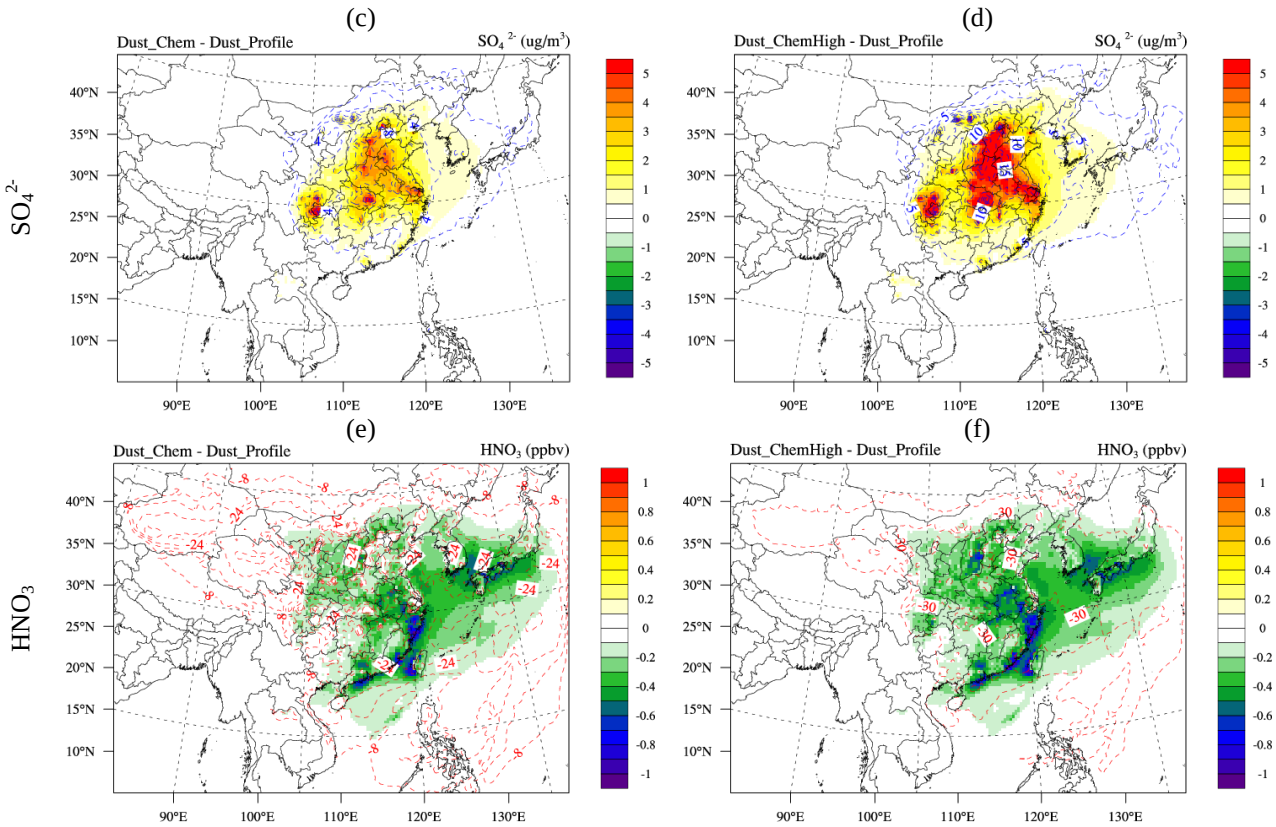

Figure 4.4 Continued

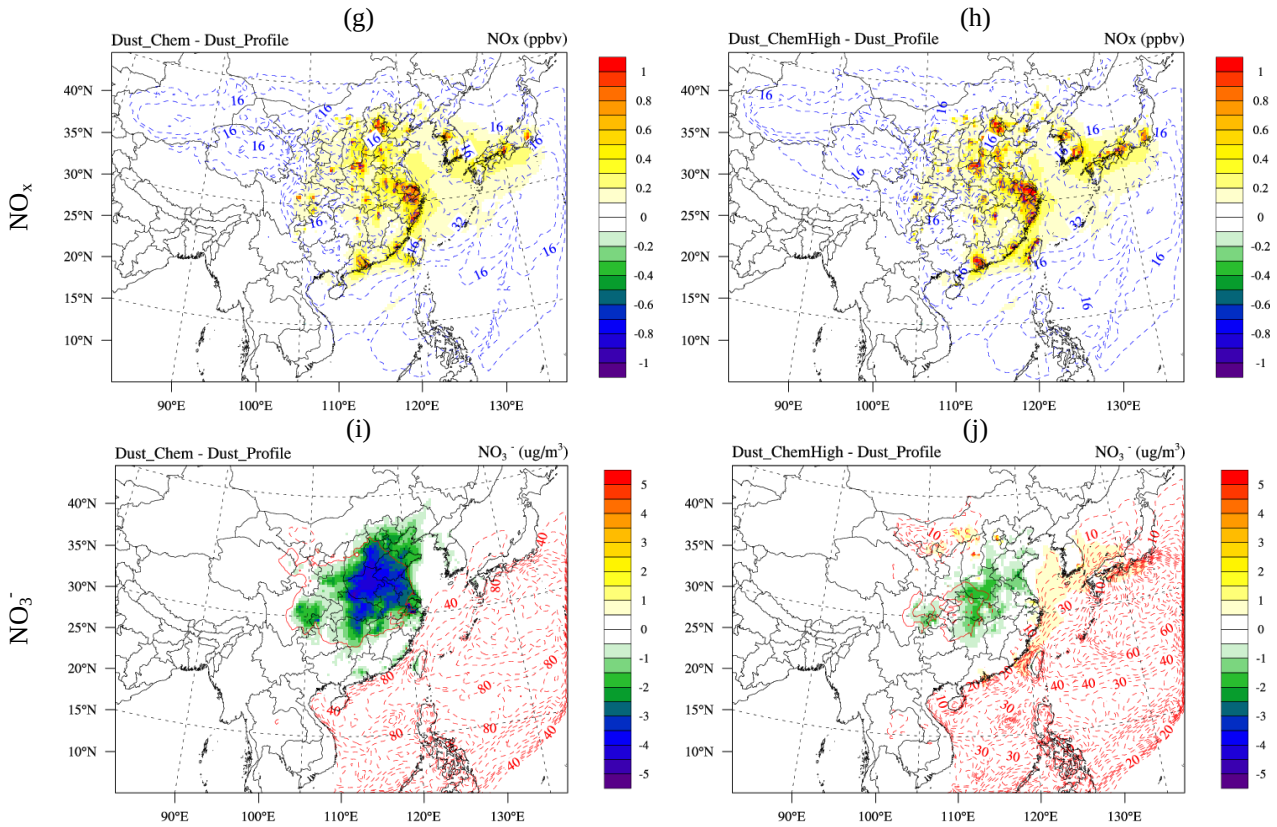

Figure 4.4 Continued

Simulation bias of SO_4^{2-} is moderately increased from -16.28% without dust chemistry, to 13.74% and 29.43% with lower and upper limits of uptake coefficients, respectively. Dust chemistry helps to reduce the slightly underprediction of NO_3^- from 13.07% to -1.97% by Dust_Chem with lower bound of uptake coefficient. But the simulation bias for NO_3^- is boosted up to 24.09% with the upper bound of uptake coefficient. Statistics shown in Table 4.2 suggest that incorporating heterogeneous chemistry in to the CMAQ helps to improve the model performance for most of the species except for O_3 and NO_x. The lower bound of uptake coefficients favors model simulation for SO_4^{2-} and NO_3^-, and the upper bound of uptake coefficients leads to better prediction for SO_4^{2-} and HNO_3. Considering the uncertainty within emission inventory as discussed in Chapter 3, the lower bound of the uptake coefficient may represent the heterogeneous reactions better. Dong and Fu [2015a] reported that that the CMAQ model overestimates NO_x and SO_2 by 30% and 20% respectively, due to the overestimation of anthropogenic emissions. Wang et al. [2011] also reported overestimation of SO_2 by 14% over China. Dust heterogeneous chemistry depletes gas-phase species including SO_2, NO_x, and HNO_3, so it compromises part of the positive bias induced by anthropogenic emission. But heterogeneous chemistry accelerates the production of secondary inorganic aerosol including SO_4^{2-} and NO_3^- . Thus using the upper bound of uptake coefficients produces excessive SO_4^{2-} and NO_3^- and pushes the simulation to overestimate their concentrations as a side effect. But before explicitly excluding the bias within anthropogenic emission inventory, no solid conclusion could be achieved regarding the selection of uptake coefficients.

4.4.4 **Case study of a severe dust storm**

In this section a severe dust storm is investigated to evaluate the model performance. Previous studies have reported that spring 2010 witnessed the most severe dust storms in recent decades [*Bian et al.*, 2011; *Li et al.*, 2012] due to nation-wide drought in China. Observed PM_{10} concentration was more than 1,000 μg/m^3 at Beijing [*Han et al.*, 2012], and 1,600 μg/m^3 at Seoul [*Tatarov et al.*, 2012]. The dust storms also affected Taiwan and increased the local PM_{10} up to 1,200 μg/m^3 [*Tsai et al.*, 2013]. These

Table 4.2 Evaluation statistics for the Dust_Profile, Dust_Chem, and Dust_ChemHigh simulation scenarios

Variable	Scenario	O_3 (ppbv)	SO_2 (ppbv)	SO_4^{2-} ($\mu g/m^3$)	NO_x (ppbv)	HNO_3 (ppbv)	NO_3^- ($\mu g/m^3$)
Mean Obs		45.81	0.59	4.38	1.75	0.43	1.52
MB	Dust_Profile	0.59	0.54	-0.71	0.63	0.46	-0.20
	Dust_Chem	-0.92	0.42	0.60	0.67	0.36	-0.03
	Dust_ChemHigh	-2.07	0.38	1.29	0.68	0.35	0.37
NMB (%)	Dust_Profile	1.26	90.70	-16.28	35.61	109.03	-13.07
	Dust_Chem	-1.97	69.83	13.74	37.79	85.17	-1.97
	Dust_ChemHigh	-4.43	63.70	29.43	38.21	81.24	24.09
R	Dust_Profile	0.63	0.68	0.79	0.69	0.65	0.71
	Dust_Chem	0.62	0.65	0.75	0.69	0.59	0.72
	Dust_ChemHigh	0.59	0.64	0.72	0.69	0.60	0.73

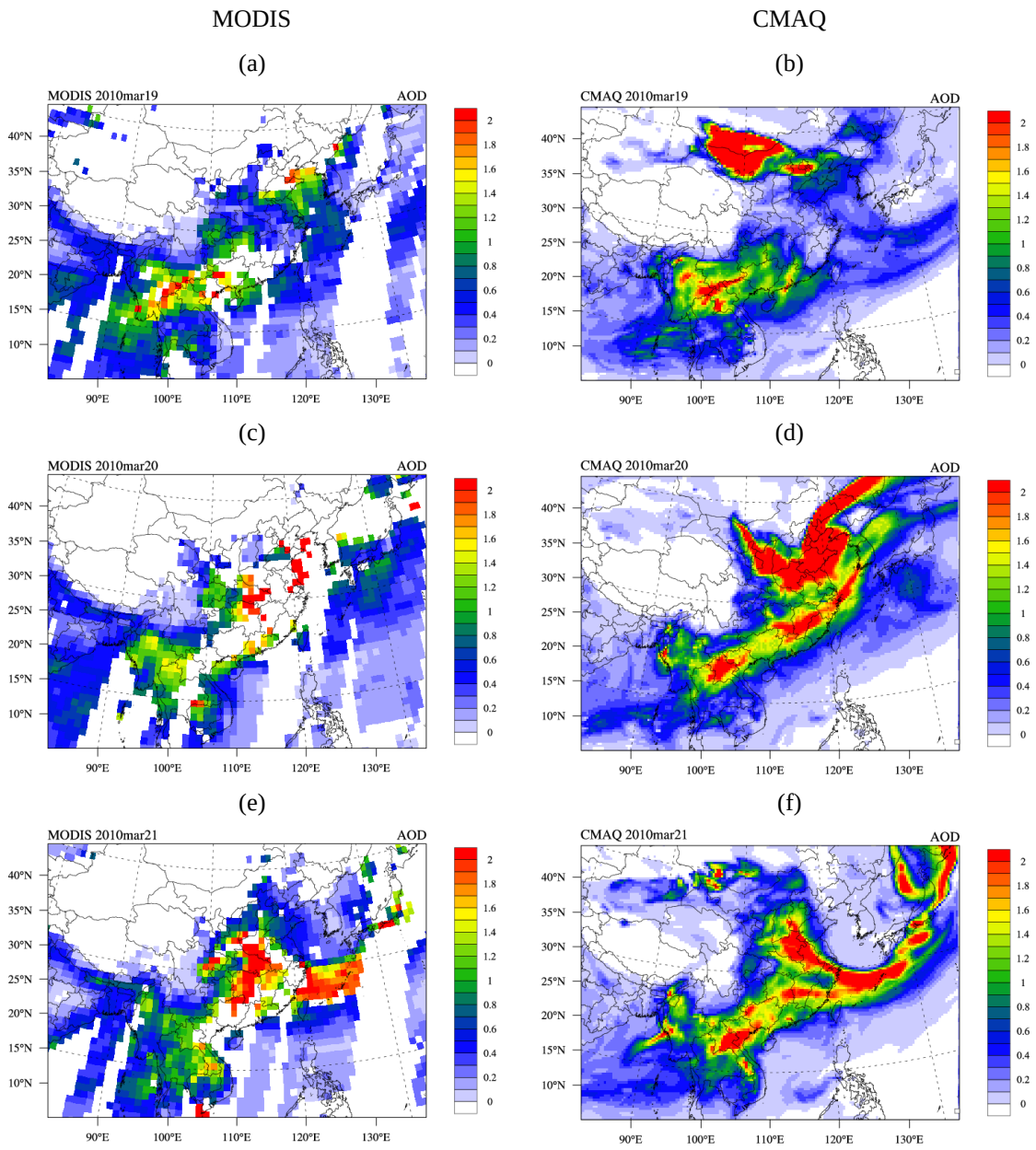

Figure 4.5 Spatial distribution of AOD from the MODIS product and the CMAQ simulation

studies focused on the impact of dust storms on a local scale, and the understanding about the emission and transport of dust storms on a regional scale is not well-developed. Figure 4.5 shows the spatial distributions of AOD from both the CMAQ simulation and the MODIS product during a severe dust storm episode from Mar.19th to Mar.21st in 2010. Spatial distributions of AOD from simulation agree well with the satellite product on a daily scale, indicating that the model successfully reproduces the column density and long-range transport of dust particles. The CMAQ simulation suggests that intensive dust emission is generated from the Gobi Desert on Mar.19th, and gradually transports toward eastern China, the West Pacific, and Taiwan during the following days. Although the MODIS product is contaminated by cloud over the Gobi Desert, observations over eastern China and the West Pacific show consistent dispersion and intensity of AOD with the CMAQ simulation.

The Hybrid Single-Particle Lagrangian Integrated Trajectory (HYSPLIT) model from NOAA/Air Resources Laboratory (Draxler and Rolph, 2015; Rolph 2015) is applid to investigate the trajectory of dust plume, as shown in Figure 4.6(f). Movement of air mass is analyzed for 72 hours starting from 0:00 UTC (8:00 BT) on Mar.19th 2010 at the Gobi Desert. Dust plumes at 500m, 1km, and 2km height move southeastward on March 20th, then the 2km height plume turns east and pass across Japan and the West Pacific. The lower two dust plumes continue move toward southeastern China, and reach down to Taiwan Mar.21st. The HYSPLIT trajectory analysis shows consistent transport pathway with the CMAQ simulation and the MODIS product. This section also compares the daily variations of PM_{10} between model simulation and surface observations at selected locations along the transport pathway. Simulations from the Dust_Chem and Dust_Off scenarios are both investigated to evaluate the improvement of model performance. Daily variations of PM_{10} are compared between the CMAQ simulations and the API observations at Beijing, Lanzhou, Nanjing, Fuzhou, Lianyungang, and Shanghai as shown in Figures 8(a), (b), (c), (d), (e), and (k), respectively. The Dust_Chem scenario successfully reproduces the temporal variations and peak values of PM_{10} as compared with the API observations. At Beijing, PM_{10} concentration increases rapidly from less than 300 $\mu g/m^3$ on Mar.18th to more than 600 $\mu g/m^3$ on Mar.19th. In central and eastern

China, concentrations of PM_{10} increase to more than $600\,\mu g/m^3$ at Nanjing and Shanghai on Mar.20th. In southern China, PM_{10} increases to $500\,\mu g/m^3$ at Xiamen on Mar.22nd. PM_{10} concentrations at these cities are elevated with the onset of the dust storm and fall back under $300\,\mu g/m^3$ right after the event. In western China however, PM_{10} concentration at Lanzhou is $500\,\mu g/m^3$ on Mar.14th, due to the contribution from the Taklamakan Desert [*Ling et al.*, 2011]. The CMAQ simulations are also compared with the AERONET measurements at Japan and the TAQMN measurement at Taiwan. Daily variations of PM_{10} at Xinzhuang, Oki, Ogasawara, and Hedo are shown in Figure 4.6(g), (h), (i), and (j) respectively. PM_{10} concentrations at these sites show consistent increase from Mar.21st to Mar.22nd due to the impact of dust storm. The local PM_{10} concentration at Xinzhuang is increased from less than $100\,\mu g/m^3$ on March 20th to more than $700\,\mu g/m^3$ on Mar.21st. Daily variations of AOD from the CMAQ simulations are compared with the AERONET measurements at four selected stations. These stations area: Beijing, the Semi-Arid Climate Observatory Laboratory (SACOL) station at Lanzhou [Ling et al., 2011], Osaka, and the EPA-NCU station at Taiwan. These stations are selected to represent the impact of dust storm on AOD at different sub-areas within the study domain. Daily variations of AOD show consistent temporal changes as PM_{10}. The local AOD is increased from Mar.19th to Mar.21st at the Beijing, Osaka, and EPA-NCU stations. The SACOL station reaches highest AOD on Mar.14th, which is also consistent with the temporal variation of PM_{10} concentration at Lanzhou. Moderate underestimations of AOD are identified at all the four stations during the dust storm episode. In general, the CMAQ model tends to slightly overestimate dust at nearby desert locations but underestimate dust at southeastern China and the West Pacific. The comparison of daily variations of PM_{10} and AOD between simulations and observations suggests that the revised CMAQ model successful reproduces the emission and transport of the severe dust storm.

4.4.5 **Remaining uncertainty within the modeling system**

Although the previous sections have demonstrated the improved CMAQ model performance by incorporating the modifications made in this study, it is necessary

Figure 4.6 Forward trajectories from (f) HYSPLIT; Comparison of daily average PM_{10} between observation and CMAQ simulations at (a) Beijing; (b) Lanzhou; (c) Nanjing; (d) Xiamen; (e) Lianyungang; (k) Shanghai; (g) Xinzhuang; (h) Oki; (i) Ogasawa; and (j) Hedo; Comparison of daily average AOD between simulations and the AERONET observations at (l) Beijing; (m) SACOL; (n) Osaka; and (o) NCU

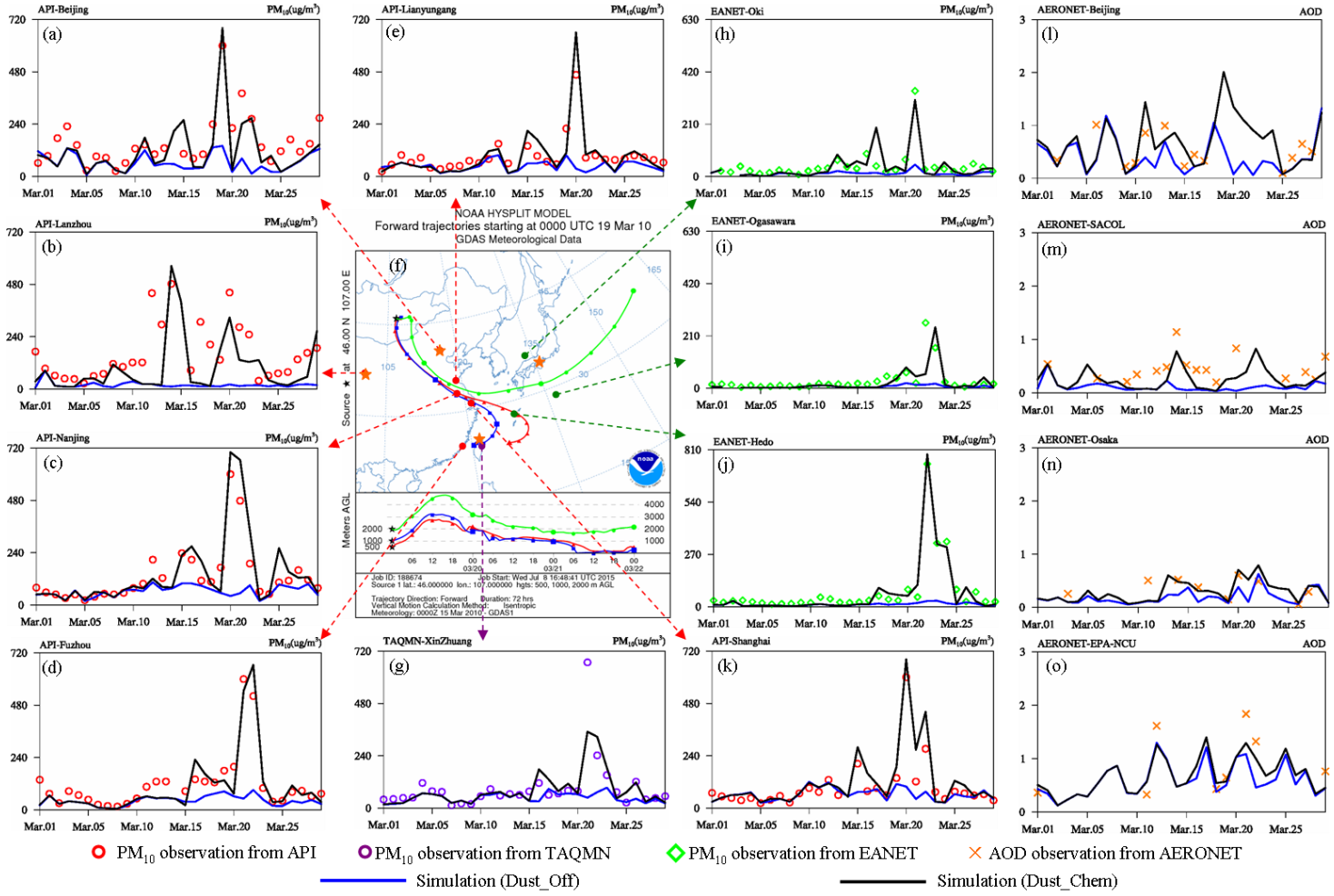

Figure 4.6 Continued

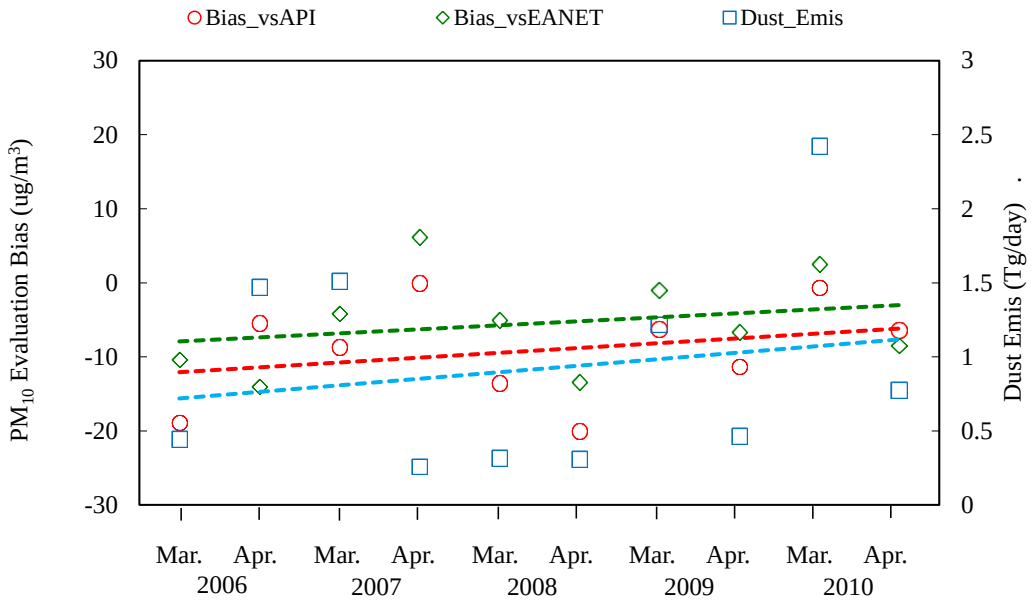

Figure 4.7 Temporal changes of the dust emission rate (solid orange rectangles), and the simulation bias of PM_{10} against observations from API (red cycles) and EANET (green diamonds). Dash lines represent the trends of the variables.

to note that there are some important remaining uncertainties within the modeling system. The first type of uncertainty is related to the anthropogenic emission. Evaluation of the CMAQ model performance in terms of simulating dust is performed by comparing simulations with observations. But the uncertainty within anthropogenic emission inventory may induce unexpected simulation bias into the modeling system. And it is difficult to distinguish bias induced by emission inventory rom the bias induced by the wind-blown dust scheme. Figure 4.7 shows the dust emission rate (Tg/day), the simulation bias of PM_{10} at the API stations, and the simulation bias of PM_{10} at EANET stations. Simulation result of CMAQ suggests a slightly increasing trend of East Asian dust emission from 2006 to 2010, which is consistent with the decadal increase of dust reported by Kurosaki et al. [2011] due to changes of soil erodibility over Mongolia and northeastern China. Simulation bias of PM_{10} shows a strong correlation with the increasing trend of dust emission at both the API and EANET stations. The strong correlation indicates that the negative simulation bias of PM_{10} is compromised by the contribution from wind-blown dust. This is also consistent with previous studies [*Wang et al.*, 2011; *Dong and Fu.*, 2015a] that reported the systematic underestimation of anthropogenic emission of primary PM_{10} over China. Improving the quality of anthropogenic emission inventory may help to a more solid baseline to further evaluate the bias from dust scheme in the model.

The second type of uncertainty lies within the threshold friction velocity u_{*_t}. This variable may be overestimated due to the excessive soil moisture fraction simulated by WRF in this study. Although the initial threshold friction velocity constants u_{*_c} is adjusted by removing the double counting of soil moisture effect, there is still non-negligible simulation bias identified in previous sections. Both the five-year average modeling bias shown in Figure 4.1 and the daily variations of PM_{10} shown in Figure 4.6 suggest overestimation of dust at the Gobi Desert and underestimation at the Taklamakan Desert. The averaged u_{*_t} calculated by the CMAQ is 0.19m/s and 0.14m/s over the Taklamakan and Gobi Desert, respectively. The soil moisture factor f_{soilm} is 1.21 and 1.13 over the Taklamakan and Gobi Desert respectively, indicating that the Taklamakan

Desert requires higher friction velocity to generate dust emission because of the wet soil. However, some recent field experimental studies suggested that u_{*_t} in the Taklamakan Desert is lower than that over the Gobi. He et al. [2010] obtained field measurements at three sampling sites inside the Taklamakan Desert and reported the value of u_{*_t} as 0.25m/s, 0.27m/s, and 0.21m/s. Yang et al. [2011] also reported the value of u_{*_t} as 0.24m/s at Tazhong inside the Taklamkan Desert. Li and Zhang [2011] reported the value of u_{*_t} as 0.34m/s ~0.42m/s at the Gobi Desert. Field measurement defines u_{*_t} as it equals to the value of friction velocity u_* when dust concentration is increased by 20% for at least one-half hour [*Li and Zhang*, 2011]. So the u_{*_t} values reported by these measurement studies are higher than the calculations from the CMAQ model. But the comparison of field measurements between the Taklamakan and the Gobi Desert suggests that the CMAQ model may either underestimate u_{*_t} at the Gobi Desert, or overestimate u_{*_t} at the Taklamakan Desert. Since f_{soilm} is determined by soil moisture fraction, this study also compares the soil moisture from FNL data with another reanalysis dataset Global Land Data Assimilation System (GLDAS; [*Rodell et al.*, 2004]). Figure 4.8 shows the spatial distributions of soil moisture fraction at top 10cm depth from FNL and GLDAS. Soil moisture fraction is estimated to be 10~15% by FNL at the Taklamakan and Gobi Deserts, while the estimation by GLDAS is less than 5% at these deserts. Zender et al. [2003] reported that soil moisture from FNL is too high over active dust emission areas and leads to negative AOD simulation bias on a global scale. Haustein et al. [2012] conducted simulation with meteorology driven by FNL and GLDAS respectively over north Africa, and reported that the prediction with GLDAS had better agreement with the AERONET measurements. Sensitivity study about the soil moisture fraction impact on meteorology model prediction has not been performed over East Asia, and unfortunately there is no publicly available measurement of soil moisture at the deserts. So research effort is required to evaluate the uncertainty caused by using FNL soil moisture data.

The last type of uncertainty lies within the mass contribution of fine mode aerosol within dust emission. Dust emission is divided into fine and coarse mode aerosol with mass contribution of 20% and 80%, respectively. In this study however, the mass contribution of $PM_{2.5}$ to TSP is about 40% based on the observations at the nearby Gobi stations. The data from Huang et al. [2010] suggests that mass contribution of $PM_{2.5}$ to TSP is 45% at an inside Taklamakan station. Model evaluation results shown in Figure 5 also demonstrate the systematic underestimations of both trace metals and total $PM_{2.5}$ concentrations at both dust source regions and downwind areas, while the concentrations of PM_{10} are slightly overestimated near the source region as demonstrated in Figure 4.3. Consequently, it is highly possible that the ratio of fine particles within dust emission should be higher than 20%. Observations of both $PM_{2.5}$ and PM_{10} at active dust regions are urgently needed to help clearly characterize their mass contributions in the model.

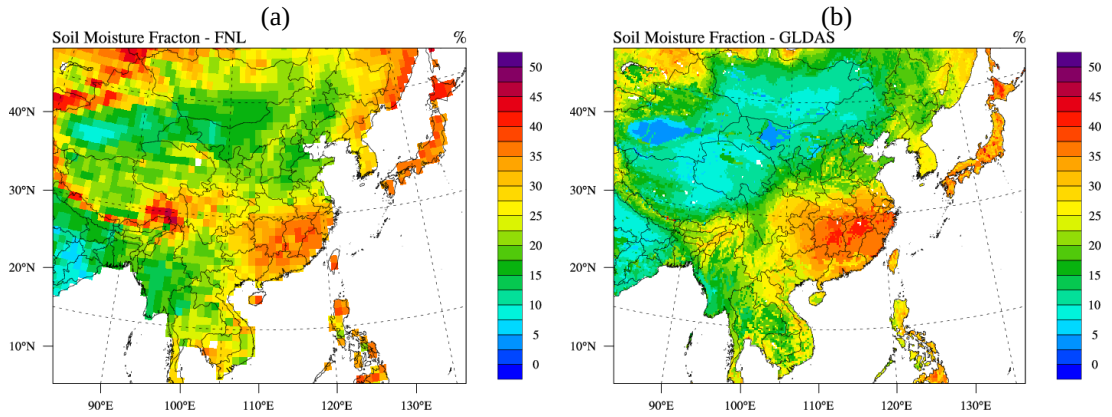

Figure 4.8 Spatial distribution of soil moisture fraction in the top 10cm soil depth from (a) FNL; and (b) GLDAS

5 IMPACT OF BIOMASS BURNING AND DUST ON REGIONAL CLIMATE

5.1 Declaration

This chapter is slightly revised based on a manuscript in preparation for journal publication.

5.2 Abstract

In this chapter the performance of two-way mode WRF/CMAQ modeling system is evaluated for the first time over East Asia. Then aerosol induced changes in shortwave radiation (SWR) and air temperature profile are investigated to estimate the impact of biomass burning and dust on regional climate. Direct radiative effect (DRE) of biomass burning aerosol is usually considered as slightly negative at top of the atmosphere (TOA), which indicates a warming enforcement on the atmosphere. Although the IPCC Fourth Assessment Report (AR4) suggests that the overall radiative forcing (RF) of biomass burning aerosol is strongly positive above the cloud, previous modeling studies only estimate the DRE of biomass burning aerosol under clear sky condition. This study evaluates the DRE of biomass burning aerosol over East Asia under both clear and all sky conditions. This study reveals that biomass burning reduces the downward SWR flux by 20W/m^2 (10%) at ground surface (SFC) over PSEA and south China. Biomass burning also has significant warming effect as it reduces the upwelling SWR flux by 10W/m^2 (<10%) at TOA under all sky condition. The biomass burning induced change of upwelling SWR at TOA is significantly higher under all sky condition due to the presence of the persistent stratocumulus cloud layer over PSEA. The distinct biomass burning DRE under clear and all sky conditions suggests that the impact of biomass burning needs to be carefully investigated. This study reveals that dust has a moderately cooling effect over China and the West Pacific as it increases the upwelling SWR flux by 3/m^2~10W/m^2 (4%~16%). Dust also has a slightly warming effect over southeast part of Tibet Plateau where the land surface is covered by snow. Both biomass burning and dust cool the near surface air and warm the upper air. The aerosol induced changes of air

temperature is heavily dependent on the vertical distribution of aerosol. Biomass burning alters air temperature by -0.3K at 0~0.5km height and +0.25K at 1 km ~3km height over PSEA and south China. Dust alters air temperature by -0.7K at 0~1km height and +0.1K at 5 km ~7km height over central China and the West Pacific. Coexistence of biomass burning and dust in upper air at Taiwan is found insignificant, as only two mixing cases are identified during the study period. But the simulation reveals that the coexistence alter the aerosol direct radiative effect efficiency ($E\tau$) of both dust and biomass burning by ±10%. This study is the first evaluation of the impact of biomass burning and dust on regional climate with the WRF/CMAQ modeling system. The result of this study provides a baseline estimation of the aerosol feedback on radiative forcing budget over East Asia.

5.3 Introduction

The impact of biomass burning aerosol on direct radiative forcing effect (DRE) is an open-ended question. The IPCC estimates the radiative forcing (RF) of biomass burning aerosol as -0.2W/m^2 in the Third Assessment Report (TAR), $+0.03 \pm 0.12$W/m^2 in the Fourth Assessment Report (AR4), and 0(-0.2~+0.2)W/m^2 in the Fifth Assessment Report (AR5). The difficulties for evaluating the contribution from biomass burning include accurately estimating the emission inventory, optical properties, and vertical distribution. Biomass burning plume contains multiple aerosol species with various optical properties. It contains both strong absorbing aerosol such BC and cooling aerosol such as sulfate. Field measurements indicate that for different types of burning activities, the mass contributions can vary within a factor of 2 for BC and a factor of 10 for inorganic aerosol [*Akagi et al.,* 2011]. Evaluating the overall DRE of biomass burning aerosol requires an accurate estimation of the mass contributions from different aerosol subspecies, which is difficult since biomass burning is essentially uncontrolled. Biomass burning emission inventories contain larger discrepancy than anthropogenic emission inventories [*Kasischke and Penner*, 2004]. The plume rise of biomass burning is usually limited within PBL by models [*Reid et al.*, 2009], but satellite products suggest that the biomass burning plume is frequently lifted into free troposphere above the cloud [*Hsu et al.*, 2003].

Some pilot studies have been conducted to investigate the impact of biomass burning on regional climate. The most recent AeroCom II experiment reviewed and summarized the modeling studies from 16 global models and reported that the contribution of biomass burning to DRE falls in the range from -0.8W/m^2 to +0.7W/m^2 [*Myer et al.,* 2013]. Based on airborne aerosol and cloud measurements over southern Africa, Keil and Haywood [2003] reported that the upwelling TOA forcing is converted from -13.0W/m^2 under clear sky condition to +11.5W/m^2 with the presence of underlying cloud. Jacobson M.Z. [2014] reported that biomass burning may cause a net global warming of 0.4K because of the cloud absorption effect. Zhang et al. [2009] investigated the impact of biomass burning on monsoon circulation over Amazonia and reported that the warming of lower troposphere by smoke aerosol may re-enforce winter-like synoptic cyclonic activities and rainfall in South America. Although these studies provide estimations of the biomass burning contribution to DRE, critical uncertainties remain in the measurement or modeling methods. In addition, most of the previous regional studies focused on South America [*Kaufman and Koren*, 2006; *Koren et al.,* 2008] and Africa [*Keil and Haywood,* 2003; *Haywood et al.,* 2004; *Wilcox et al.,* 2012]. The understanding of biomass burning impact over East Asia is poorly developed due to limited research efforts.

Knowledge of the dust impact on climate is not well developed either. Estimations are mainly made for anthropogenic dust because its RF efficiency is assumed as equal to natural dust. The TAR reported that the DRE of anthropogenic dust lies in the range from -0.6W/m^2 to +0.4W/m^2. The AR4 reported that the net DRE of dust falls in the range from -0.3W/m^2 to +0.1W/m^2 [*Forster et al.*, 2006], but also indicated that dust may exert extremely strong instantaneous shortwave DRE by up to -130W/m^2~-45W/m^2 over coastline of West Africa [*Haywood et al.*, 2003; *Hsu et al.*, 2000]. The AR5 reported the DRE of dust is -0.14±0.11W/m^2. Although these estimations about the DRE of dust are consistent among IPCC reports, no solid conclusion is achieved regarding the inquiry that whether dust is cooling or warming the atmosphere. Huneeus et al [2011] compared 15 global models and reported that the surface concentration of dust is reproduced within a factor of 10 and AOD is estimated within a factor of 2, due to the variations of the microphysical schemes in the models. Zhao et al. [2012] conducted model simulation

over Southwestern U.S. and reported that the lower atmosphere over the deserts is heated by suspended dust and subsequently strengthen the low-level southerly moisture fluxes. The impact of natural dust on DRE over East Asia has also been investigated by recent studies. Uno et al. [2006] compared applications of eight models over Asia and reported the surface level dust concentration is simulated within a factor of 4, and vertical profiles of dust is reproduced within a factor of 2. Chen et al. [2014] reported that the DRE of dust over East Asia is -14W/m^2~-10W/m^2at SFC and -8W/m^2~-5W/m^2 at TOA.

The abovementioned studies indicate an urgent research need to estimate the DRE of biomass burning and dust over East Asia. In this study, the two-way mode WRF/CMAQ modeling system is applied to evaluate the DRE of biomass burning and dust with and without the presence of cloud. This study also probes into the regional climate effect of biomass burning and dust in terms of altering the air temperature profiles. In addition, East Asia suffers from both biomass burning and dust in spring, but no investigation has been initiated to evaluate the overall radiative forcing effect with the coexistence of biomass burning and dust. Johnson et al. [2008] reported that there is frequently considerable mixing of biomass burning and mineral dust over West Africa, and the presence of mineral dust enhances the biomass burning aerosol absorption of solar radiation by approximately 10%. So in this study, the coexistence of biomass burning and natural dust is also investigated to reveal the net effect on the regional climate of East Asia.

5.4 Results and discussion

5.4.1 **Evaluation of the two-way mode WRF/CMAQ system**

Before probing into the impact of aerosol on regional climate, the two-way mode WRF/CMAQ modeling system is compared with the CERES and MODIS products to evaluate the model performance.

Figure 5.1 shows the spatial distributions of upward SWR at TOA and downward SWR at SFC from the CERES product and the WRF/CMAQ simulation. The evaluation statistics are summarized in Table 5.1. The modeling system successfully

reproduces the spatial distributions and intensities of SWR flux at both TOA and SFC, with noticeable discrepancies are found over the Himalayas and the Tibet Plateau.

The WRF/CMAQ system overestimates the upward SWR flux at TOA under clear sky condition by 14.8%. Simulation bias is larger over land areas with high surface albedo, such as the Taklamakan Desert and the barren and grass land over Mongolia. Overestimation of SWR flux at TOA is associated with the fixed albedo for snow and ice (0.8) used in the model [*Porter et al.*, 2011]. Simulated bias of SWR flux at TOA is -3.98%, indicating a good model performance of the WRF/CMAQ system. Evaluation for downward SWR flux at SFC suggests consistent agreement between simulation and satellite observation. The simulation bias for SWR flux at SFC is -0.61% under clear sky condition and 7.87% under all sky condition. Large negative bias is found over Tibet Plateau under clear sky condition, due to the discrepancy of predicting cloud cover over this region.

Evaluation statistics calculated in this study are consistent with the findings from other studies. IPCC compared the CMIP5 models with the CERES product and reported ±10 W/m^2 modeling bias over the continental U.S. (CONUS) domain. Wu et al. [2015] reported correlation between WRF and CERES as ≥0.87 over the Central and West Pacific domain. Yu et al. [2014] reported about ±30% difference between the WRF simulation and the CERES product for shortwave cloud forcing over CONUS. Wu et al. [2012] reported ±10% difference between the WRF simulation and the CERES product over the inner tropics. Kato et al. [2013] compared the CERES product with surface observations and reported that uncertainty in CERES SWR lies in the range of -1.7~4.7 W/m^2. So in summary, the WRF/CMAQ modeling system reasonably reproduces the radiation flux over East Asia.

The MODIS product is used in this section to evaluate the model performance in terms of reproducing the vertical profiles of meteorological variables. Figure 5.2 shows the spatial distributions of air temperature (T) and relative humidity (RH) at 1000hPa, 950hPa, 920hPa, 850hPa, 780hPa, 700hPa, 620hPa and 500hPa from the MODIS product and the WRF/CMAQ simulation. Evaluation statistics are summarized in Table 5.2. Simulations and satellite observations are in close agreement with each other at all

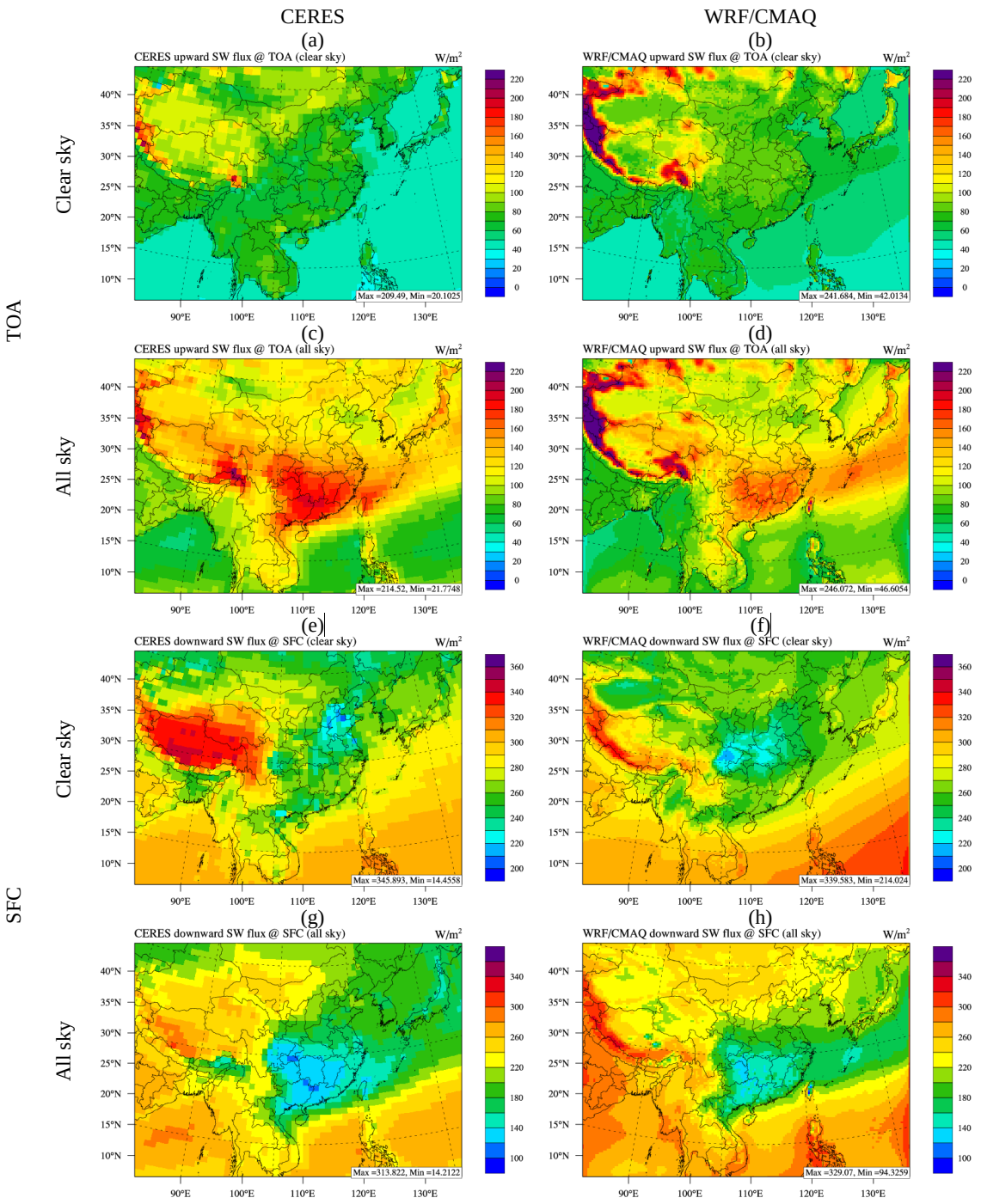

Figure 5.1 Comparison of SWR between the CERES product (left panel) and the WRF/CMAQ simulation (right panel) for upwelling flux at TOA and downward flux at SFC

Table 5.1 Evaluation Statistics for SWR flux

Variable	Condition	Mean Obs(W/m^2)	Mean Sim(W/m^2)	MB (W/m^2)	NMB (%)	Corr.
TOA	Clear sky	66.14	75.90	9.79	14.80	0.91
	All sky	113.98	109.45	-4.53	-3.98	0.89
SFC	Clear sky	282.03	280.29	-1.73	-0.61	0.86
	All sky	221.55	238.98	17.43	7.87	0.93

Figure 5.2 Comparision of air temperature at 1,000hPa, 950hPa, 920hPa, 850hPa, 780hPa, 700hPa, 620hPa, and 500hPa between the MODIS product (left panel) and the WRF/CMAQ simulation (right panel)

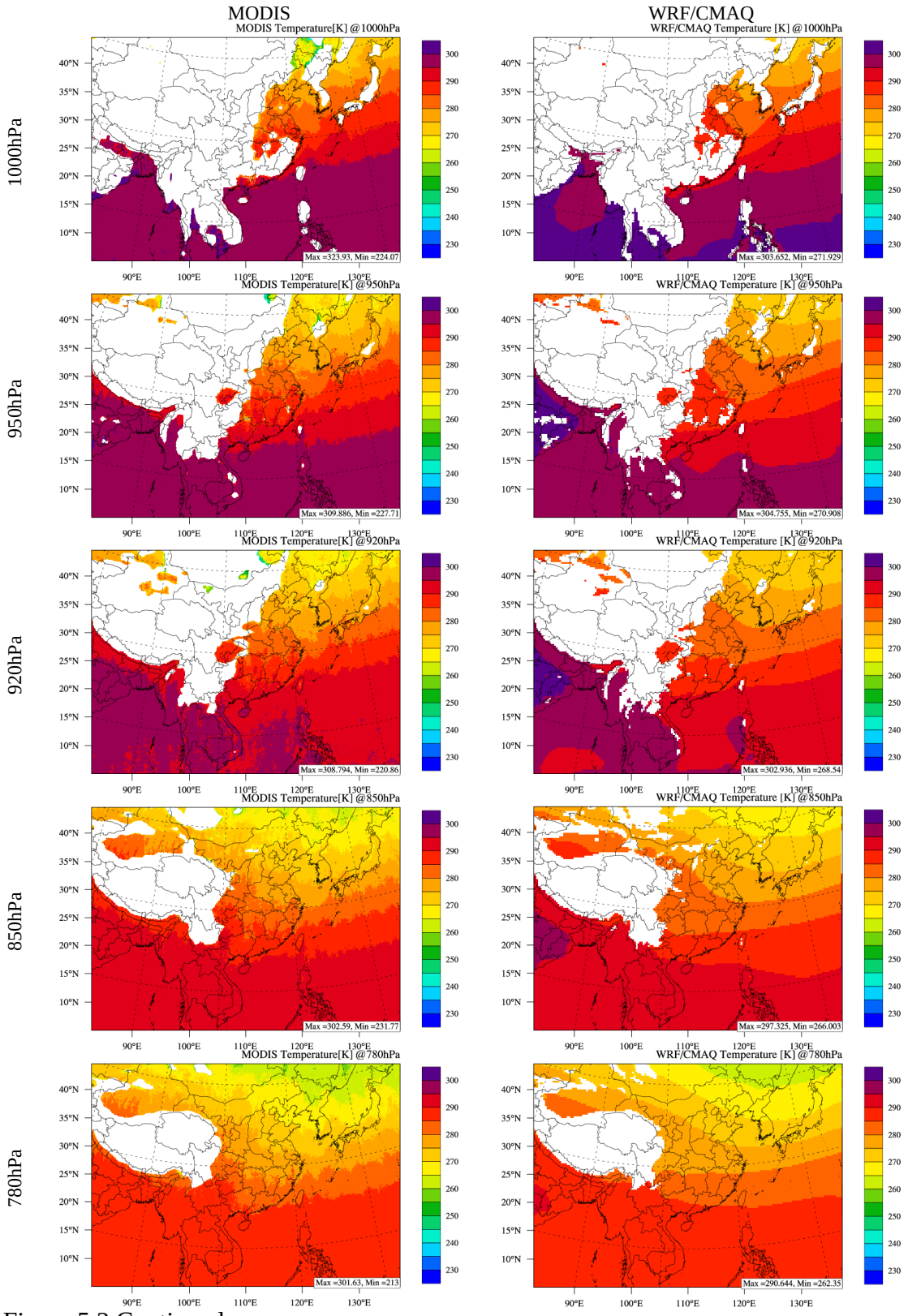

Figure 5.2 Continued

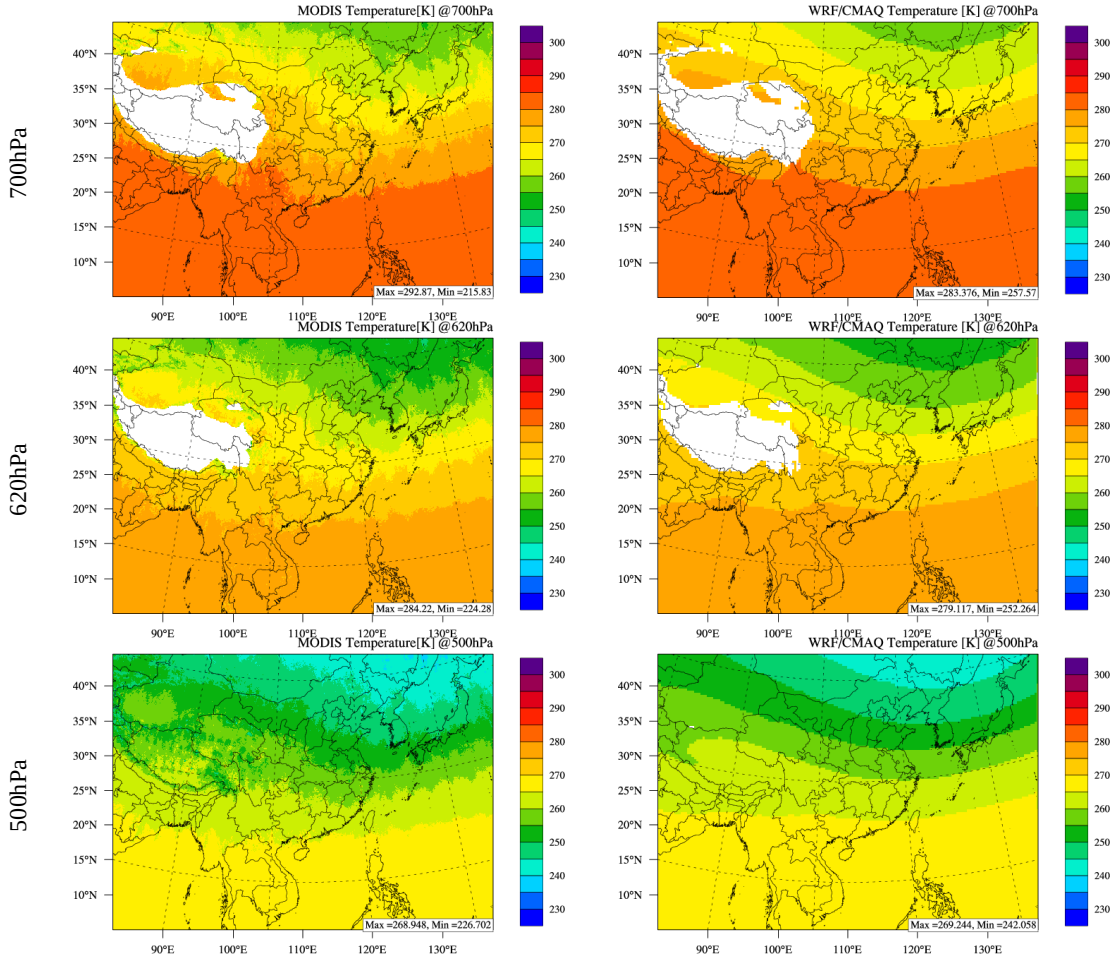

Figure 5.2 Continued

Figure 5.3 Comparision of relative humidity at 1,000hPa, 950hPa, 920hPa, 850hPa, 780hPa, 700hPa, 620hPa, and 500hPa between the MODIS product (left panel) and the WRF/CMAQ simulation (right panel)

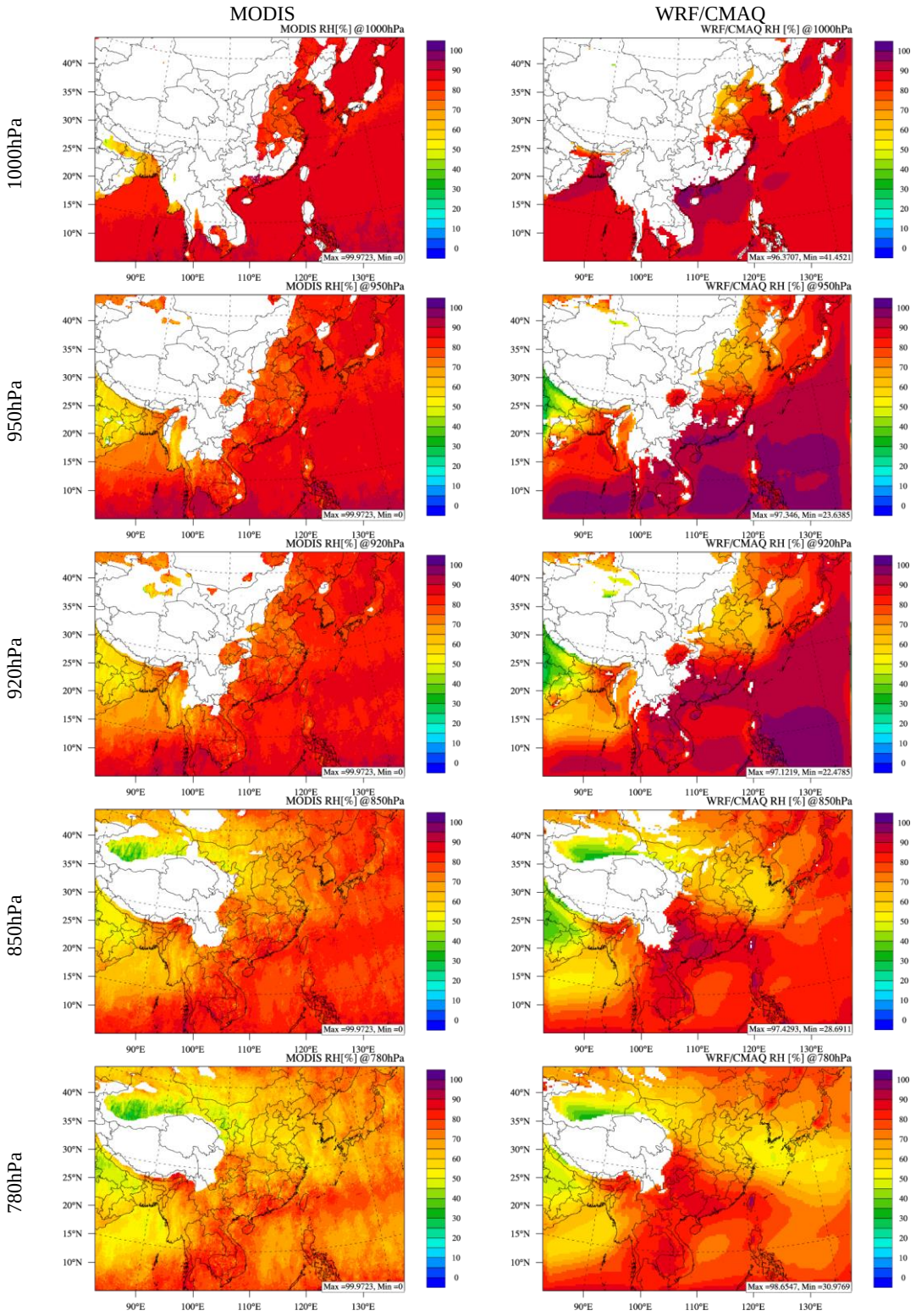

Figure 5.3 Continued

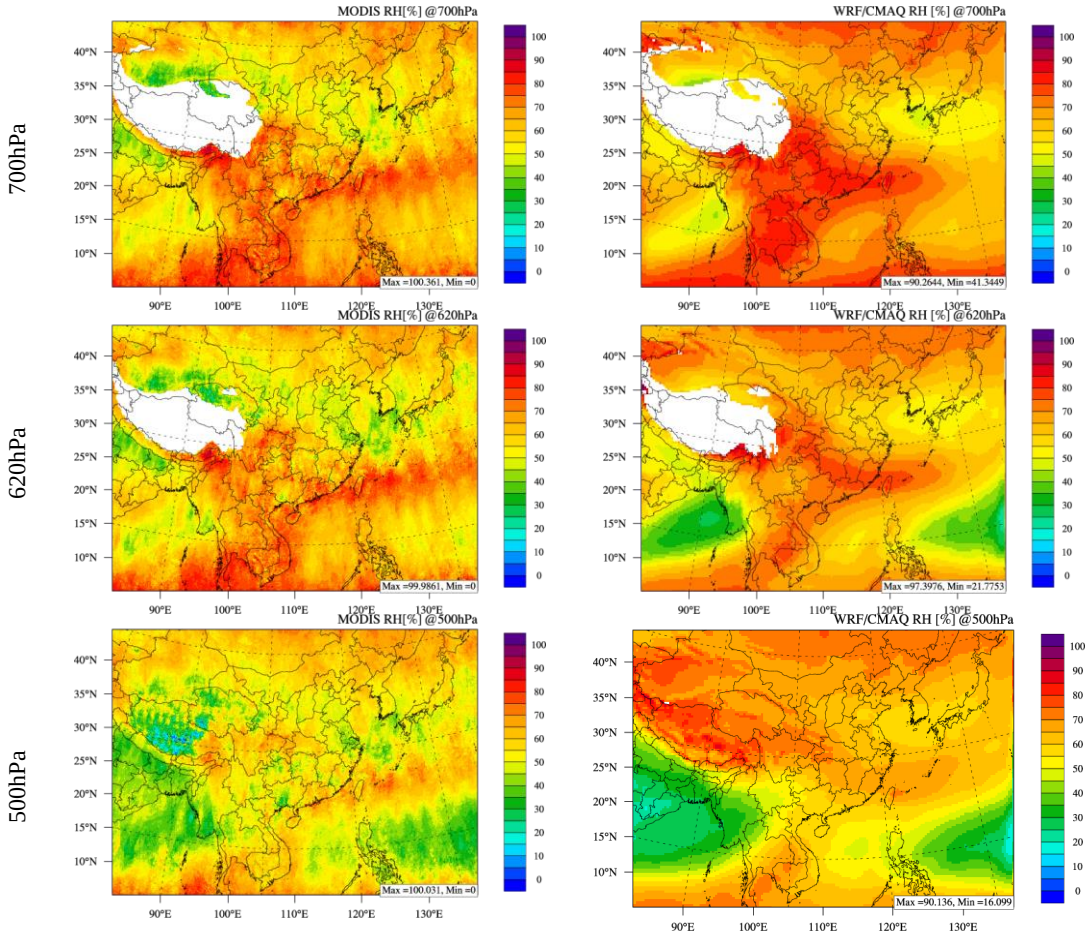

Figure 5.3 Continued

Table 5.2 Evaluation Statistics for T and RH

Variable	Pressure Level	Mean Obs	Mean Sim	MB	NMB (%)	R
T	1000hPa	293.85	294.20	0.35	0.12	0.99
	950hPa	290.77	290.81	0.04	0.01	0.99
	920hPa	288.98	289.22	0.24	0.08	0.98
	850hPa	284.47	285.03	0.55	0.19	0.99
	780hPa	280.58	280.97	0.39	0.14	0.99
	700hPa	275.32	276.00	0.68	0.25	0.99
	620hPa	269.27	270.65	1.39	0.51	0.99
	500hPa	258.71	260.58	1.87	0.72	0.99
RH	1000hPa	86.55	87.20	0.65	0.76	0.64
	950hPa	82.61	86.72	4.11	4.97	0.87
	920hPa	80.62	82.98	2.36	2.92	0.90
	850hPa	74.04	74.69	0.64	0.87	0.93
	780hPa	67.20	71.16	3.96	5.90	0.89
	700hPa	62.93	68.42	5.48	8.72	0.87
	620hPa	60.69	6.66	1.98	3.26	0.70
	500hPa	53.09	59.47	6.38	12.02	0.76

investigated pressure levels. The simulation bias is ±0.7% for T and ±12% for RH. The WRF/CMAQ system slightly overestimates T and RH at 850hPa~1,000hPa over South China Sea (SCS) and Bay of Bengal, due to the difficulties of simulating the air-sea interactions [*Meynadier et al.*, 2015; *Kim et al*, 2010]. The WRF/CMAQ system successfully reproduces the vertical profiles of T and RH over East Asia.

Regional climate models, including WRF, tend to overestimate precipitation [*Argueso et al.*, 2012; *Caldwell et al.*, 2009; *Schwartz et al.*, 2010] due to deficiencies within the convective cloud microphysical schemes. Aerosol may affect precipitation by changing the RF budget and altering the microphysical properties of rain cloud. The two-way mode WRF/CMAQ modeling system has included the direct impact of aerosol on precipitation. The WRF/CMAQ simulation of precipitation has never been evaluated over East Asia due to limited efforts of research. So in this section, observations from the TRMM and GPCC products are employed to evaluate the simulation of precipitation Figure 5.4 shows the spatial distribution of precipitation from observations and simulations. Table 5.3 summarizes the evaluation statistics.

TRMM shows 200mm precipitation over southeast China, Philippines, and the West Pacific in March, with a moderate increase by 50mm in April. Temporal change of sea surface temperature (SST) over the West Pacific has an overwhelming impact on the pre-monsoon precipitation over East Asia. The West Pacific High system starts to expend at the end of boreal spring due to the increase of SST, brings excessive water vapor to China, South Korea, and Japan and leads to the rain fall increase in April [*Yang and Lau*, 2004; *Xie et al.*, 2007].

Precipitation from the GPCP product is about 100mm higher than that from TRMM due to different algorithms used by different satellites. Simulations from the offline WRF and two-way mode WRF/CMAQ both reproduce the spatial distribution of precipitation as compared to the observations. But model simulations overestimate precipitation at the south boundary of modeling domain. Simulation bias is reduced from 50% in March and 35% in April with the offline WRF system to 46% in March and 27% in April with the two-way mode WRF/CMAQ system.

Figure 5.4 Spatial distributions of precipitation from the TRMM product, the GPCP product, the offline mode WRF simulation, and the two-way mode WRF/CMAQ simulation.

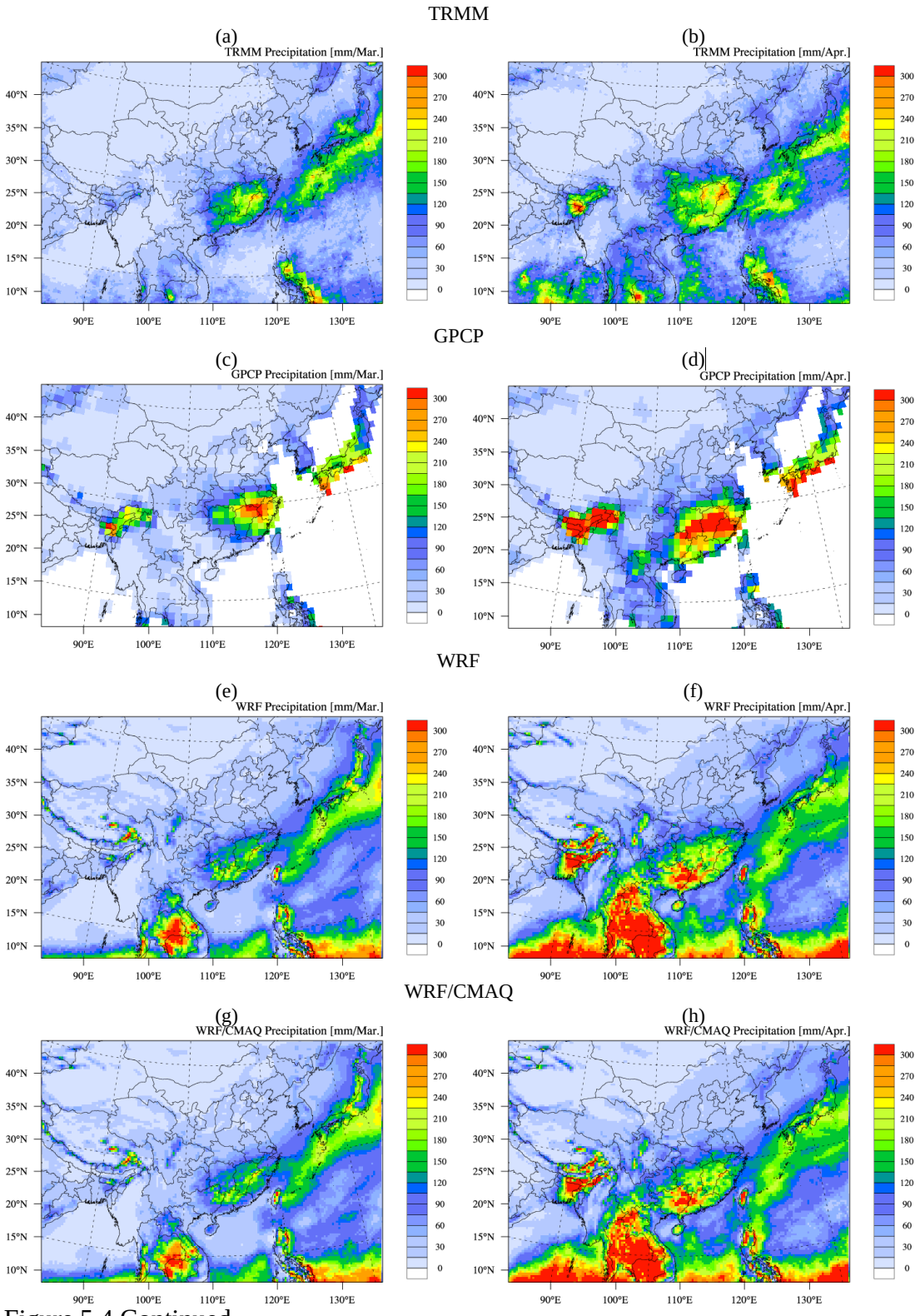

Figure 5.4 Continued

Table 5.3 Evaluation statistics for precipitation from the WRF (Offline) and WRF/CMAQ (Inline) simulations

Obs. Data	Month	Mean Obs(mm)	Mean Sim(mm)		MB (mm)		NMB (%)		R	
			Offline	Inline	Offline	Inline	Offline	Inline	Offline	Inline
TRMM	Mar.	43.79	64.97	63.30	21.15	19.51	48.30	44.55	0.83	0.84
	Apr.	65.35	101.51	98.86	36.16	33.51	55.33	51.28	0.81	0.81
GPCP	Mar.	38.56	50.63	48.29	12.07	9.73	31.32	25.24	0.68	0.70
	Apr.	63.58	85.90	82.24	22.32	18.66	35.11	29.36	0.72	0.71

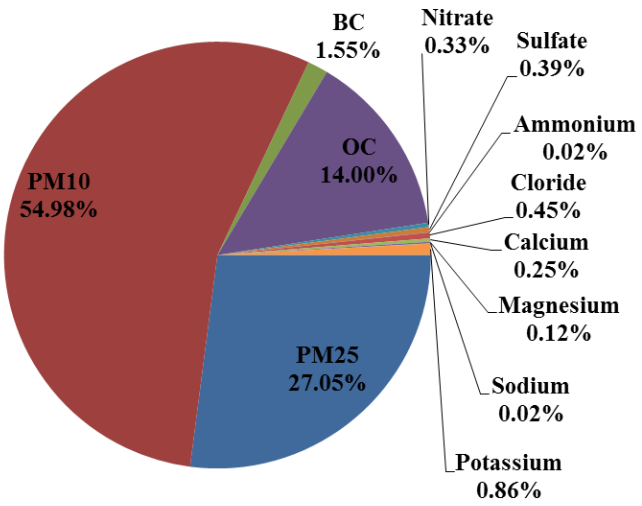

Figure 5.5 Mass contributions of aerosol subspecies to biomass burning emission, data is derived from emission factors described in Akagi et al. [2011]

5.4.2 **Impact of biomass burning aerosol on regional climate**

Since biomass burning contains both strong absorbing particles such as BC, OC and also scattering particles such as sulfate, nitrate, and ammonium, the impact of biomass burning aerosol on radiative forcing is a net effect of aerosol subspecies. Figure 5.5 shows the mass contributions of aerosol subspecies to biomass burning emission. Unspeciated PM_{10} and $PM_{2.5}$ compose 82% of biomass burning aerosol, followed by BC and OC aerosol as 15.5%. Inorganic aerosol and trace metals only compose less than 2.5% of the biomass burning aerosol.

Aerosol has cooling effect at TOA by reinforcing the backward reflecting flux, except when the underlying surface is covered by ice, snow, or cloud which has higher scattering albedo than the aerosol. Absorbing aerosol above cloud (AAC) usually leads to reduction of upward flux at TOA due to the higher albedo of the underlying cloud. Chapter 3 demonstrates that biomass burning aerosol is lifted up into free troposphere due to the lee side trough on the right side of Tibet Plateau. So the PSEA biomass burning may induce excessive aerosol above the cloud and subsequently alter the radiative forcing budget. Wang et al. [2013] also reported observed significant upper layer (3km~4km) transport of biomass burning aerosol over East Asia. Figure 5.6 shows the biomass burning aerosol induced SWR flux change. The five-year averaged impact of biomass burning on SWR flux under clear sky condition at TOA ranges from -6W/m^2 over PSEA to 3W/m^2 over SCS. The upwelling SWR flux at TOA represents the total solar radiation reflected by Earth's surface, cloud, and aerosol. Thus the negative SWR change at TOA represents a warming effect of the aerosol. So the -4% reduction of SWR flux at TOA of PSEA suggests that biomass burning has a slightly warming effect over the source area. Over SCS where the ocean surface albedo is less than 0.1 under clear sky condition, elevated biomass burning aerosol slightly increase the upward SWR flux at TOA by 2%, indicating an overall cooling effect over the ocean. Under all sky condition, the upwelling SWR flux at TOA is reduced by 4W/m^2~20W/m^2 (-4%~-12%) over PSEA and SCS due to the impact of biomass burning. The large difference between all sky and clear sky conditions indicates a strong correlation between biomass burning aerosol and cloud. Some studies have identified the existence of a persistent stratocumulus cloud

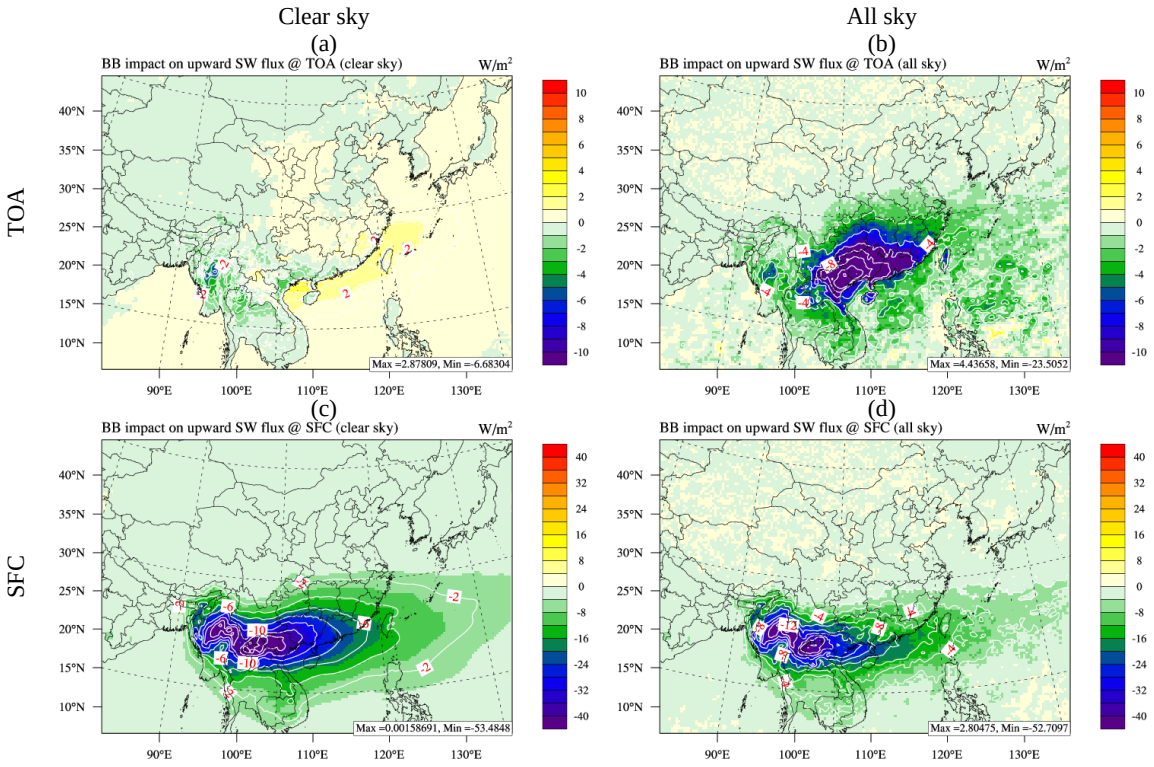

Figure 5.6 Impact of biomass burning aerosol on SWR flux at TOA and SFC under clear and all sky conditions. Color contours represent the absolute changes of SWR flux, and the white dash lines with red markers represent the percentage contribution

deck over north Vietnam and south China based on satellite observations [*Lin et al.,* 2014; *Galvin et al.,* 2007]. Stratocumulus cloud is frequently formed among subtropical area and it typically occupies the upper few hundred meters of PBL [*Wood et al.,* 2012]. While biomass burning aerosol is lifted up into free troposphere over south China and the West Pacific, the underlying stratocumulus cloud deck explains the strong warming effect of biomass burning under all sky condition.

Figure 5.7 shows the spatial distribution and vertical profile of cloud fraction from the WRF/CMAQ simulation and the AIRS product. Cross sectional distribution of biomass burning BC concentration is also analyzed to investigate the relationship between biomass burning and stratocumulus cloud. Figure 5.7(a) shows distinct cloud fraction at the eastern and western side of Yungui Plateau. Cloud fraction is more than 15% on the eastern side and less than 5% on the western side, indicating the existence of persistent cloud at north Vietnam and south China. Figure 5.7(b) compares the vertical distribution of cloud fraction from WRF/CMAQ simulation and the AIRS product at a selected grid over eastern side of Yungui Plateau. Due to the coarse grid solution of AIRS (5°×5°), all the model simulations falls in this grid cell are used to calculate the average cloud fraction as well as the maximum and minimum values. Although large discrepancy is found at 750hPa~450hPa between WRF/CMAQ and AIRS, both simulation and satellite observation suggest the existence of a persistent stratocumulus layer at around 800hPa on the eastern side of Yungui Plateau. Figure 5.7(c) shows the cross sectional distributions of cloud fraction and biomass burning BC concentration. Over north Vietnam and south China (around 110°E longitude), existence of cloud is identified below 2km height, while biomass burning BC is lifted up above 2.5km height. The AAC identified in Figure 5.7(c) indicates that biomass burning aerosol not only causes the significant drop of scattering albedo, but also affects the polarized light reflectance of the underlying cloud [*Waquet et al.,* 2013]. The presence of AAC over PSEA and south China has been investigated by some measurement-based studies. With multiple satellite products, Hsu et al. [2003] reported that the PSEA biomass burning aerosol is frequently lifted up above clouds and reduces the reflected solar radiation over cloudy areas by up to 100W/m^2 due to the direct and indirect effects. Feng and Christopher [2015] also

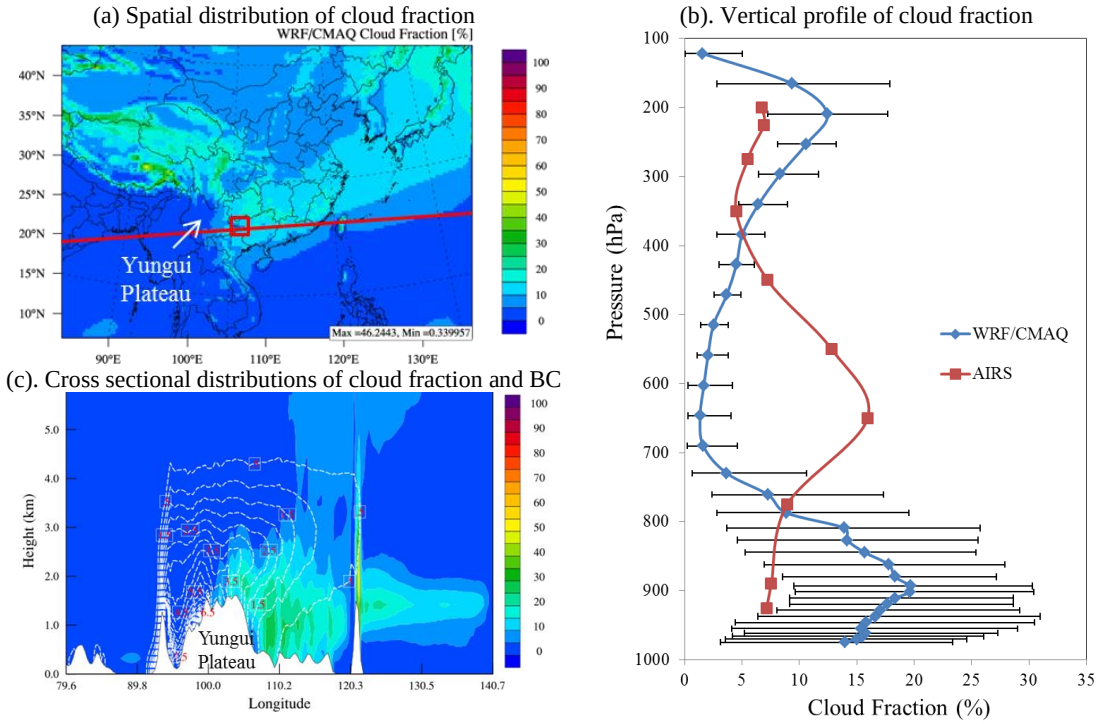

Figure 5.7 (a) Cloud fraction from WRF/CMAQ simulation; (b) Vertical profiles of cloud fraction from WRF/CMAQ simulation and the AIRS product at the selected grid (red rectangles in Figure 5.7(a)); (c) Cross Sectional distributions of cloud fraction (color contour), and biomass burning BC concentration (white dash lines with red markers with unit of $\mu g/m^3$).

examined satellite products and reported that the AAC radiative effect is $36.7W/m^2 \pm 20.5W/m^2$ over western Africa. These measurement-based estimations are comparable with the simulation-based estimation from this work. This study is the first investigation of AAC with the coupled meteorology and chemical transport modeling system.

As a result of altering solar radiation flux, biomass burning aerosol changes the air temperature profiles by cooling the lower and warming the upper air simultaneously. Figure 5.8 shows the biomass burning aerosol induced temperature changes at different model layers. The altitude height is used here instead of the pressure height because of the complex topography over PSEA. At near surface layers, air temperature is reduced by up to 0.8K at 20m and 0.3K at 530m, following the similar spatial distribution as changes of downward SWR flux. Near surface air temperature is reduced over inland areas of PSEA and south part of China. Biomass burning aerosol increases air temperature by up to 0.25K in the upper air from 800m to 2.5km height. Spatial distributions of the air temperature change also reveals that the impact of biomass burning is confined over land area. The SST over SCS is hardly affected by biomass burning aerosol due to the low surface albedo of ocean water. As the most significant temperature changes are identified over north Vietnam and south China, air temperature vertical profile is investigated at four selected sites within this area. These sites are: Simao, Hanoi, Baise, and Naning. Figure 5.9(a) shows the comparison of air temperature vertical profiles between the WRF/CMAQ simulations and local ground-based sounding observations during the massive burning event on March 7th 2007. Simulations and sounding observations are in close agreement with each other at all the four sites. Figure 5.9(b) shows the biomass burning induced air temperature changes at these four sites. Hanoi (21.01 ℃N, 105.80 ℃E) lies inside the flat low-lying Red River Delta plain in north Vietnam with terrain height of only a few meters. The PSEA biomass burning aerosol at Hanoi is constrained within the inversion layer [Wang et al., 2010] and subsequently warms the air by 2.5K at 1000m height. Simao (22.76 ℃N, 100.98 ℃E), Baise (23.90 ℃N, 106.60 ℃E) and Naning (22.63 ℃N, 108.21 ℃E) are located at Yungui Plateau with terrain height of more than 1.3km. Biomass burning

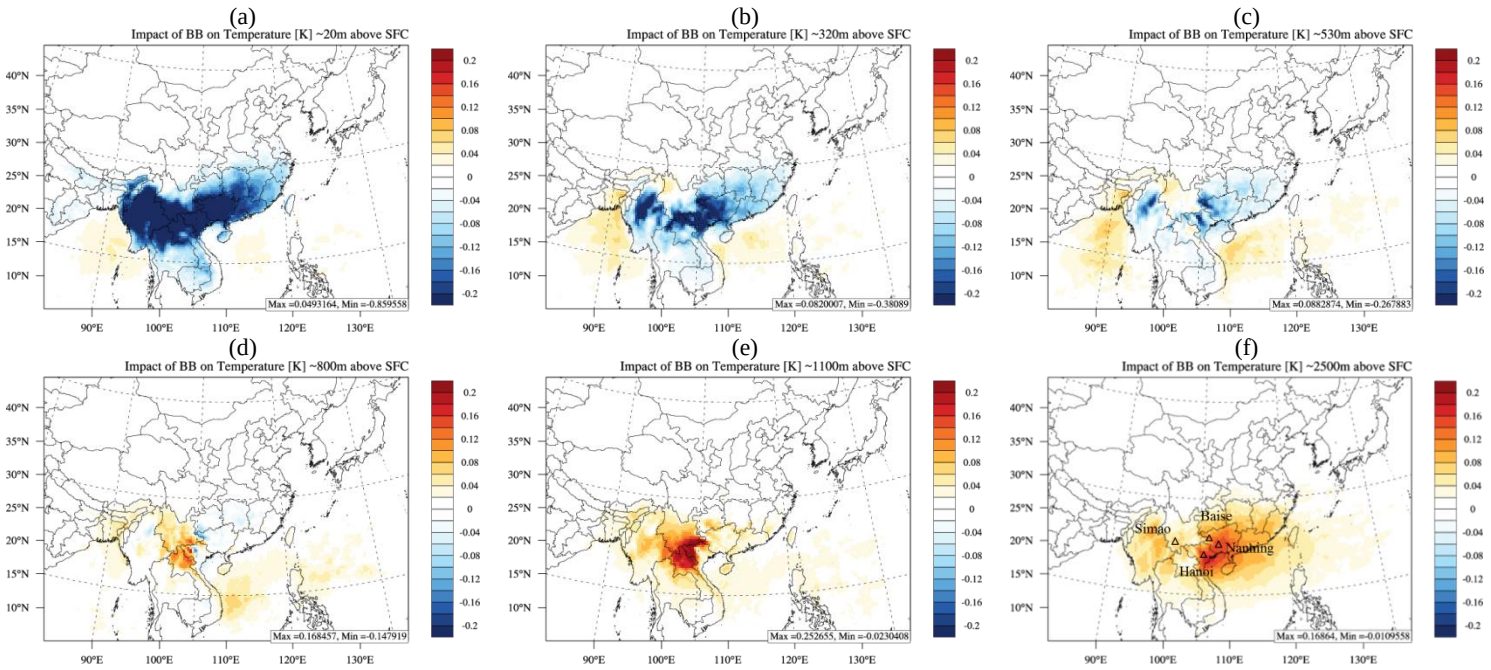

Figure 5.8 Biomass burning aerosol induced temperature changes at (a) 20m; (b) 320m; (c) 530m; (d) 800m; (e) 1100m; and (f) 2500m above the surface ground. Upward triangles in (f) represent the locations of ground-based stations with sounding data.

(a) Comparison of temperature vertical profiles between WRF/CMAQ and sounding observation

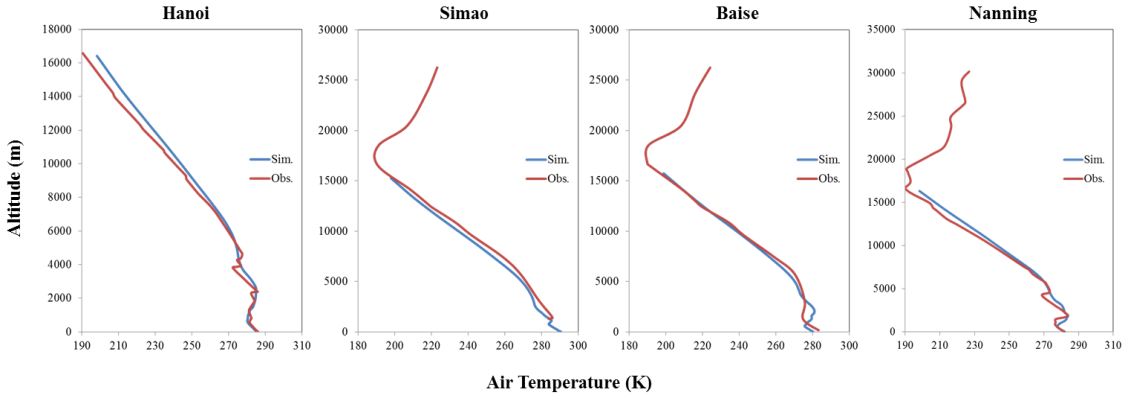

(b) Biomass burning aerosol induced temperature profile changes

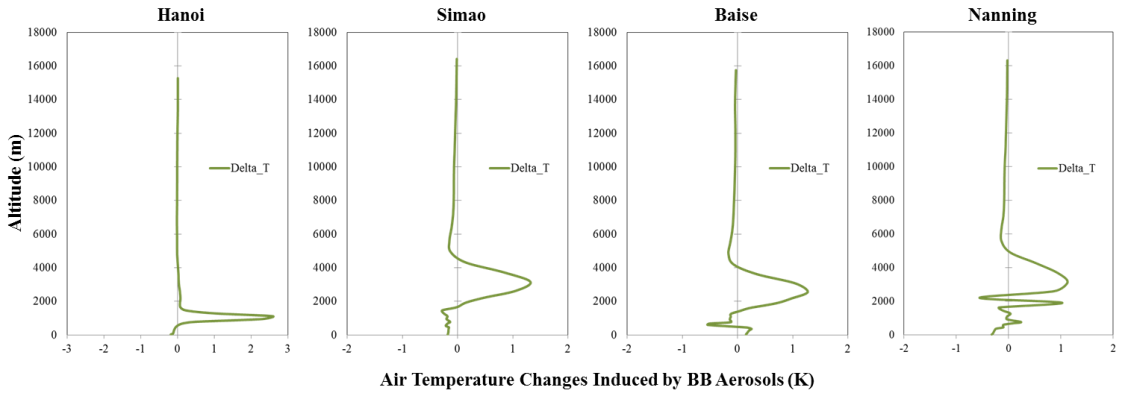

Figure 5.9 (a) Comparison of air temperature profiles between the WRF/CMAQ simulations and sounding observations; (b) Biomass burning aerosol induced temperature change

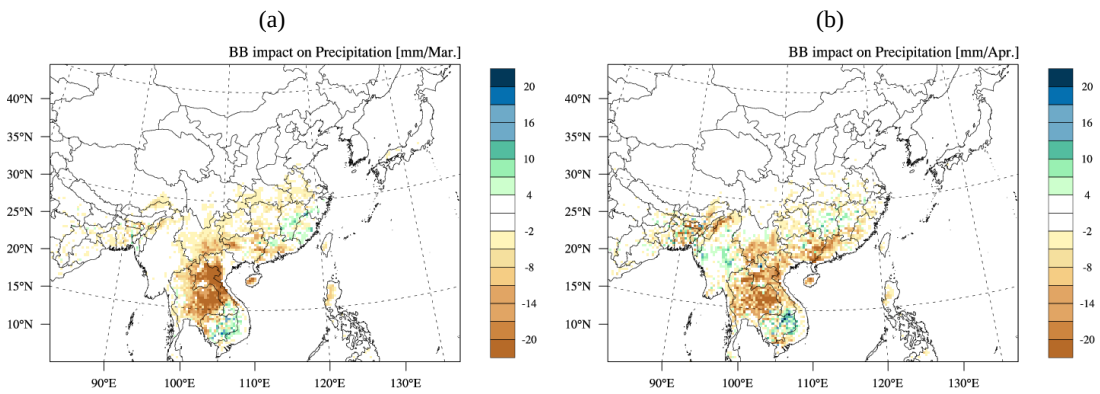

Figure 5.10 Spatial distribution of biomass burning aerosol induced precipitation change

aerosol transported from PSEA is lifted up into free troposphere at these three cites, and subsequently increases the upper air temperature by 1K at 3km height.

Cooling at lower and warming at the upper atmosphere leads to increase of stability and decrease of convection. PSEA biomass burning is active from early Marh to late April, and the East Asia Monsoon usually starts from May. The impact of biomass burning on radiative forcing and air temperature profile also affects the pre-monsoon precipitation over PSEA and south China. Figure 5.10 shows the monthly precipitation changes induced by biomass burning aerosol over land area. Zhang et al. [2003] reported that in current mesoscale numerical simulation, small initial difference may grow rapidly due to the nonlinearities in the convective and microphysical parameterizations. The reinforced initial difference changes the timing and position of convective cells, and subsequently causes unexpected change of moisture convection and precipitation. So the change of precipitation over ocean area is not analyzed in this work due to the contamination caused by excessive moisture. As shown in Figure 5.10 (a) and (b), monthly average precipitation is reduced by 10mm/month (2%) over PSEA and south China. Thermodynamic forcing caused by biomass burning aerosol is demonstrated to stabilize the lower atmosphere and suppress the convective precipitation by 0.02mm/day (2%) over Amazonia [*Zhang et al.,* 2009], which is quite consistent with the finding from this study. Tosca et al. [2010] reported overall 10% precipitation decrease due to impact of biomass burning over equatorial Asia during El Niño. A recent study by Lee et al. [2014] suggested about 40% of precipitation reduction is due to direct effect of biomass burning aerosol based on simulation with GEOS-5 Atmospheric Global Climate Model (AGCM). But Lin et al. [2014] commented that the work by Lee may be influenced by the simplified microphysical parameterizations necessitated by the model. The studies mentioned above indicate the challenges for representing the convective precipitation by model. The understanding of the indirect effect of aerosol is also poorly developed [*Mechem et al.,* 2010a, 2010b; *Feingold et al.,* 2006]. Since modeling study of the biomass burning aerosol impact on precipitation is not well documented in the literature, more research effort is necessary to reveal the interactions between biomass burning aerosol and cloud.

5.4.3 **Impact of dust on regional climate**

Monthly averages of dust induced SWR changes at TOA and SFC are demonstrated in Figure 5.11. Under clear sky condition, upwelling SWR flux is increased by 10W/m^2 (8%) over East Asia as dust aerosol has higher scattering albedo than the underlying land surface. East Asian dust is usually transported with cold frontal system under high pressure and cloud free condition over desert area. So dust aerosol has very limited impact on the upward SWR flux at TOA under all sky condition as shown in Figure 5.11(b). But over cloudy areas including the West Pacific, Japan, and south China, dust aerosol is lifted up above the cloud and slightly reduces the underlying surface albedo and subsequently decreases the upward SWR flux at TOA. The only exception is found for the eastern Tibet Plateau, where the reflecting flux is significantly reduced by 20W/m^2 (8%) due to the high surface albedo of snow within this area. Figure 5.12 shows the snow cover from Northern Hemisphere Snow Cover Monthly Statistics (NHSNOWM) product produced by NOAA [*Ramsay B.*, 1998]. The NHSNOWM product indicates high snow coverage of this region. East boundary of Tibet Plateau is outlined by Hengduan Mountains which blocks the eastward moisture fluxes and generates the persistent snow coverage. The elevated wind-blown dust emitted from Tibet Plateau is also blocked by the Hengduan Mounts. Thus the suspended dust over snow reduces the surface albedo and decreases the SWR flux at TOA under both clear and all sky conditions. Dust induced SWR flux change at SFC ranges from more than -60 W/m^2 (16%) over Tibet and central China to -20W/m^2 (-8%) over the West Pacific and Japan under clear sky condition. The impact of dust under all sky condition is slightly less intensive, which ranges from -20W/m^2(-4%) over the West Pacific to more than -40W/m^2 (12%) over northwest China.

Findings from WRF/CMAQ simulation in this work shows consistent assessment as compared with other studies. Table 5.4 summarizes the recent evaluations of dust impact on radiative forcing over East Asia. Estimation from WRF/CMAQ and estimations from other studies are in close agreement with each other.

Figure 5.13 shows the spatial distribution of dust induced temperature changes at different heights. At near surface layer, air temperature is reduced by -0.5K at 50m~610m

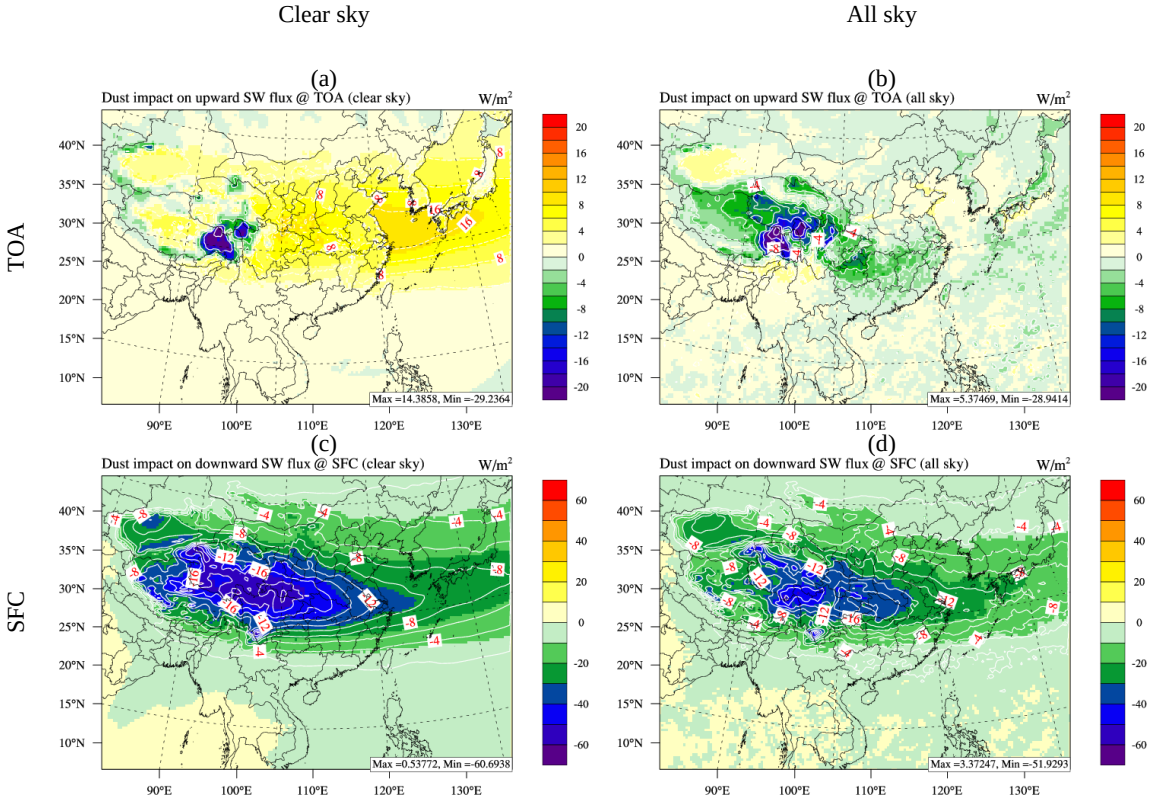

Figure 5.11 Impact of dust aerosoll on SWR flux at TOA and SFC under clear and all sky conditions. Color contours represent the absolute changes of SWR flux, and the white dash lines with red markers represent the percentage contribution

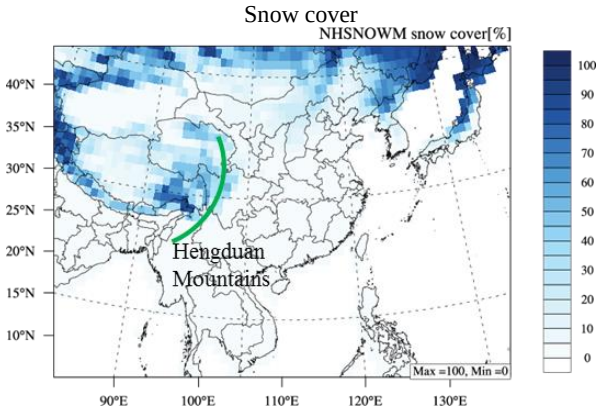

Figure 5.12 Snow cover from the NHSNOWM product. Green curve represents the location of Hengduan Mountains

Table 5.4 Dust aerosol impact on SW flux at TOA and SFC under clear sky condition

Region	Method	Dust induced change @ TOA (W/m^2)	Dust induced change @ SFC (W/m^2)
South Korea	CCM3 [*Won et al.,* 2005]	5 ~ 10	-20 ~ -10
	This study	5 ~ 10	-30 ~ -10
East China	CCM3 [*Park et al.,* 2005]	10 ~ 20	-40 ~ -10
	ADAM [*Park et al,* 2008]	-	-40 ~ -20
	This study	5 ~ 15	-60 ~ -20
Tibet	MFRSR [*Ge et al.,* 2011]	-4 ~ 3	-20 ~ -10
Plateau	fvGCM [*Lau et al.,* 2006]	-2	-13
	WRF-Chem [*Chen et al.,* 2013]	-4	-6
	This study	-30 ~ 5	-10 ~ -60
Taklamkan	RTM, CALIPSO[*Kuhlmann and Quaas,* 2010]	-	-60 ~ -90
	This study	0 ~ 5	-20 ~ -40

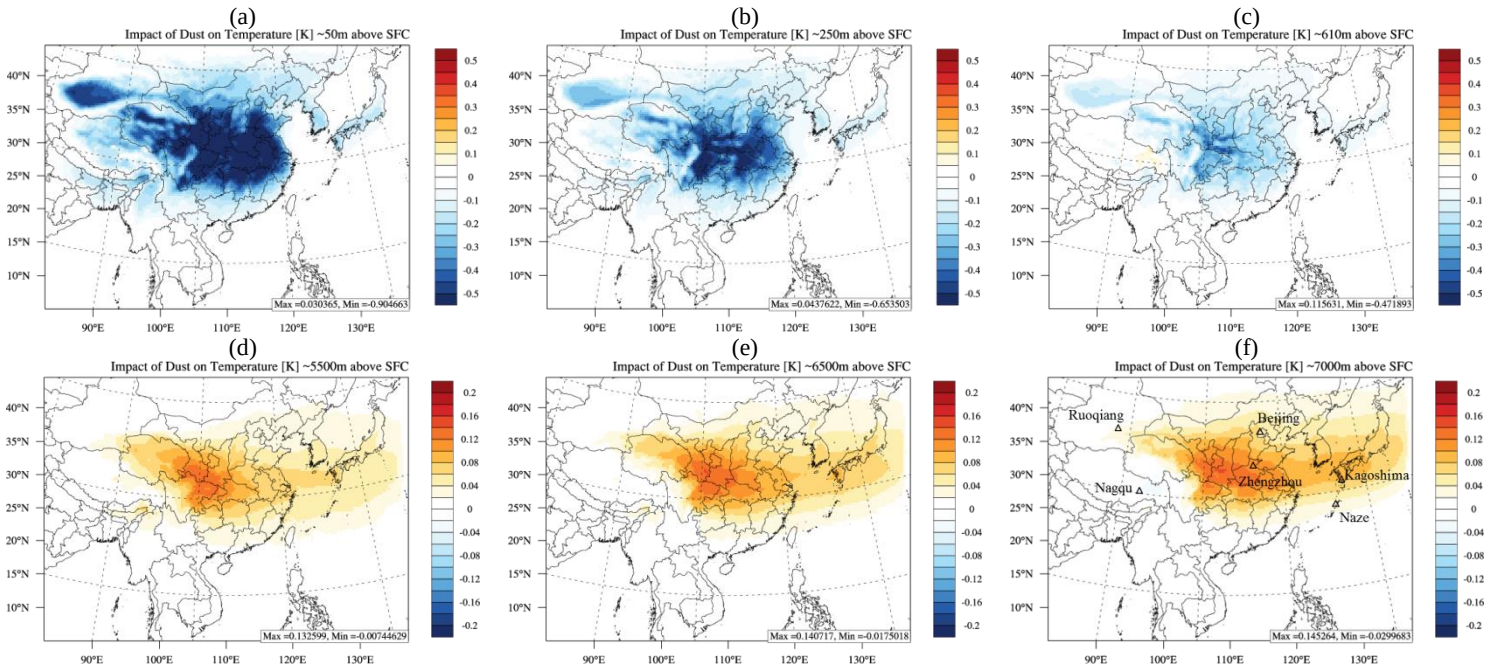

Figure 5.13 Dust induced temperature changes at (a) 50m, (b) 250m, (c) 610m, (d) 5,500m, (e) 6,500m, and (f) 7,000m above the surface ground. Upward triangles in (f) represent the locations of ground-based stations with sounding data

height over central and east China, South Korea, and Japan. Cooling effect of dust is limited under 1km height above surface ground due to its scattering effect. Elevated dust aerosol warms the upper air within the range of 5km~7km height by less than 0.2K. Some in-site measurements [*Huebert et al.,* 2003; *Clarke et al.,* 2004; *Shi et al.,* 2005; *Mikami et al.,* 2006] suggested that dust aerosol is slightly absorbing with single scattering abledo (ω_0) falls in the range of 0.90~0.99. But the absorbing effect of different aerosol subspecies within the dust plume has not been considered by models. In this study the source-dependent mineralogical distribution profile is incorporated into the WRF/CMAQ system, and enables the model to identify the overall absorbing effect as a result of all the different aerosol subspecies.

Figure 5.14(a) shows the comparison of air temperature vertical profile between the WRF/CMAQ simulation and the sounding observations. Dust induced changes of temperature profile are investigated at six selected sites as shown in Figure 5.14(b). These sites include: two sites in desert region: Ruoqiang (39.03 ℃N, 88.16 ℃E) and Nagqu (31.48 ℃N, 92.06 ℃E); two sites in central China: Beijing (39.93 ℃N, 116.28 ℃E) and Zhengzhou (34.71 ℃N, 113.65 ℃E); and two sites in the West Pacific: Kagoshima (31.55 ℃N, 130.55 ℃E) and Naze (28.38 ℃N, 129.55 ℃E). These sites are selected to evaluate the evolution of dust impact along the transport pathway. Their locations are shown in Figure 5.13(f). The CALIPSO aerosol subtype product is used in this section to identify the vertical distribution of dust, as shown in Figure 5.15. Dust plume is identified at 1km~4km height over The Taklamakan Desert, 1km~8km height over central and north China, and 1km~6km height over the West Pacific. The CALIPSO product also suggests that clean dust particles are gradually contaminated along the transport pathway from northwest China to the West Pacific. At Ruoqiang and Nagqu, the clean dust aerosol shows a cooling effect within the near surface air and decreases air temperature by less than 0.5K. At Beijing and Zhengzhou, the partially contaminated dust aerosol cools near surface air by up to 0.9K and also warms upper air by 0.1K. At Kagoshima and Naze, the polluted dust aerosol slightly cools the near surface air by less than 0.1K, but significantly warms the upper air by 0.2K. Impact of dust aerosol shows distinct influences along the transport pathway. The clean dust aerosol dominates the cooling

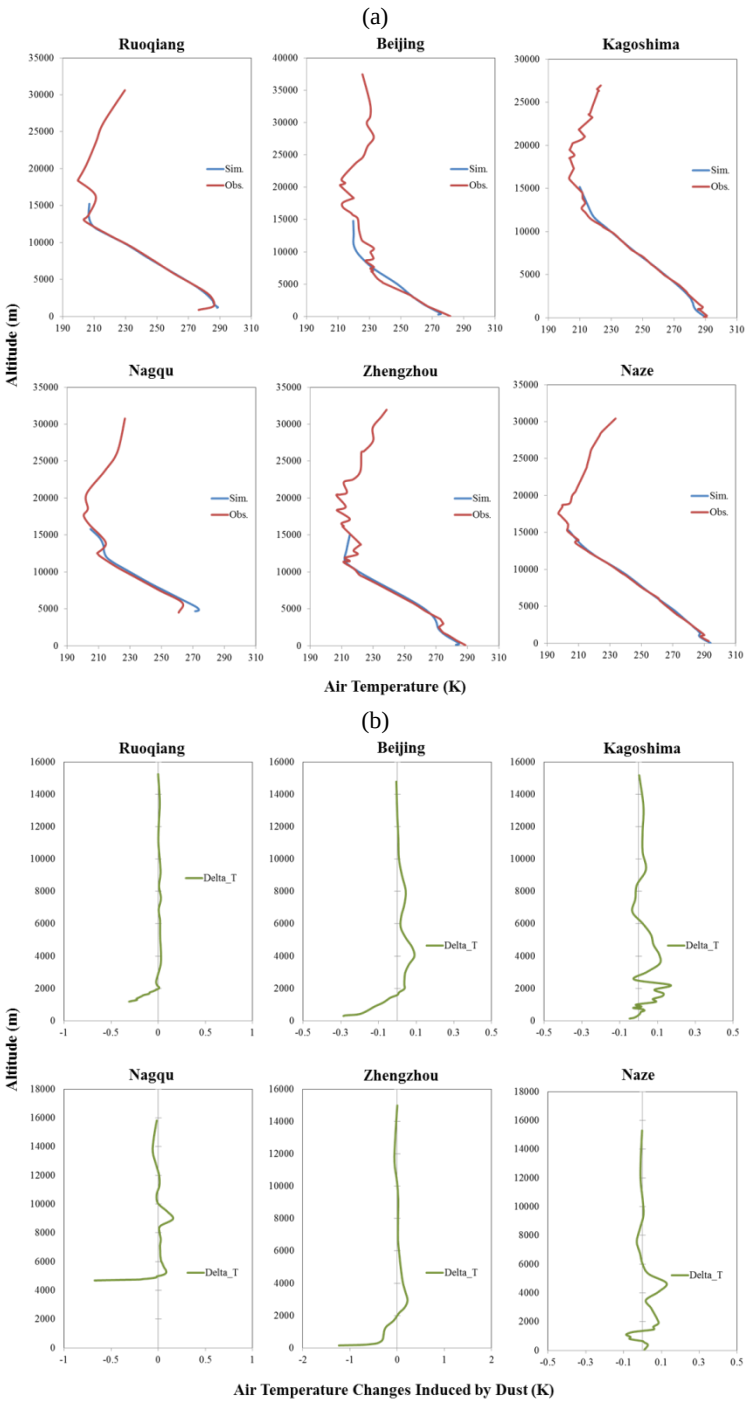

Figure 5.14 (a) Comparison of temperature profiles between the WRF/CMAQ simulation and sounding observations; (b) Dust induced temperature change

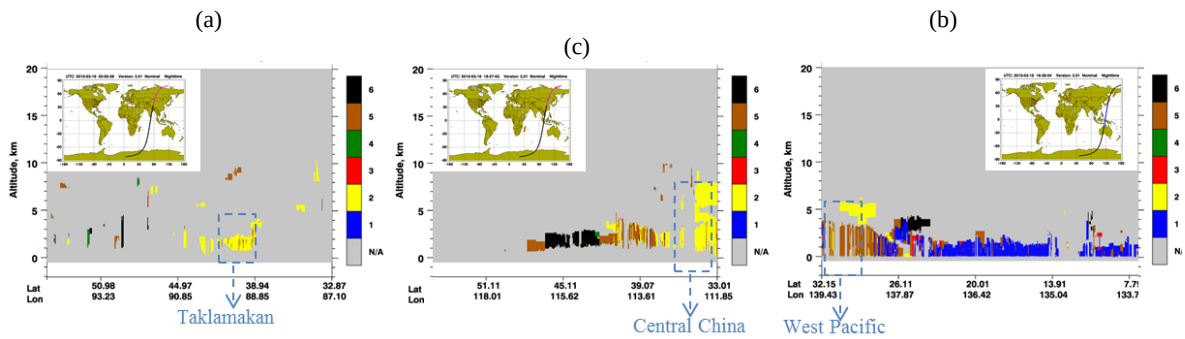

N/A = not application; 1 = clean marine; 2 = dust; 3 = polluted continental; 4 = clean continental; 5 = polluted dust; 6 = smoke

Figure 5.15 CALIPSO aerosol subtype product on Mar.16th 2010

effect at near surface air over desert area. The partially contaminated dust aerosol shows comparable cooling effect at near surface air and warming effect at upper air over central and eastern China. The fully polluted dust aerosol dominates the warming effect at upper air over the West Pacific. Contamination induced by anthropogenic emission alters the optical properties of dust aerosol by decreasing the cooling effect and reinforcing the warming effect. This study is the first investigation into the evolution of dust aerosol impact on regional climate with the WRF/CMAQ modeling system.

5.4.4 **Coexistence of biomass burning and dust**

As introduced in previous chapters, biomass burning aerosol is brought into south China and the West Pacific by the Westerlies from PSEA. Simultaneously, dust aerosol is also transported by northwest winds toward south China and the West Pacific. This section investigates the coexistence of biomass burning and dust at Taiwan, because the local MPL observation helps to identify the presence of distinct aerosol layers. Many research efforts have been devoted to investigate the impacts of biomass burning and dust storm at Taiwan. However, the coexistence of biomass burning and dust is not well documented due to limited research. Understanding of the mixing status, the frequency of coexistence and the subsequent impact on air quality is poorly developed. In this study, the coexistence of biomass burning is evaluated by the following steps. At the first step, daily MPL observation at the Taiwan EPA-NCU station (24.97°N, 121.18°E) is analyzed to identify the presence of multiple aerosol layers. A total of eight cases are found to have at least two distinct aerosol layers, including three cases in 2006 (Mar.4th, Mar.10th and Mar.29th), one case in 2008 (Mar.4th), three cases in 2009 (Apr.18th, Apr.24th and Apr.27th), and one case in 2010 (Mar.11th). At the second step, the HYSPLIT model is applied to investigate the transport trajectories of biomass burning and dust. At the third step, the WRF/CMAQ simulation is analyzed investigate the spatial distribution of biomass burning and dust. The MODIS product is also used to verify the indications from HYSPLIT and the WRF/CMAQ system. And at the last step, the WRF/CMAQ simulation is analyzed to evaluate the impact of the mixed aerosol on radiative forcing under coexistence condition. The CALIPSO aerosol subtype product is also used to

verify the coexistence of biomass burning and dust in case it is available. By following the approach mentioned above, two cases are confidently identified as having the coexistence of biomass burning and dust aerosol, including the Mar.29th 2006 case and Mar.11th 2010 case.

Figure 5.14 shows the coexistence case on Mar.29th 2006. The MPL observation shown in Figure 5.14(a) suggests that there are three distinct aerosol layers at 1km, 2km, and 4km height respectively. The lowest aerosol layer should be associated with the local anthropogenic emission since the EPA-NCU station is located inside the urban center of Taoyuan city. Figure 5.14(b) shows the back trajectory analysis performed with HYSPLIT model for four consecutive days from Mar.26th to Mar.29th. HYSPLIT suggests air plumes transported from the Gobi Desert, PSEA, and central China are responsible for the aerosol layers at 4km, 2km, and 1km respectively. Figure 5.14(c) shows the distribution of PSEA biomass burning BC, and Figure 5.14(d) shows the distribution of unspeciated coarse mode dust (ASOIL). Cross sectional distributions of biomass burning BC and dust ASOIL are also demonstrated to identify the vertical distribution of biomass burning and dust aerosol. The transport trajectories of biomass burning and dust are consistent between the HYSPLIT prediction and the WRF/CMAQ simulation. On one hand, the lifted biomass burning aerosol is carried by the Westerlies toward Taiwan at the upper air within 3~5km height. On the other hand, wind-blown dust is elevated at the Gobi Desert but it subsides rapidly during the southeastward transport and remains in 2km~3km height when it arrives at Taiwan. Spatial distribution of the MODIS AOD also suggests presence of biomass burning aerosol transport from Southeast Asia to Taiwan. MODIS is unable to identify dust storm due to the contamination by cloud over the Gobi Desert, but it also indicates high column density of aerosol over Taiwan. Vertical distributions of the biomass burning BC and dust ASOIL are shown in Figure 5.14(f). The temperature profile changes due to impact of biomass burning and dust are also demonstrated. Dust aerosol lies in 2km height and biomass burning aerosol lies in 4km height as indicated by the WRF/CMAQ simulation, which explains the two distinct aerosol layers identified by MPL observation. Changes of temperature profile agree well with the vertical distribution of aerosol. Air temperature is

Figure 5.16 Coexistence of biomass burning and dust aerosol at the MPL EPA-NCU site in Taiwan on Mar.29th 2006. (a) MPL normalized back scatter observation; (b) HYSPLIT back trajectories from Mar.26th to Mar.29th; (c) Spatial (upper panel) and cross sectional (lower panel) distributions of biomass burning BC; (d) Spatial (upper panel) and cross section distributions of dust ASOIL; (e) MODIS AOD; (f) Vertical profiles of aerosol concentrations and temperature change

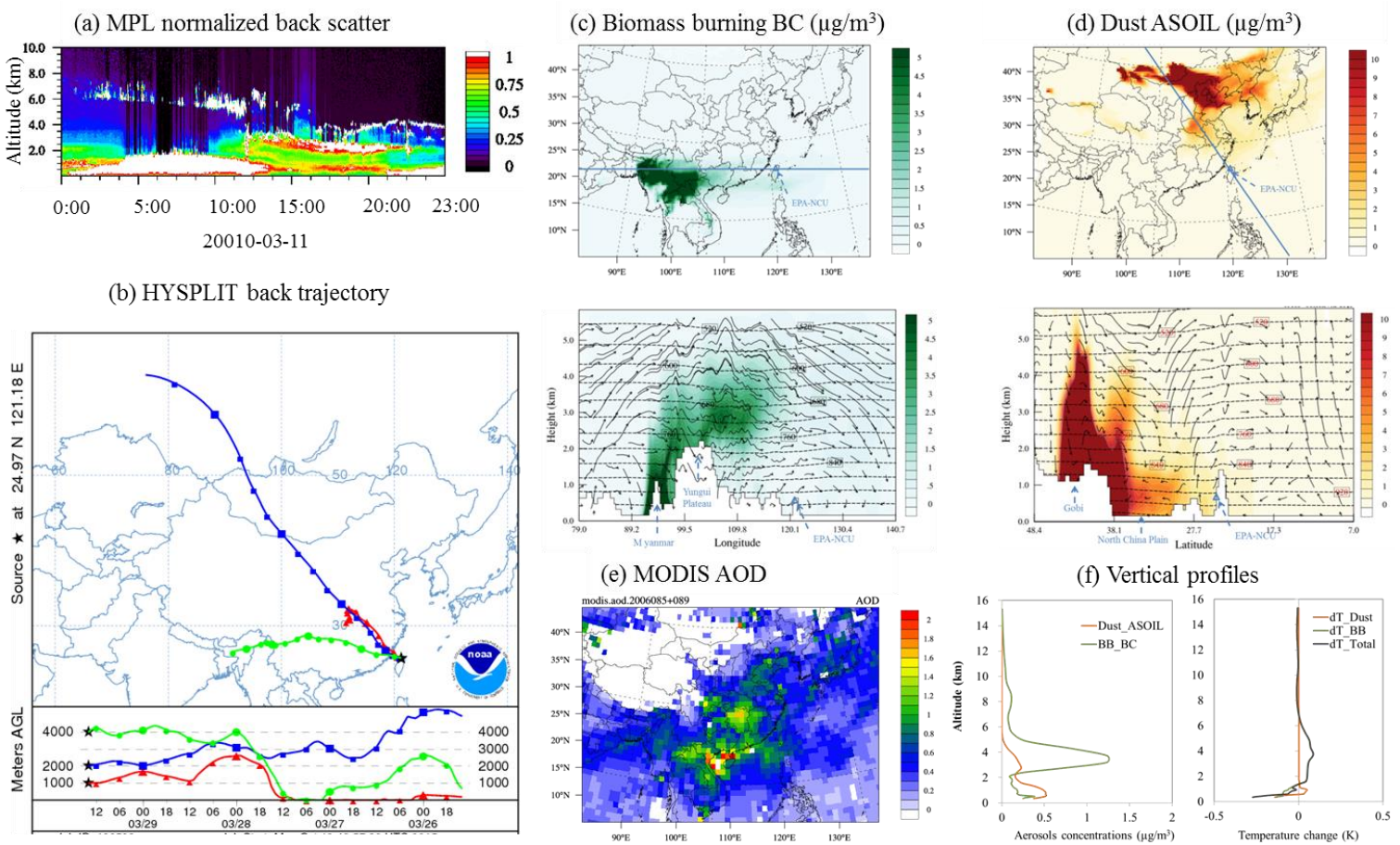

Figure 5.16 Continued

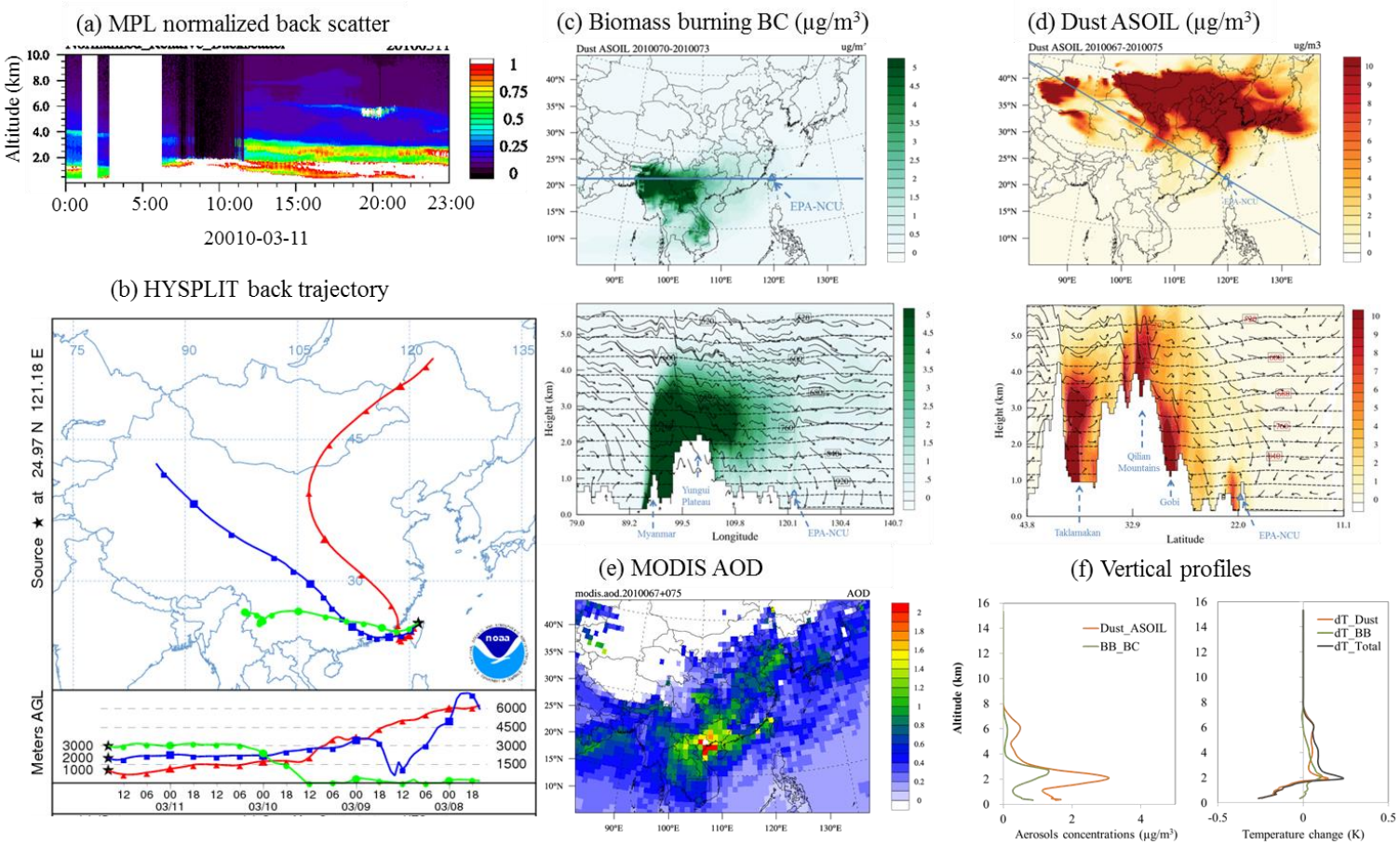

Figure 5.17 Same as Figure 5.16 but for the coexistence case on Mar.11th 2010

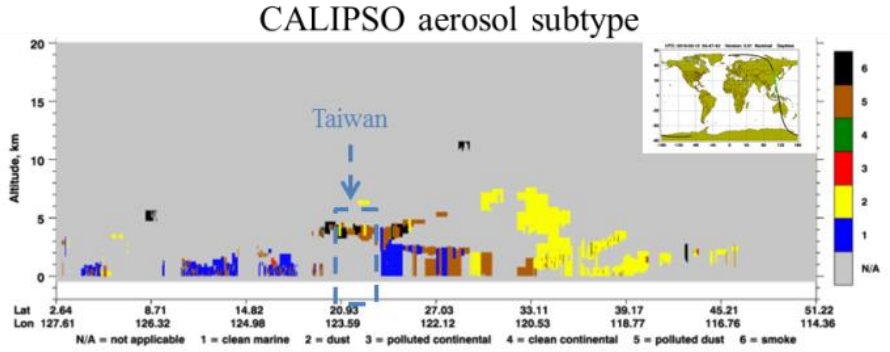

Figure 5.18 CALIPSO aerosol subtype on Mar.11th 2010

reduced by -0.15K at near surface layer as a result of the cooling effect from dust, and increased by +0.05K at upper air as a warming effect of biomass burning.

Another coexistence case occurs on Mar.11th 2010. The MPL observation identifies two neighboring aerosol layers at 2km height, which are revealed as the biomass burning from Myanmar and dust from both Gobi and Taklamakan Desert. Vertical distributions of BC and ASOIL suggest that biomass burning and dust aerosol almost mix with each other at 2km height. The CALIPSO aerosol subtype product shown in Figure 5.16 also suggests the mixing of smoke (biomass burning) and polluted dust aerosol at Taiwan on Mar.12th 2010. And as a result of the mixed aerosol, air temperature is decreased by 0.25K at near surface layer and the increased by 0.2K at the upper air.

The air temperature changes under the coexistence condition are consistent with the changes with the presence of one single type of aerosol, as indicated by Figure 5.9(b), Figure 5.14(b), 5.15(f) and Figure 5.16(f). In summary, biomass burning aerosol favors the warming of upper air while dust favors the cooling of near surface air. The investigation about coexistence of biomass burning and dust is very limited. Johnson et al. [2008] reported that the upper biomass burning aerosol layer absorbs 10% more back reflected SWR with the presence of underlying dust layer over West Africa. To evaluate the SWR changes induced by underlying dust with above biomass burning, the aerosol direct radiative effect efficiency Eτ for dust (Eτ_Dust) and biomass burning (Eτ_BB) is investigated as shown in Figure 5.18. Eτ is defined as the DRE per unit of aerosol optical depth and has been applied for evaluating the radiative efficiency of different aerosol species [*Yu et al.,* 2006; *Li et al.,* 2004; *Xing et al.,* 2015]. The upwelling SWR at TOA under clear sky (SWUPTC) is divided by the aerosol induced changes of AOD in this section to calculate Eτ. The "No mixing" category refers to the presence of pure dust or pure biomass burning aerosol. The "Mixing" category refers to coexistence case on Mar.11th 2010, and the "Overlay" category refers to the case on Mar.29th 2006. Eτ_Dust changes from 25$Wm^{-2}\tau^{-1}$ under pure dust condition to 22$Wm^{-2}\tau^{-1}$ and 35$Wm^{-2}\tau^{-1}$ under the overlay and mixing condition respectively. The current WRF/CMAQ system assumes internal mixing between different aerosol species to calculate the overall optical properties. So Eτ_Dust is increased by 30% under the mixing condition due to the extra

loading of scattering aerosol from biomass burning. But under the overlaying condition, Eτ_Dust is decreased by 12% since the upper biomass burning aerosol absorbs the reflected solar radiation. Eτ_BB changes from -3.8 $Wm^{-2}\tau^{-1}$ under pure biomass burning condition to -4.2$Wm^{-2}\tau^{-1}$ and -2.6.$Wm^{-2}\tau^{-1}$ under the mixing and overlay condition, respectively. Evaluation of the coexistence cases suggests Eτ_BB is changed by ±8% with the presence of dust aerosol, which is consistent with the 10% estimation reported by Johnson et al [2008]. This study is the first investigation into the coexistence of biomass burning and dust over East Asia. However, there remain lots of uncertainties within the WRF/CMAQ modeling system used in this study, such as the aging process of biomass burning and dust aerosol. So in summary, more research efforts are necessary to further develop the model and evaluate the mixing phase of biomass burning and dust aerosol.

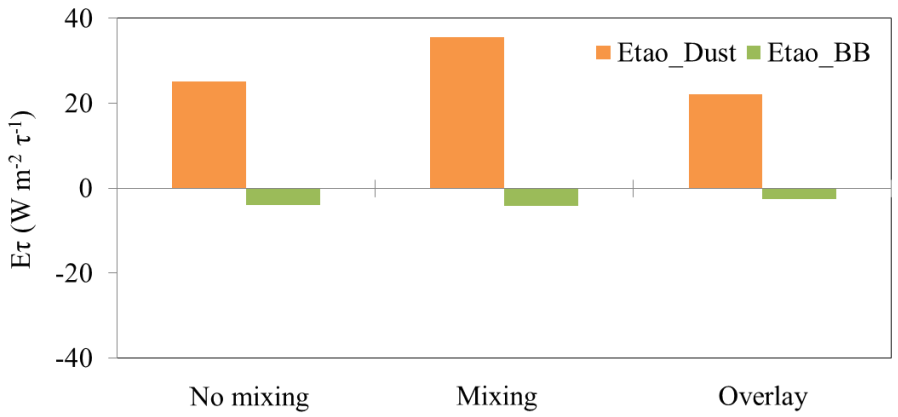

Figure 5.19 Aerosol radiative effect efficiency of dust and biomass burning under "No mixing", "Mixing", and "Overlay" conditions.

6 SUMMARY AND FUTURE STUDIES

6.1 Summary of the study

The impact of biomass burning and natural dust on air quality and regional climate of East Asia is evaluated in this study. Biomass burning emission shows wide annual variation of up to 60% during the study period from 2006 to 2010. The impact of biomass burning on air quality is mostly constrained within the upper air at 1km~6km height due to the uplift motion driven by lee side trough. Contribution of biomass burning to air pollutants gradually declines along the transport pathway from PSEA to the West Pacific due to the dispersion within free troposphere. Uncertainties are identified within the WRF/CMAQ modeling system based on evaluation with measurements from multiple networks. The FLAMBE inventory overestimates NO_x by about 15% due to the overestimated emission factor of deforestation fire. The systematic bias is about ±10% for NO_2 and SO_2 in the INTEX-B inventory, but the uncertainty of the spatial allocation of anthropogenic emission introduces significant simulation bias. Anthropogenic emission inventory of China overestimates NO_2 and SO_2 by 20% and underestimates primary PM_{10} by 30%~50%. This study is the first investigation into the uplift motion scheme and inter-annual variation of biomass burning with modeling method. The uncertainty associated with spatial allocation of the INTEX-B inventory is also investigated for the first time.

The WRF/CMAQ modeling system is improved in this study by incorporating modifications to the wind-blown dust module. Parameterization of the microphysical scheme is revised to remove the double counting of soil moisture effect. Source-dependent speciation profile is developed to specify the mass contributions of aerosol subspecies to dust emission. Dust heterogeneous chemistry is also implemented with a total of 13 reactions. Comparison between the simulations and observations suggests substantial improvement of model performance due to the modifications mentioned above. Simulation bias for PM_{10} is reduced from -55% by the default model to -16% by the revised model. Simulation bias is about -50% for trace metals and total $PM_{2.5}$, indicating the mass contribution of fine mode aerosol is systematically

underestimated by the model. The impact of dust heterogeneous chemistry on deletion of gas-phase species and production of secondary inorganic aerosol is investigated with both lower and upper limits of uptake coefficients. As compared to the default model, simulation with dust chemistry is in better agreement with observation. But no solid conclusion can be achieved with respect to the preference of uptake coefficients, as the lower bound of uptake coefficients favors the simulation of SO_4^{2-} and NO_3^- while the upper bound favors the prediction of SO_2 and NO_2. This study is the first attempt to address the uncertainty within the wind-blown dust scheme of the CMAQ model. The modifications incorporated into the CMAQ system in this study help to improve the model performance and promote it as a useful tool for further investigation of dust storm.

The two-way mode WRF/CMAQ modeling system is applied in this study to evaluate the impact of biomass burning and dust on regional climate. Biomass burning aerosol slightly cools the near surface air by -0.2K but significantly warms the upper air by up to +2K due to the presence of underlying stratocumulus cloud. Dust aerosol shows a stronger cooling effect, as it decreases the near surface air temperature by -0.9K and increases the upper air temperature by only +0.1K. This study is the first investigation into the coexistence of biomass burning and dust over East Asia. The analysis of the WRF/CMAQ simulation and the CALIPSO product reveals that, the warming effect of biomass burning and cooling effect of dust is altered by ±10% when the two types of aerosol encounter with each other.

6.2 Summary of Chapter 3

The impact of biomass burning on near surface air quality shows relatively small inter-annual variation from year to year due to the uplift motion. During the simulation period, the minimum contribution of biomass burning to O_3, $PM_{2.5}$ and CO is 0~25ppbv (0~30%), 2μg/m^3~10μg/m^3 (5%~25%), and 50ppbv~300ppbv (25%~50%) respectively, and the maximum contribution is 5ppbv~40ppbv (5%~45%), 5μg/m^3~20μg/m^3 (10%~45%), 90ppbv~550ppbv (30%~60%) respectively.

Investigation of the geopotential height, lightning activity, and biomass burning carbon emission suggests that the lee side trough along eastern side of the Tibet Plateau is

the dominant driving force for uplifting biomass burning plume, while deep convection plays an unimportant role. This uplift motion leads to substantial loading of air pollutants into the free troposphere of East Asia. The lifted biomass burning plume mostly remains in the upper air, but may be occasionally dragged down to the near surface air of Taiwan with the existence of frontal system. O_3 concentration in lower part of the free troposphere at Taiwan is increased by up to 30% by biomass burning, while the near surface O_3 is altered by less than ±10%.

6.3 Summary of Chapter 4

Modifications are incorporated into the WRF/CMAQ system to enhance the model's capability to simulate the emission, transport, and chemistry of wind-blown dust. The prescribed friction velocity threshold constant is revised based on reanalysis of the field campaign data [*Gillette et al.,* 1980; 1982]. The source-dependent speciation profile is derived from the local measurements to characterize the mass contribution of aerosol subspecies better. Dust heterogeneous chemistry is incorporated into the model to simulate the depletion of gas-phase species and production of secondary inorganic aerosol. These modifications significantly improve the model performance as demonstrated by the comparison between simulations and observations. A severe dust storm around March 19th-21st 2010 is investigated with the revised model. The revised WRF/CMAQ system successfully reproduces the elevated PM_{10} and AOD at selected sites along the transport pathway. Spatial distributions of AOD from the model simulation and the MODIS product are in close agreement with each other. Daily variation of PM_{10} and AOD are also well reproduced by the revised WRF/CMAQ system. But the negative bias at nearby Taklamakan sites and the positive bias at nearby Gobi sites indicates the existence of systematic uncertainty within the modeling system. The Comparison between the FNL and GLDAS reanalysis data suggests that the excessive soil moisture of FNL may be responsible for the underestimation of the Taklamakan dust. The concentration of K^+, Mg_2^+, Ca_2^+, and $PM_{2.5}$ is systematically underestimated by 50%. The mass contribution of total fine mode aerosol to dust emission is setup as 20% by the model, but local sampling data suggests that mass contribution of fine model

aerosol to TSP is 40% at the Taklamakan and Gobi Desert. This study is the first attempt to improve the wind-blown dust scheme of the WRF/CMAQ system. The revised modeling system can serve as a useful tool for further investigating the impact of dust on regional climate.

6.4 Summary of Chapter 5

Simulation from the two-way mode WRF/CMAQ system is evaluated against the CERES and MODIS product. The modeling system successfully reproduces the spatial distribution and vertical profile of meteorological variables. Simulation bias for SWR flux, temperature, relative humidity, and precipitation is 10%, 1%, 7%, and 30% respectively. Impact of biomass burning and dust on regional climate is investigated with the WRF/CMAQ system. Biomass burning aerosol slightly increases the upwelling SWR flux at TOA by +5W/m^2 (2%) under clear sky condition, and significantly reduces the flux by -20W/m^2 (10%) under all sky condition. The significant warming effect of biomass burning aerosol is associated with the presence of the underlying stratocumulus cloud over north Vietnam and south China. Biomass burning aerosol slightly cools the near surface air by -0.2K but significantly warms the upper air by up to +2K. As a result of the changes in radiation flux and temperature profile, regional precipitation of PSEA is also reduced by 10mm/month (2%). But this evaluation may contain substantial uncertainty because the simulated precipitation is contaminated by the nonlinearities in the convective and microphysical parameterizations within the modeling system. Thus the current WRF/CMAQ system has not been well developed to simulate the impact of aerosol on precipitation.

Dust aerosol increases the upwelling SWR at TOA by +15W/m^2 (10%) under clear sky condition and +5W/m^2 (1%) under all sky condition. Impact of dust aerosol on radiative forcing budget receives little intrusion from cloud since transport of dust is usually associated with cold frontal system. But analysis with model simulation and the CALIPSO product reveals that, the direct radiative forcing effect of dust aerosol is gradually contaminated by anthropogenic emission along the transport pathway. The fresh dust primarily cools near surface air by -0.5K over the desert. The partially polluted

dust cools the near surface air by -0.9K and slightly warms the upper air by +0.1K over northern and central China. The full contaminated dust aerosol slightly cools the near surface air by -0.1K and warms the upper air by +0.2K over Japan and the West Pacific.

Two coexistence cases are identified and investigated in this study to evaluate the impact of mixed biomass burning and dust aerosol. Model simulation successfully reproduces the spatial distribution, vertical profile, and temporal variation of biomass burning and dust. On Mar.29th 2006, biomass burning and dust aerosol is detected at 4km and 2km height respectively. On Mar.11th 2010, the two different types of aerosol almost mix with each other at 2km height above the surface ground. The coexistence of biomass burning and dust alters the aerosol radiative effect efficiency by ±10%. The warming effect of biomass burning and cooling effect of dust is reinforced on Mar.29th 2006, yet both of the effects are depressed on Mar.11th 2010. This study is the first investigation into the coexistence of biomass burning and dust over East Asia with the WRF/CMAQ modeling system. However, the current WRF/CMAQ system still contains lots of uncertainty. Some important physical and chemical processes are not well represented by the model, such as the aging process of biomass burning aerosol, and the chemical evolution of dust particles. In summary, more research efforts are necessary to further develop the model and evaluate the impact of aerosol on regional climate of East Asia and elsewhere.

6.5 Future studies

This study provides a baseline estimation of the impact of biomass burning and dust on air quality and regional climate. The investigation conducted in this study helps to improve the understanding of the characteristics of biomass burning and dust. Evaluation of the WRF/CMAQ also helps to address the uncertainties within the modeling system. A total of 100TB data is collected and produced in this study, including the ground-based measurements, satellite observations, and model simulations. This dataset can be used by future studies. The revised WRF/CMAQ system provides a useful tool to investigate the impact of dust in the Earth system.

However, the simulation period is limited by the computational resource to only five years from 2006 to 2010. This analysis period is short as compared to the standard 30-year atmospheric studies. Thus the impact of aerosol on regional climate is evaluated in a relatively loose manner in this study. In addition, the anthropogenic emission is changing so fast that this study is actually a transient climate analysis instead of an equilibrium analysis. So in future study, decadal simulations can be performed to achieve more solid estimation of the regional climate change due to impact of biomass burning and dust aerosol.

The current WRF/CMAQ system assumes internal mixing between different aerosol subspecies, so the future study can also investigate into the external mixing condition. A better representation of the mixing status by the model can provide a more accurate approximation of the aging process of aerosol. Future study can also improve the model by simulating the coating process of organic aerosol on the surface of inorganic aerosol and vice versa. It is reported that coatings of essentially non-absorbing components on strongly absorbing core components can increase the absorption of the composite aerosol [*Schnaiter et al.,* 2003]. Investigation into the evolution of optical properties of the composite aerosol can help to improve the knowledge about the net effect of aerosol on climate change.

Regional climate model studies [*Zhang et al*., 2008, 2009] reported that biomass burning over Amazonia works against the monsoon circulation by stabilizing the lower troposphere and weakening the surface pressure gradient. So the future study can also investigate the impact of biomass burning and dust on the East Asia Monsoon system.

REFERENCES

Akagi, S. K., Yokelson, R. J., Wiedinmyer, C., Alvarado, M. J., Reid, J. S., Karl, T., Crounse, J. D., and Wennberg, P. O.: Emission factors for open and domestic biomass burning for use in atmospheric models, *Atmos. Chem. Phys.*, 11, 4039–4072, 2011.

Alder, R.F., Huffman, G., Chang, A., Ferraro, R., Xie, P.P., Janowiak, J., Rudolf, B., Schneider, U., Curtis, S., Bolvin, D., Gruber, A., Susskind, J., Arkin, P., and Nelkin, E.: The version-2 Global Precipitation Climatology Project (GPCP) monthly precipitation analysis (1979-present), *Journal of Hydrometeorology*, 4, 1147–1167, 2003.

Alvarado, M. J., Logan, J. A., Mao, J., Apel, E., Riemer, D., Blake, D., Cohen, R. C., Min, K. E., Perring, A. E., Browne, E. C., Wooldridge, P. J., Diskin, G. S., Sachse, G. W., Fuelberg, H., Sessions, W. R., Harrigan, D. L., Huey, G., Liao, J., Case-Hanks, A., Jimenez, J. L., Cubison, M. J., Vay, S. A., Weinheimer, A. J., Knapp, D. J., Montzka, D. D., Flocke, F. M., Pollack, I. B., Wennberg, P. O., Kurten, A., Crounse, J., St Clair, J. M., Wisthaler, A., Mikoviny, T., Yantosca, R. M., Carouge, C. C., and Le Sager, P.: Nitrogen oxides and PAN in plumes from boreal fires during ARCTAS-B and their impact on ozone: an integrated analysis of aircraft and satellite observations, *Atmospheric Chemistry and Physics*, 10, 9739-9760, 2010.

Anantharaj, V. G., Nair, U. S., Lawrence, P., Chase, T. N., Christopher, S., and Jones, T.: Com parison of satellite – TOA shortwave clear – fluxes to estimates from GCM simulations constrained by satellite observations of land surface characteristics, *Int. J. Climatol.*, 30, 2088–2104, 2010.

Appel, K. W., Pouliot, G. A., Simon, H., Sarwar, G., Pye, H. O. T., Napelenok, S. L., Akhtar, F., and Roselle, S. J.: Evaluation of dust and trace metal estimates from the Community Multiscale Air Quality (CMAQ) model version 5.0, *Geoscientific Model Development*, 6, 883-899, 2013.

Arimoto, R., Kim, Y. J., Kim, Y. P., Quinn, P. K., Bates, T. S., Anderson, T. L., Gong, S., Uno, I., Chin, M., Huebert, B. J., Clarke, A. D., Shinozuka, Y., Weber, R. J., Anderson, J. R., Guazzotti, S. A., Sullivan, R. C., Sodeman, D. A., Prather, K. A., and Sokolik, I. N.: Characterization of Asian Dust during ACE-Asia, *Global and Planetary Change*, 52, 23-56, 2006.

Bian, H., Tie, X. X., Cao, J. J., Ying, Z. M., Han, S. Q., and Xue, Y.: Analysis of a Severe Dust Storm Event over China: Application of the WRF-Dust Model, *Aerosol and Air Quality Research*, 11, 419-428, 2011.

Blanco, A., De Tomasi, F., Filippo, E., Manno, D., Perrone, M. R., Serra, A., Tafuro, A. M., and Tepore, A.: Characterization of African dust over southern Italy, *Atmospheric Chemistry and Physics*, 3, 2147-2159, 2003.

Byun, D., and Ching, J. K. S.: Science Algorithms of the EPA Models-3 CommunityMultiscale Air Quality (CMAQ) Modeling System., U. S. Environmental Protection Agency, Office of Research and Development, EPA, Washington, DC, 727, 1999.

Byun, D., and Schere, K. L.: Review of the governing equations, computational algorithms, and other components of the models-3 Community Multiscale Air Quality (CMAQ) modeling system, *Applied Mechanics Reviews*, 59, 51-77, 2006.

Castellanos, P., Boersma, K.F., van der Werf, G.R.: Satellite observations indicate substantial spatiotemporal variability in biomass burning NOx emission facotrs for South America, *Atmospheric Chemistry and Physics*, 14, 3929-3943, 2014.

Carmichael, G. R., Tang, Y., Kurata, G., Uno, I., Streets, D., Woo, J. H., Huang, H., Yienger, J., Lefer, B., Shetter, R., Blake, D., Atlas, E., Fried, A., Apel, E., Eisele, F., Cantrell, C., Avery, M., Barrick, J., Sachse, G., Brune, W., Sandholm, S., Kondo, Y., Singh, H., Talbot, R., Bandy, A., Thorton, D., Clarke, A., and Heikes, B.: Regional-scale chemical transport modeling in support of the analysis of observations obtained during the TRACE-P experiment, *Journal of Geophysical Research-Atmospheres*, 108, 2003.

Carmichael, G. R., Sakurai, T., Streets, D., Hozumi, Y., Ueda, H., Park, S. U., Fung, C., Han, Z., Kajino, M., Engardt, M., Bennet, C., Hayami, H., Sartelet, K., Holloway, T., Wang, Z., Kannari, A., Fu, J., Matsuda, K., Thongboonchoo, N., and Amann, M.: MICS-Asia II: The model intercomparison study for Asia Phase II methodology and overview of findings, *Atmospheric Environment*, 42, 3468-3490, 2008.

Chen, S., Zhao, C., Qian, Y., Leung, R., Huang, J., Huang, Z., Bi, J., Zhang, W., Shi, J., Yang, L., Li, D., and Li, J.: Regional modeling of dust mass balance and radiative forcing over East Asia using WRF-Chem, *Aeolian Research*, 15, 15-30, 2014.

Chuang, C. C., and Penner, J. E.: Effects of Anthropogenic Sulfate on Cloud Drop Nucleation and Optical-Properties, *Tellus Series B-Chemical and Physical Meteorology*, 47, 566-577, 1995.

Chuang, M. T., Chou, C. C. K., Sopajaree, K., Lin, N. H., Wang, J. L., Sheu, G. R., Chang, Y. J., and Lee, C. T.: Characterization of aerosol chemical properties from near-source biomass burning in the northern Indochina during 7-SEAS/Dongsha experiment, *Atmospheric Environment*, 78, 72-81, 2013.

Chun, Y. S., Boo, K. O., Kim, J., Park, S. U., and Lee, M.: Synopsis, transport, and physical characteristics of Asian dust in Korea, *Journal of Geophysical Research-Atmospheres*, 106, 18461-18469, 2001.

Cwiertny, D. M., Young, M. A., and Grassian, V. H.: Chemistry and photochemistry of mineral dust aerosol, *Annual Review of Physical Chemistry*, 59, 27-51, 2008.

Davis, J. M., Bhave, P. V., and Foley, K. M.: Parameterization of N2O5 reaction probabilities on the surface of particles containing ammonium, sulfate, and nitrate, *Atmospheric Chemistry and Physics*, 8, 5295-5311, 2008.

De Longueville, F., Hountondji, Y. C., Henry, S., and Ozer, P.: What do we know about effects of desert dust on air quality and human health in West Africa compared to other regions, *Science of the Total Environment*, 409, 1-8, 2010.

Deng, X. J., Tie, X. X., Zhou, X. J., Wo, D., Zhong, L. J., Tan, H. B., Li, F., Huang, X. Y., Bi, X. Y., and Deng, T.: Effects of Southeast Asia biomass burning on aerosols and ozone concentrations over the Pearl River Delta (PRD) region, *Atmospheric Environment*, 42, 8493-8501, 2008.

Dentener, F. J., Carmichael, G. R., Zhang, Y., Lelieveld, J., and Crutzen, P. J.: Role of mineral aerosol as a reactive surface in the global troposphere, *Journal of Geophysical Research-Atmospheres*, 101, 22869-22889, 1996.

Dong, X. Y., Li, J., Fu, J. S., Gao, Y., Huang, K., and Zhuang, G. S.: Inorganic aerosols responses to emission changes in Yangtze River Delta, China, *Science of the Total Environment*, 481, 522-532, 2014.

Dong, X. Y., and Fu, J. S.: Understanding interannual variations of biomass burning from Peninsular Southeast Asia, part I: Model evaluation and analysis of systematic bias, *Atmospheric Environment*, 116, 293-307, 2015a.

Dong, X. Y., and Fu, J. S.: Understanding interannual variations of biomass burning from Peninsular Southeast Asia, part I: Variability and different impacts in lower and higher atmospheric layers, *Atmospheric Environment*, 115, 9-18, 2015b.

EANET: EANET Data Report 2006, Acid Deposition Monitoring Network in East Aisa (EANET), 2007.

Engelstaedter, S., Kohfeld, K. E., Tegen, I., and Harrison, S. P.: Controls of dust emissions by vegetation and topographic depressions: An evaluation using dust storm frequency data, *Geophysical Research Letters*, 30, 2003.

Fairlie, T. D., Jacob, D. J., Dibb, J. E., Alexander, B., Avery, M. A., van Donkelaar, A., and Zhang, L.: Impact of mineral dust on nitrate, sulfate, and ozone in transpacific Asian pollution plumes, *Atmospheric Chemistry and Physics*, 10, 3999-4012, 2010.

F ́ecan, F., Marticorena, B., and Bergametti, G.: Parametrization of the increase of the aeolian erosion threshold wind friction velocity due to soil moisture for arid and semi-arid areas, *Ann. Geophys.*, 17, 149–157, 1999.

Fisher, J. A., Jacob, D. J., Purdy, M. T., Kopacz, M., Le Sager, P., Carouge, C., Holmes, C. D., Yantosca, R. M., Batchelor, R. L., Strong, K., Diskin, G. S., Fuelberg, H. E., Holloway, J. S., Hyer, E. J., McMillan, W. W., Warner, J., Streets, D. G., Zhang, Q., Wang, Y., and Wu, S.: Source attribution and interannual variability of Arctic pollution in spring constrained by aircraft (ARCTAS, ARCPAC) and satellite (AIRS) observations of carbon monoxide, *Atmospheric Chemistry and Physics*, 10, 977-996, 2010.

Formenti, P., Elbert, W., Maenhaut, W., Haywood, J., and Andreae, M. O.: Chemical composition of mineral dust aerosol during the Saharan Dust Experiment (SHADE) airborne campaign in the Cape Verde region, September 2000, *Journal of Geophysical Research-Atmospheres*, 108, 2003.

Forster, P.M.F., and Taylor, K.E.: Climate forcings and climate sensitivities diagnosed from coupled climate model integrations, *J. Clim.*, 19, 6181–6194, 2006.

Fu, J. S., Jang, C. J., Streets, D. G., Li, Z. P., Kwok, R., Park, R., and Han, Z. W.: MICS-Asia II: Modeling gaseous pollutants and evaluating an advanced modeling system over East Asia, *Atmospheric Environment*, 42, 3571-3583, 2008.

Fu, J. S., Dong, X. Y., Gao, Y., Wong, D. C., and Lam, Y. F.: Sensitivity and linearity analysis of ozone in East Asia: The effects of domestic emission and intercontinental transport, *Journal of the Air & Waste Management Association*, 62, 2012a.

Fu, J. S., Hsu, N. C., Gao, Y., Huang, K., Li, C., Lin, N. H., and Tsay, S. C.: Evaluating the influences of biomass burning during 2006 BASE-ASIA: a regional chemical transport modeling, *Atmospheric Chemistry and Physics*, 12, 3837-3855, 2012b.

Fu, X., Wang, S. X., Cheng, Z., Xing, J., Zhao, B., Wang, J. D., and Hao, J. M.: Source, transport and impacts of a heavy dust event in the Yangtze River Delta, China, in 2011, *Atmospheric Chemistry and Physics*, 14, 1239-1254, 2014.

Gillette, D.A., Adams, J., Endo, A., Smith., D., and Kihl, R.: Thereshold velocities for input of soil particles into the air by desert soils, *Journal of Geophysical Research-Atmospheres*, 85, 5621-5630, 1980.

Gillette, D.A., Adams, J., Muhs, D., and Kihl, R.: Thereshold friction velocities and rupture moduli for crusted desert soils for the input of soil particles into the air, *Journal of Geophysical Research-Atmospheres*, 87, 9003-9015, 1982.

Ginoux, P., Chin, M., Tegen, I., Prospero, J. M., Holben, B., Dubovik, O., and Lin, S. J.: Sources and distributions of dust aerosols simulated with the GOCART model, *Journal of Geophysical Research-Atmospheres*, 106, 20255-20273, 2001.

Grell, G. A., Peckham, S. E., Schmitz, R., McKeen, S. A., Frost, G., Skamarock, W. C., and Eder, B.: Fully coupled "online" chemistry within the WRF model, *Atmospheric Environment*, 39, 6957-6975, 2005.

Guenther, A., Karl, T., Harley, P., Wiedinmyer, C., Palmer, P. I., and Geron, C.: Estimates of global terrestrial isoprene emissions using MEGAN (Model of Emissions of Gases and Aerosols from Nature), *Atmospheric Chemistry and Physics*, 6, 3181-3210, 2006.

Gustafsson, O., Krusa, M., Zencak, Z., Sheesley, R. J., Granat, L., Engstrom, E., Praveen, P. S., Rao, P. S. P., Leck, C., and Rodhe, H.: Brown Clouds over South Asia: Biomass or Fossil Fuel Combustion, *Science*, 323, 495-498, 2009.

Han, X., Ge, C., Tao, J. H., Zhang, M. G., and Zhang, R. J.: Air Quality Modeling for a Strong Dust Event in East Asia in March 2010, *Aerosol and Air Quality Research*, 12, 615-628, 2012.

Haustein, K., Perez, C., Baldasano, J. M., Jorba, O., Basart, S., Miller, R. L., Janjic, Z., Black, T., Nickovic, S., Todd, M. C., Washington, R., Muller, D., Tesche, M., Weinzierl, B., Esselborn, M., and Schladitz, A.: Atmospheric dust modeling from meso to global scales with the online NMMB/BSC-Dust model - Part 2: Experimental campaigns in Northern Africa, *Atmospheric Chemistry and Physics*, 12, 2933-2958, 2012.

Haywood, J., Francis, P., Dubovik, O., Glew, M., and Holben, B.: Comparison of aerosol size distributions, radiative properties, and optical depths determined by aircraft observations and Sun photometers during SAFARI 2000, *Journal of Geophysical Research-Atmospheres*, 108, doi:10.1029/2002jd002250.

Haywood, J.M., Osborne, S.R., Abel, S.J.: The effect of overlying absorbing aerosol layers on remote sensing retrievals of cloud effective radius and cloud optical depth, *Q. J. R. Meteorol. Soc.*, 130, 779-800, 2004

Heikes, B. G., and Thompson, A. M.: Effects of Heterogeneous Processes on No3, Hono, and Hno3 Chemistry in the Troposphere, *Journal of Geophysical Research-Oceans and Atmospheres*, 88, 883-895, 1983.

Holben, B.N., Eck, T.F., Slutsker, I., Tanre, D., Buis, J.P., Setzer, A., Vermote, E., Reagan, J.A., Kaufman, Y.J., Nakajima, T., Lavenu, F., Jankowiak, I., Smirnov, A.: AERONET – a federated instrument network and data archive for aerosol characterization. *Remote Sensing of Environment*, 66, 1-16, 1998.

Holben, B.N., Tanre, D., Simrnov, A., Eck, T.F., Slutsker, I., Abuhassan, N., Newcomb, W.W., Schafer, J.S., Chatenet, B., Lavenu, F., Kaufman, Y.J., Castel, J.V, Setzer, A., Markham, B., Clark, D., Frouin, R., Halthore, R., Karneli, A., O'Neill, N.T., Pietras,

C., Pinker, R.T., Voss, K., Zibordi, G.: An emerging ground based aerosol climatology: Aerosol optical depth from AERONET. *Geophys Res Lett*., 106, 12067-12097, 2010

Hsu, N. C., Herman, J. R., and Tsay, S. C.: Radiative impacts from biomass burning in the presence of clouds during boreal spring in southeast Asia, *Geophysical Research Letters*, 30, 2003.

Hsu, N.C., Herman,J.R. and Weaver,. C.: Determination of radiative forcing of Saharan dust using combined TOMS and ERBE data, *J. Geophys. Res.*, 105, 20649–20661, 2000.

Hu, X. M., Nielsen-Gammon, J. W., and Zhang, F. Q.: Evaluation of Three Planetary Boundary Layer Schemes in the WRF Model, *Journal of Applied Meteorology and Climatology*, 49, 1831-1844, 2010.

Huang, K., Zhuang, G. S., Li, J. A., Wang, Q. Z., Sun, Y. L., Lin, Y. F., and Fu, J. S.: Mixing of Asian dust with pollution aerosol and the transformation of aerosol components during the dust storm over China in spring 2007, *Journal of Geophysical Research-Atmospheres*, 115, 2010.

Huang, K., Fu, J. S., Hsu, N. C., Gao, Y., Dong, X. Y., Tsay, S. C., and Lam, Y. F.: Impact assessment of biomass burning on air quality in Southeast and East Asia during BASE-ASIA, *Atmospheric Environment*, 78, 291-302, 2013.

Huang, K., Fu, J. S., Gao, Y., Dong, X. Y., Zhuang, G. S., and Lin, Y. F.: Role of sectoral and multi-pollutant emission control strategies in improving atmospheric visibility in the Yangtze River Delta, China, *Environmental Pollution*, 184, 426-434, 2014.

Huffman, G. J., Adler, R. F., Morrissey, M., Bolvin, D. T., Curtis, S., Joyce, R., McGavock, B., and Susskind, J.: Global Precipitation at One-Degree Daily Resolution from Multi-Satellite Observations, *J. Hydrometeor.*, 2, 36–50, 2001.

Huffman, G. J., Adler, R. F., Bolvin, D. T., Gu, G., Nelkin, E. J., Bowman, K. P., Hong, Y., Stocker, E. F., and Wolff, D. B.: The TRMM Multi-satellite Precipitation Analysis: Quasi-Global, Multi-Year, Combined-Sensor Precipitation Estimates at Fine Scale. *J. Hydrometeor*., 8, 38–55, 2007.

Huneeus, N., Schulz, M., Balkanski, Y., Griesfeller, J., Prospero, J., Kinne, S., Bauer, S., Boucher, O., Chin, M., Dentener, F., Diehl, T., Easter, R., Fillmore, D., Ghan, S., Ginoux, P., Grini, A., Horowitz, L., Koch, D., Krol, M. C., Landing, W., Liu, X., Mahowald, N., Miller, R., Morcrette, J.-J., Myhre, G., Penner, J., Perlwitz, J., Stier, P., Takemura, T., and Zender, C. S.: Global dust model intercomparison in AeroCom phase I, *Atmos. Chem. Phys.*, 11, 7781-7816, 2011.

IPCC: Contribution of Working Group I to the Fourth Assessment Report of the Intergovernmental Panel on Climate Change, New York, 2007.

Ito, A., and Penner, J. E.: Historical emissions of carbonaceous aerosols from biomass and fossil fuel burning for the period 1870-2000, *Global Biogeochem Cy.*, 19, 2005.

Jacob, D. J., Crawford, J. H., Kleb, M. M., Connors, V. S., Bendura, R. J., Raper, J. L., Sachse, G. W., Gille, J. C., Emmons, L., and Heald, C. L.: Transport and Chemical Evolution over the Pacific (TRACE-P) aircraft mission: Design, execution, and first results, *Journal of Geophysical Research-Atmospheres*, 108, 1-19, 2003.

Jacobson, M.Z.: Efffects of biomass burning on climate, accounting for heat and moisture fluxes, black and brown carbon, and cloud absorption effects, *Journal of Geophysical Research-Atmospheres*, 119, 8980-9002, 2014.

Jian, Y., and Fu, T. M.: Injection heights of springtime biomass-burning plumes over peninsular Southeast Asia and their impacts on long-range pollutant transport, *Atmospheric Chemistry and Physics*, 14, 3977-3989, 2014.

Johnson, B.T., Heese, B., McFarlane, S.A., Chazette, P., Jones, A., and Bellouin, N.: Vertical distribution and radiative effects of mineral dust and biomass burning aerosol over West African during DABEX, Y., *Journal of Geophysical Research-Atmospheres*, 113, 01-12, 2008.

Kandler, K., Benker, N., Bundke, U., Cuevas, E., Ebert, M., Knippertz, P., Rodriguez, S., Schutz, L., and Weinbruch, S.: Chemical composition and complex refractive index of Saharan Mineral Dust at Izana, Tenerife (Spain) derived by electron microscopy, *Atmospheric Environment*, 41, 8058-8074, 2007.

Kasischke, E.S. and Penner, J.E.: Improving global estimates of atmospheric emissions from biomass burning, *Journal of Geophysical Research*, 109, 0148-0227, 2004.

Kato, S., Loeb, N.G., Rose, F.G., Doelling, D.R., Rutan, D.A., Caldwell, T.E., Yu, L., and Weller, A.: Surface irradiances concistent with CERES-derived top-of-atmosphere shortwave and longwave irradiances, *J. Climate*, 26, 2719–2740, 2013.

Kaufman, Y.J., and Koren, I.: Smoke and pollution aerosol effect on cloud cover. *Science*, 313, 655-658, 2006.

Keil, A., and Haywood, J.M.: Solar radiative foring by biomass burning aerosol particles during SAFARI 2000: A case study based on measured aerosol and cloud properties, *Journal of Geophysical Research*, 108, 8467-8477, 2003.

Krueger, B. J., Grassian, V. H., Cowin, J. P., and Laskin, A.: Heterogeneous chemistry of individual mineral dust particles from different dust source regions: the importance of particle mineralogy, *Atmospheric Environment*, 38, 6253-6261, 2004.

Koren, I., Martins, J.V., Remer, L.A., Afargan, H.: Smoke invigoration versus inhibition of clouds over the Amazon, *Science*, 321, 946-949, 2008

Kurosaki, Y., and Mikami, M.: Regional difference in the characteristic of dust event in East Asia: Relationship among dust outbreak, surface wind, and land surface condition, *Journal of the Meteorological Society of Japan*, 83A, 1-18, 2005.

Kwok, R. H. F., Fung, J. C. H., Lau, A. K. H., and Fu, J. S.: Numerical study on seasonal variations of gaseous pollutants and particulate matters in Hong Kong and Pearl River Delta Region, *J. Geophys. Res.*, 115, D16308, doi:10.1029/2009JD012809, 2010.

Lamsal, L. N., Martin, R. V., van Donkelaar, A., Celarier, E. A., Bucsela, E. J., Boersma, K. F., Dirksen, R., Luo, C., and Wang, Y.: Indirect validation of tropospheric nitrogen dioxide retrieved from the OMI satellite instrument: Insight into the seasonal variation of nitrogen oxides at northern midlatitudes, *Journal of Geophysical Research-Atmospheres*, 115, 2010.

Li, J., Wang, Z. F., Zhuang, G., Luo, G., Sun, Y., and Wang, Q.: Mixing of Asian mineral dust with anthropogenic pollutants over East Asia: a model case study of a

super-duststorm in March 2010, Atmospheric Chemistry and Physics, 12, 7591-7607, 2012.

Li, W. Y., Shen, Z. B, Lu, S. H., and Li, Y. H: Sensitivity Tests of Factors Influencing Wind Erosion, *Journal of Desert Research*, 27, 984–993, 2007.

Liao, H., Seinfeld, J. H., Adams, P. J., and Mickley, L. J.: Global radiative forcing of coupled tropospheric ozone and aerosols in a unified general circulation model, *Journal of Geophysical Research-Atmospheres*, 109, 2004.

Lin, C. Y., Hsu, H. M., Lee, Y. H., Kuo, C. H., Sheng, Y. F., and Chu, D. A.: A new transport mechanism of biomass burning from Indochina as identified by modeling studies, *Atmospheric Chemistry and Physics*, 9, 7901-7911, 2009.

Lin, N. H., Tsay, S. C., Maring, H. B., Yen, M. C., Sheu, G. R., Wang, S. H., Chi, K. H., Chuang, M. T., Ou-Yang, C. F., Fu, J. S., Reid, J. S., Lee, C. T., Wang, L. C., Wang, J. L., Hsu, C. N., Sayer, A. M., Holben, B. N., Chu, Y. C., Nguyen, X. A., Sopajaree, K., Chen, S. J., Cheng, M. T., Tsuang, B. J., Tsai, C. J., Peng, C. M., Schnell, R. C., Conway, T., Chang, C. T., Lin, K. S., Tsai, Y. I., Lee, W. J., Chang, S. C., Liu, J. J., Chiang, W. L., Huang, S. J., Lin, T. H., and Liu, G. R.: An overview of regional experiments on biomass burning aerosols and related pollutants in Southeast Asia: From BASE-ASIA and the Dongsha Experiment to 7-SEAS, *Atmospheric Environment*, 78, 1-19, 2013.

Lin, N. H., Sayer, A. M., Wang, S. H., Loftus, A. M., Hsiao, T. C., Sheu, G. R., Hsu, N. C., Tsay, S. C., and Chantara, S.: Interactions between biomass-burning aerosols and clouds over Southeast Asia: Current status, challenges, and perspectives, *Environ. Pollut.*, 195, 292-307, 2014.

Liu, H. Y., Jacob, D. J., Bey, I., Yantosca, R. M., Duncan, B. N., and Sachse, G. W.: Transport pathways for Asian pollution outflow over the Pacific: Interannual and seasonal variations, *Journal of Geophysical Research-Atmospheres*, 108, 2003.

Liu, M., and Westphal, D. L.: A study of the sensitivity of simulated mineral dust production to model resolution, *Journal of Geophysical Research-Atmospheres*, 106, 18099-18112, 2001.

Loeb, N. G., Wielicki, B. A., Doelling, D. R., Smith, G. L., Keyes, D. F., Kato, S., Manalo-Smith, N., and Wong, T.: Toward optimal closure of the earth's top-of-atmosphere radiation budget, *J. Climate*, 22, 748–766, doi:10.1175/2008JCLI2637.1, 2009.

Loeb, N. G., Lyman, J. M., Johnson, G. C., Allan, R. P., Doelling, D. R., Wong, T., Soden, B. J., and Stephens, G. L.: Observed changes in top-of-the-atmosphere radiation and upper-ocean heating consistent within uncertainty, *Nat. Geosci.*, 5, 110–113, 2012.

Lu, Z., Zhang, Q., and Streets, D. G.: Sulfur dioxide and primary carbonaceous aerosol emissions in China and India, 1996-2010, *Atmospheric Chemistry and Physics*, 11, 9839-9864, 2011.

Ma, C. J., Kasahara, M., Holler, R., and Kamiya, T.: Characteristics of single particles sampled in Japan during the Asian dust-storm period, *Atmospheric Environment*, 35, 2707-2714, 2001.

Marticorena, B., Bergametti, G., Aumont, B., Callot, Y., NDoume, C., and Legrand, M.: Modeling the atmospheric dust cycle .2. Simulation of Saharan dust sources. *Journal of Geophysical Research-Atmospheres*, 102(D4) 4387-4404, 1997.

Martin, R. V., Jacob, D. J., Yantosca, R. M., Chin, M., and Ginoux, P.: Global and regional decreases in tropospheric oxidants from photochemical effects of aerosols, *J. Geophys. Res.-Atmos.*, 108, 4097, doi:10.1029/2002JD002622, 2003.

Meskhidze, N., Chameides, W. L., Nenes, A., and Chen, G.: Iron mobilization in mineral dust: Can anthropogenic SO2 emissions affect ocean productivity, *Geophysical Research Letters*, 30, 2003.

Miller, R. L., Cakmur, R. V., Perlwitz, J., Geogdzhayev, I. V., Ginoux, P., Koch, D., Kohfeld, K. E., Prigent, C., Ruedy, R., Schmidt, G. A., and Tegen, I.: Mineral dust aerosols in the NASA goddard institute for Space Sciences ModelE atmospheric general circulation model, *Journal of Geophysical Research-Atmospheres*, 111, 2006.

Mochida, M., and Kawamura, K.: Hygroscopic properties of levoglucosan and related organic compounds characteristic to biomass burning aerosol particles, *Journal of Geophysical Research-Atmospheres*, 109, 2004.

Muller, J. F., Stavrakou, T., Wallens, S., De Smedt, I., Van Roozendael, M., Potosnak, M. J., Rinne, J., Munger, B., Goldstein, A., and Guenther, A. B.: Global isoprene emissions estimated using MEGAN, ECMWF analyses and a detailed canopy environment model, *Atmospheric Chemistry and Physics*, 8, 1329-1341, 2008.

Myhre, G., Govaerts, Y., Haywood, J. M., Berntsen, T. K., and Lattanzio, A.: Radiative effect of surface albedo change from biomass burning, *Geophysical Research Letters*, 32, 2005.

Myhre, G., Samset, B. H., Schulz, M., Balkanski, Y., Bauer, S., Berntsen, T. K., Bian, H., Bellouin, N., Chin, M., Diehl, T., Easter, R. C., Feichter, J., Ghan, S. J., Hauglustaine, D., Iversen, T., Kinne, S., Kirkevag, A., Lamarque, J. F., Lin, G., Liu, X., Lund, M. T., Luo, G., Ma, X., van Noije, T., Penner, J. E., Rasch, P. J., Ruiz, A., Seland, O., Skeie, R. B., Stier, P., Takemura, T., Tsigaridis, K., Wang, P., Wang, Z., Xu, L., Yu, H., Yu, F., Yoon, J. H., Zhang, K., Zhang, H., and Zhou, C.: Radiative forcing of the direct aerosol effect from AeroCom Phase II simulations, *Atmospheric Chemistry and Physics*, 13, 1853-1877, 2013.

Nakajima, T., Yoon, S. C., Ramanathan, V., Shi, G. Y., Takemura, T., Higurashi, A., Takamura, T., Aoki, K., Sohn, B. J., Kim, S. W., Tsuruta, H., Sugimoto, N., Shimizu, A., Tanimoto, H., Sawa, Y., Lin, N. H., Lee, C. T., Goto, D., and Schutgens, N.: Overview of the Atmospheric Brown Cloud East Asian Regional Experiment 2005 and a study of the aerosol direct radiative forcing in east Asia, *Journal of Geophysical Research-Atmospheres*, 112, 2007.

Nam, J., Wang, Y., Luo, C., and Chu, D. A.: Trans-Pacific transport of Asian dust and CO: accumulation of biomass burning CO in the subtropics and dipole structure of transport, *Atmospheric Chemistry and Physics*, 10, 3297-3308, 2010.

Ohara, T., Akimoto, H., Kurokawa, J., Horii, N., Yamaji, K, Yan, X., and Hayasaka, T.: An Asian emission inventory of anthropogenic emission sources for the period 1980-2020, *Atmos. Chem. Physics.*, 7, 4419–4444, 2007.

Otte, T. L., Pouliot, G., Pleim, J. E., Young, J. O., Schere, K. L., Wong, D. C., Lee, P. C. S., Tsidulko, M., McQueen, J. T., Davidson, P., Mathur, R., Chuang, H.-Y., DiMego, G., and Seaman, N. L.: Linking the Eta Model with the Community Multiscale Air Quality (CMAQ) modeling system to build a national air quality forecasting system, *Weather Forecast.*, 20, 367–384, 2005.

Otte, T. L. and Pleim, J. E.: The Meteorology-Chemistry Interface Processor (MCIP) for the CMAQ modeling system: updates through MCIPv3.4.1, *Geosci. Model Dev.*, 3, 243–256, doi:10.5194/gmd-3-243-2010, 2010

Owen, P.R.: Saltation of uniform grains in air. *Journal of Fluid Mechanics*, 20(2), 225-242, 1964.

Park, S. U., and In, H. J.: Parameterization of dust emission for the simulation of the yellow sand (Asian dust) event observed in March 2002 in Korea, *Journal of Geophysical Research-Atmospheres*, 108, 2003.

Pathak, R. K., Wang, T., and Wu, W. S.: Nighttime enhancement of PM2.5 nitrate in ammonia-poor atmospheric conditions in Beijing and Shanghai: Plausible contributions of heterogeneous hydrolysis of N2O5 and HNO3 partitioning, *Atmospheric Environment*, 45, 1183-1191, 2011.

Phadnis, M. J. and Carmichael, G. R.: Numerical investigation of the influence of mineral dust on the tropospheric chemistry of East Asia, *J. Atmos. Chem.*, 36, 285–323, 2000.

Pham, T.B.T., Manomaiphiboon, K., Vongmahadlek, C.: Updated emission estimates of ozone precursors from energy consumption by power plants and industrial facilities in the central and eastern regions of Thailand, *Asian Journal on Energy and Environment*, 08, 483-489, 2007.

Piao, S., Ciais, P., Huang, Y., Shen, Z., Peng S., Li, J., Zhou, L., Liu, H., Ma, Y., Ding, Y., Friedlingstein, P., Liu, C., Tan, K., Yu, Y., Zhang T., and Fang, J: The impacts of climate change on water resources and agriculture in China, *Nature*, 467, 43-51, 2010.

Porter, D.F., Cassano, J.J., and Serreze, M.C.: Analysisi of the Arctic atmospheric energy budget in WRF: a comparison with reanalyses and satellite observations, , *Journal of Geophysical Research*, 22108-22128, 2011.

Prospero, J. M.: Long-term measurements of the transport of African mineral dust to the southeastern United States: Implications for regional air quality, *Journal of Geophysical Research-Atmospheres*, 104, 15917-15927, 1999.

Pun, B. K., and Seigneur, C.: Sensitivity of particulate matter nitrate formation to precursor emissions in the California San Joaquin Valley, *Environmental Science & Technology*, 35, 2979-2987, 2001.

Qian, W. H., Quan, L. S., and Shi, S. Y.: Variations of the dust storm in China and its climatic control, *Journal of Climate*, 15, 1216-1229, 2002.

Onishi, K., Kurosaki, Y., Otani, S., Yoshida, A., Sugnimoto, N., Kurozawa, Y.: Atmospheric transport route determines components of Asian dust and heal effects in Japan, *Atmospheric Environment*, 49, 94-102, 2012

Reddy, M. S., Boucher, O., Balkanski, Y., and Schulz, M.: Aerosol optical depths and direct radiative perturbations by species and source type, *Geophysical Research Letters*, 32, 2005.

Reid, E. A., Reid, J. S., Meier, M. M., Dunlap, M. R., Cliff, S. S., Broumas, A., Perry, K., and Maring, H.: Characterization of African dust transported to Puerto Rico by individual particle and size segregated bulk analysis, *Journal of Geophysical Research-Atmospheres*, 108, 2003.

Reid, J. S., Hyer, E. J., Prins, E. M., Westphal, D. L., Zhang, J. L., Wang, J., Christopher, S. A., Curtis, C. A., Schmidt, C. C., Eleuterio, D. P., Richardson, K. A., and Hoffman, J. P.: Global Monitoring and Forecasting of Biomass-Burning Smoke: Description of and Lessons From the Fire Locating and Modeling of Burning Emissions (FLAMBE) Program, *IEEE Journal of Selected Topics in Applied Earth Observations and Remote Sensing*, 2, 144-162, 2009.

Reid, J. S., Hyer, E. J., Johnson, R. S., Holben, B. N., Yokelson, R. J., Zhang, J. L., Campbell, J. R., Christopher, S. A., Di Girolamo, L., Giglio, L., Holz, R. E., Kearney, C., Miettinen, J., Reid, E. A., Turk, F. J., Wang, J., Xian, P., Zhao, G. Y., Balasubramanian, R., Chew, B. N., Janjai, S., Lagrosas, N., Lestari, P., Lin, N. H., Mahmud, M., Nguyen, A. X., Norris, B., Oanh, N. T. K., Oo, M., Salinas, S. V., Welton, E. J., and Liew, S. C.: Observing and understanding the Southeast Asian aerosol system by remote sensing: An initial review and analysis for the Seven Southeast Asian Studies (7SEAS) program, *Atmospheric Research*, 122, 403-468, 2013.

Rodell, M., Houser, P. R., Jambor, U., Gottschalck, J., Mitchell, K., Meng, C. J., Arsenault, K., Cosgrove, B., Radakovich, J., Bosilovich, M., Entin, J. K., Walker, J. P., Lohmann, D., and Toll, D.: The global land data assimilation system, *B Am Meteorol Soc*, 85, 381-401, 2004.

Rosenfeld, D., Rudich, Y., and Lahav, R.: Desert dust suppressing precipitation: A possible desertification feedback loop, *Proceedings of the National Academy of Sciences of the United States of America*, 98, 5975-5980, 2001.

Sarwar, G., Roselle, S. J., Mathur, R., Appel, W., Dennis, R. L., and Vogel, B.: A comparison of CMAQ HONO predictions with observations from the northeast oxidant and particle study, *Atmospheric Environment*, 42, 5760-5770, 2008.

Shao, Y., and Dong, C. H.: A review on East Asian dust storm climate, modelling and monitoring, *Global and Planetary Change*, 52, 1-22, 2006.

Shimizu, A., Sugimoto, N., Matsui, I., Nishizawa, T.: Direct comparison of extinction coefficients derived from Mie-scattering lidar and number concentrations of particles, subjective weather report in Japan, *Journal of Quantitative Spectroscopy and Radiative Transfer*, 153, 77-87, 2014.

Simon, H., Beck, L., Bhave, P.V., Divita, F., Hsu, Y., Luecken, D., Mobley, J.D., Pouliot, G.A., Reff, A., Sarwar, G., and Strum, M.: The development and uses of EPA's SPECIATE database. *Atmospheric Pollution Research*, 1(4) 196-206, 2010.

Skamarock, W. C., and Klemp, J. B.: A time-split nonhydrostatic atmospheric model for weather research and forecasting applications, *J. Comput. Phys.*, 227, 3465-3485, 10.1016/j.jcp.2007.01.037, 2008.

Streets, D. G., Yarber, K. F., Woo, J. H., and Carmichael, G. R.: Biomass burning in Asia: Annual and seasonal estimates and atmospheric emissions, *Global Biogeochemical Cycles*, 17, 2003.

Sun, Y. L., Zhuang, G. S., Wang, Y., Zhao, X. J., Li, J., Wang, Z. F., and An, Z. S.: Chemical composition of dust storms in Beijing and implications for the mixing of mineral aerosol with pollution aerosol on the pathway, *Journal of Geophysical Research-Atmospheres*, 110, 2005.

Sun, Y., Zhang, X., Zwiers, F.W., Song, L., Wang H., Hu, T., Yin, H., and Ren, G.: Rapid increase in the risk of extreme summer heat in Eastern China, *Nature Climate Change*, 4, 1082-1085, 2005.

Tang, Y. H., Carmichael, G. R., Woo, J. H., Thongboonchoo, N., Kurata, G., Uno, I., Streets, D. G., Blake, D. R., Weber, R. J., Talbot, R. W., Kondo, Y., Singh, H. B., and Wang, T.: Influences of biomass burning during the Transport and Chemical Evolution Over the Pacific (TRACE-P) experiment identified by the regional chemical transport model, *Journal of Geophysical Research-Atmospheres*, 108, 2003.

Tang, Y. H., Carmichael, G. R., Kurata, G., Uno, I., Weber, R. J., Song, C. H., Guttikunda, S. K., Woo, J. H., Streets, D. G., Wei, C., Clarke, A. D., Huebert, B., and Anderson, T. L.: Impacts of dust on regional tropospheric chemistry during the ACE-Asia experiment: A model study with observations, *Journal of Geophysical Research-Atmospheres*, 109, 2004.

Tatarov, B., Muller, D., Noh, Y. M., Lee, K. H., Shin, D. H., Shin, S. K., Sugimoto, N., Seifert, P., and Kim, Y. J.: Record heavy mineral dust outbreaks over Korea in 2010: Two cases observed with multiwavelength aerosol/depolarization/Raman-quartz lidar, *Geophysical Research Letters*, 39, 2012.

Thao, P.T.B., Junpen, A., Cheewapongpham, P., Boonman, T., Garivait, S., Chatani, S., Kojima, K.: Bottom-up inventory of air pollutants emissions from power generation in Thailand. 16th GEIA Conference, Colorado, USA, 2014.

Tsai, F. J., Fang, Y. S., and Huang, S. J.: Case Study of Asian Dust Event on March 19-25, 2010 and Its Impact on the Marginal Sea of China, *Journal of Marine Science and Technology-Taiwan*, 21, 353-360, 2013.

Tong, D. Q., Bowker, G. E., He, S., Byun, D. W., Mathur, R., and Gillette, D. A.: Development of a windblown dust emission model FENGSHAA description and initial application in the United States, In review, 2015.

Ummer, K., CARMA Revisited: An Updated Database of Carbon Dioxide Emissions from Power Plants Worldwide, Working Paper Number 304, Center for Global Development, 2012.

Underwood, G. M., Song, C. H., Phadnis, M., Carmichael, G. R., and Grassian, V. H.: Heterogeneous reactions of NO_2 and HNO_3 on oxides and mineral dust: A combined laboratory and modeling study, *J. Geophys. Res.*, 106, 18055–18066, 2001.

Uno, I., Amano, H., Emori, S., Kinoshita, K., Matsui, I., and Sugimoto, N.: Trans-Pacific yellow sand transport observed in April 1998: A numerical simulation, *Journal of Geophysical Research-Atmospheres*, 106, 18331-18344, 2001.

Uno, I., Wang, Z., Chiba, M., Chun, Y.S., Gongs, S.L., Hara, Y., Jung, E., Lee, S.S., Liu, M., Mmikami, Mm., Music, S., Nickovic, S., Satake, S., Shao, Y., Song, Z., Sugimoto, N., Tanaka, T., and Westphal, D.L.: Dust model intercomparision (DMIP) study over Asia: overview, *Journal of Geophysical Research-Atmospheres*, 11, 12213-12233, 2006.

Usher, C. R., Michel, A. E., and Grassian, V. H.: Reactions on mineral dust, *Chemical Reviews*, 103, 4883-4939, 2003.

van der Werf, G.R., Dempewolf, J., Trigg, S.N., Randerson, J.T., Kasibhatla, P.S., Gigliof, L., Murdiyarso, D., Peters, W., Morton, D.C., Collatz, G.J., Dolman, A.J., DeFries, R.S.: Climate regulation of fire emissions and deforestation in equatorial Asia. *Proceedings of the National Academy of Sciences of the United States of America*, 105, 20350-20355, 2008

van der Werf, G.R., Randerson, J.T., Giglio, L., Collatz, G.J., Mu, M., Kasibhatla, P.S., Morton, D.C., DeFries, R.S., Jin, Y., van Leeuwen, T.T.: Global fire emissions and the contribution of deforestation, savanna, forest, agricultural, and peat fires (1997-2009). *Atmospheric Chemistry and Physics*, 10, 11707-11735, 2010

Vogel, B., Vogel, H., Kleffmann, J., and Kurtenbach, R.: Measured and simulated vertical profiles of nitrous acid - Part II. Model simulations and indications for a photolytic source, *Atmospheric Environment*, 37, 2957-2966, 2003.

Wang, K., Zhang, Y., Nenes, A., and Fountoukis, C.: Implementation of dust emission and chemistry into the Community Multiscale Air Quality modeling system and initial application to an Asian dust storm episode, *Atmospheric Chemistry and Physics*, 12, 10209-10237, 2012.

Wang, L., Du, H. H., Chen, J. M., Zhang, M., Huang, X. Y., Tan, H. B., Kong, L. D., and Geng, F. H.: Consecutive transport of anthropogenic air masses and dust storm plume: Two case events at Shanghai, China, *Atmospheric Research*, 127, 22-33, 2013.

Wang, S. H., Lin, N. H., Chou, M. D., and Woo, J. H.: Estimate of radiative forcing of Asian biomass-burning aerosols during the period of TRACE-P, *Journal of Geophysical Research-Atmospheres*, 112, 2007a.

Wang, S. X., Zhao, M., Xing, J., Wu, Y., Zhou, Y., Lei, Y., He, K. B., Fu, L. X., and Hao, J. M.: Quantifying the Air Pollutants Emission Reduction during the 2008 Olympic Games in Beijing, *Environmental Science & Technology*, 44, 2490-2496, 2010.

Wang, S. X., Xing, J., Chatani, S., Hao, J. M., Klimont, Z., Cofala, J., and Amann, M.: Verification of anthropogenic emissions of China by satellite and ground observations, *Atmospheric Environment*, 45, 6347-6358, 2011.

Wang, Y., Zhuang, G. S., Tang, A. H., Zhang, W. J., Sun, Y. L., Wang, Z. F., and An, Z. S.: The evolution of chemical components of aerosols at five monitoring sites of China during dust storms, *Atmospheric Environment*, 41, 1091-1106, 2007b.

Washington, R., Todd, M., Middleton, N. J., and Goudie, A. S.: Dust-storm source areas determined by the total ozone monitoring spectrometer and surface observations, *Annals of the Association of American Geographers*, 93, 297-313, 2003.

Watanabe, M., Kurai, J., Shimizu, E.: Influence of Asian Dust Storm on Asthma in Western Japan, *Genes and Environment*, 36, 137-144, 2014.

Wheeler, D., and Ummer, K.: Calculating CARMA: Global Estimation of CO2 Emission from the Power Sector, Working Paper Number 145, Center for Global Development, 2008.

Wielicki, B.A., Barkstrom, B.R., Baum, B.A., Charlock, T.P., Green, R.N., Kratz, D.P., Lee, R.B., Minnis, P., Smith, G.L., Wong, T., Young, D.F., Cess, R.D., Coakley, J.A., Crommelynck, D.A.H., Donner, L., Kandel, R., King, M.D., Miller, A.J.,

Ramanathan, V., Randall, D.A., Stowe, L.L., and Welch, R.M.: Clouds and the Earth's Radiant Energy System (CRERES): algorithm overview, *IEEE Transations on Geoscience and Remote Sensing*, 36, 1127-1141, 1998.

Wilcox, E.M.: Direct and semi-direct radiative forcing of smoke aerosols over clouds, *Atmos. Chem. Phys.*, 12, 139-149, 2012.

Wong, D., Pleim, J., Mathur, R., Binkowski, F., Otte, T., Gilliam, R., Pouliot, G., Xiu, A., Young, J.O., and Kang, D.: WRF-CMAQ two-way coupled system with aerosol feedback: software development and preliminary results, *Geosci. Model Dev.*, 5, 299-312, 2012.

World Health Organization: Burden of disease attributable to outdoor air pollution, Geneva, 2011

World Health Organization: Burden of disease attributable to outdoor air pollution, Geneva, 2014.

Wu, L., Li, J., Pi, C.J., Yu, J.Y., Chen, J.P.: An observationally based evaluation of WRF seasonal simulations over the Central and Eastern Pacific, *Journal of Geophysical Research-Atmospheres*, 120, 10664-1680, 2015.

Wu, L., Su, Hh., Jiang, J.H., and Read, W.G.: Hydration or dehydration: competing effects of upper tropospheric cloud radiation on the TTL water vapor, *Atmoss. Chem. Phys.*, 12, 7727-7735, 2012..

Xing, J., Mathur, R., Pleim, J., Hogrefe, C., Gan, C.M., Wong, D.C., Wei, C., Gilliam, R, and Pouliot, G.: Observations and modeling of air quality trends over 1990-2010 across the Northern Hemisphere: China, the United States and Europe, *Atmoss. Chem. Phys.*, 15, 2723-2747, 2015.

Xiong, J. Q., Zhong, M. H., Fang, C. P., Chen, L. C., and Lippmann, M.: Influence of organic films on the hygroscopicity of ultrafine sulfuric acid aerosol, *Environmental Science & Technology*, 32, 3536-3541, 1998.

Yang, Y.Q., Wang, J. Z., Niu, Ta., Zhou C.H., Chen, M., Liu, J.Y. The Variability of Spring Sand-Dust Frequency in Northeast Aisa from 1980 to 2011, *Journal of Meteorological Research*, 27, 119-127, 2013.

Yu, S., Mathur, R., Pleim, J., Wong, D., Gilliam, R., Alapaty, K., Zhao, C., and Liu, X.: Aerosol indirect effect on the grid-scale clouds in the two-way coupled WRF–CMAQ: model description, development, evaluation and regional analysis, *Atmos. Chem. Phys.*, 14, 11247–11285, doi:10.5194/acp-14-11247-2014, 2014.

Zhang, Q., Streets, D. G., Carmichael, G. R., He, K. B., Huo, H., Kannari, A., Klimont, Z., Park, I. S., Reddy, S., Fu, J. S., Chen, D., Duan, L., Lei, Y., Wang, L. T., and Yao, Z. L.: Asian emissions in 2006 for the NASA INTEX-B mission, *Atmospheric Chemistry and Physics*, 9, 5131-5153, 2009.

Zhang, X. Y., Gong, S. L., Zhao, T. L., Arimoto, R., Wang, Y. Q., and Zhou, Z. J.: Sources of Asian dust and role of climate change versus desertification in Asian dust emission, *Geophysical Research Letters*, 30, 2003.

Zhao, B., Wang, S. X., Dong, X. Y., Wang, J. D., Duan, L., Fu, X., Hao, J. M., and Fu, J.: Environmental effects of the recent emission changes in China: implications for particulate matter pollution and soil acidification, *Environmental Research Letters*, 8, 2013.

Zhao, C., Liu, X., and Leung, L. R.: Impact of the Desert dust on the summer monsoon system over Southwestern North America, *Atmos. Chem. Phy*s., 12, 3717-3731, 2012.

Zhao, C., Liu, X., Leung, L. R., Johnson, B., McFarlane, S. A., Gustafson, W. I., Fast, J. D., and Easter, R.: The spatial distribution of mineral dust and its shortwave radiative forcing over North Africa: modeling sensitivities to dust emissions and aerosol size treatments, *Atmospheric Chemistry and Physics*, 10, 8821-8838, 2010.

Zhu, H. and Zhang, H. S.: An estimation of the threshold friction velocities over the three different dust storm source areas in northwest China (in Chinese), *Acta. Meteorol. Sin.*, 68, 977–984, 2010.

Zhuang, G. S., Yi, Z., Duce, R. A., and Brown, P. R.: Link between Iron and Sulfur Cycles Suggested by Detection of Fe(Ii) in Remote Marine Aerosols, *Nature*, 355, 537-539, 1992..

VITA

Xinyi Dong was born in Luoyang, Henan Province, China. He received his bachelor and master degrees in Photogrammetry and Remote Sensing from Wuhan University at 2006 and 2008 respectively. He joined the Department of Civil and Environmental Engineering at the University of Tennessee in August 2010. In December 2015, he graduated with a Ph.D. in Civil Engineering and a minor in Computational Science.